IS-T 1874

A Comparison of Thermoelectric Phenomena in Diverse Alloy Systems

by

Cook, Bruce

PHD Thesis submitted to Iowa State University

Ames Laboratory, U.S. DOE

Iowa State University

Ames, Iowa 50011

Date 1999

PREPARED FOR THE U.S. DEPARTMENT OF ENERGY

UNDER CONTRACT NO. W-7405-Eng-82.

DISCLAIMER

This report was prepared as an account of work sponsored by an agency of the United States Government. Neither the United States Government nor any agency thereof, nor any of their employees, makes any warranty, express or implied, or assumes any legal liability or responsibility for the accuracy, completeness or usefulness of any information, apparatus, product, or process disclosed, or represents that its use would not infringe privately owned rights. Reference herein to any specific commercial product, process, or service by trade name, trademark, manufacturer, or otherwise, does not necessarily constitute or imply its endorsement, recommendation, or favoring by the United States Government or any agency thereof. The views and opinions of authors expressed herein do not necessarily state or reflect those of the United States Government or any agency thereof.

This report has been reproduced directly from the best available copy.

AVAILABILITY:

To DOE and DOE contractors: Office of Scientific and Technical Information
P.O. Box 62
Oak Ridge, TN 37831

prices available from: (615) 576-8401
FTS: 626-8401

To the public: National Technical Information Service
U.S. Department of Commerce
5285 Port Royal Road
Springfield, VA 22161

TABLE OF CONTENTS

CHAPTER 1. INTRODUCTION

1.1. Dissertation Organization

This dissertation describes research on the thermoelectric properties of a number of diverse alloy systems and is submitted in an alternate format. Chapter 1 is a general introduction to the theory of thermoelectric materials and power generation. Chapter 2 provides a general overview of mechanical alloying. Chapter 3 is a paper published in the Journal of Applied Physics entitled "Parasitic Effects of Oxygen on the Thermoelectric Properties of $Si_{80}Ge_{20}$ Doped with GaP and P." Chapter 4 is a paper published in the Journal of Applied Physics entitled "$Si_{80}Ge_{20}$ Thermoelectric Alloys Prepared with GaP Additions." Chapter 5 is a paper published in the Journal of Applied Physics entitled "Electrical Properties of Ga and ZnS-doped ZnO Prepared by Mechanical Alloying." Chapter 6 is a selection entitled "High Temperature Thermoelectric Properties of MNiSn (M=Ti,Zr,Hf)," and is based on papers published in the Proceedings of the XVIII International Conference on Thermoelectrics, Baltimore, MD (1999), in the Proceedings of the Fifth European Workshop on Thermoelectric Materials, Pardubice, Czech Republic (1999), and in the Journal of Material Science, 34 (1999) 323. Chapter 7 is a paper to be published in the Journal of Applied Physics entitled "Thermoelectric Properties of Hot Pressed $(Nd_{0.5}Gd_{0.5})Se_{1.50-x}$ Where $x = 0.01, 0.02$." Chapter 8 consists of general conclusions drawn from these papers. References cited in chapter 1 and chapter 8 are listed at the end of the dissertation.

1.2. General Introduction

The study of thermoelectric phenomena in solids provides a wealth of opportunity for exploration of the complex interrelationships between structure, processing, and properties of materials. As "thermoelectricity" implies some type of coupled "thermal" and "electrical" behavior, it is expected that a basic understanding of transport behavior in materials is the goal of such a study. However, transport properties such as electrical resistivity and thermal diffusivity cannot be fully understood and interpreted without first developing an understanding of the material's preparation and its underlying structure. It is the objective of this dissertation to critically examine a number of diverse systems in order to develop a broad perspective on how structure-processing-property relationships differ from system to system, and to discover the common parameters upon which any good thermoelectric material is based. The alloy systems examined in this work include silicon-germanium, zinc oxide, complex intermetallic compounds such as the half-Heusler MNiSn, where M = Ti, Zr, or Hf, and rare earth chalcogenides

The thermoelectric effect is recognized as a fundamental electro-thermal property of matter, which is described by the dimensionless figure of merit, ZT;

$$ZT = \frac{S^2\sigma T}{\lambda} \qquad (1)$$

where S is the Seebeck coefficient (sometimes incorrectly termed thermopower [1]), σ is the electrical conductivity, λ is the total thermal conductivity, and T is the absolute temperature. The expression is derived from a thermodynamic analysis of conservation of energy in a thermoelectric heat engine operating between T_h and T_c. It represents the effect of irreversible heat losses, which reduce the efficiency of such a thermoelectric material from the ideal Carnot value of $(T_h-T_c)/T_h = 1 - T_c/T_h$, in which the Carnot efficiency is maximized for the largest possible temperature difference. Obviously, a requisite for high ZT is a large $S^2\sigma$ product, implying high electrical conductivity, concomitant with a large Seebeck coefficient. However, while the electrical conductivity in metals is high, the Seebeck coefficient is low, resulting in a low $S^2\sigma$ product. Conversely, while the Seebeck coefficient tends to be large in insulators, the electrical conductivity is low, again resulting in a low $S^2\sigma$ product. The remaining materials parameter that affects ZT is the thermal conductivity, λ. While a low thermal conductivity might appear at first glance to yield a high ZT, this is not necessarily the case in all materials. Thermal conductivity represents the proportionality coefficient between heat flux and temperature gradient and is actually a sum of (at least) two components, a lattice component due to phonons and an electronic component due to carriers. Recalling the coupling between electrical conductivity and the electronic component of the thermal conductivity, viz. the Wiedemann-Franz relationship, it is observed that if the bulk of the heat in the material is transported by charge carriers, then a low λ must necessarily result in a low σ as well. However, if the dominant mechanism for heat conduction is phonon propagation, then reducing λ to the minimum is a valid approach for increasing ZT. These concepts and the relationship between these three primary macroscopic parameters (electrical conductivity, σ, Seebeck coefficient, S, and thermal conductivity, λ) are summarized in the idealized diagram of Fig. 1. The abscissa, identifying the carrier concentration, is used only as a general guide and is not intended to represent the optimum carrier concentration of any *specific* material.

A renewed interest in thermoelectric materials has recently developed as new techniques provide a means to examine systems unavailable only a few years ago. Novel new materials, thin films and quantum wells, nanocomposites, and new binary and higher order semiconductors provide a wealth of possibilities for improved performance in thermoelectric cooling or power generation devices. During the initial development of semiconductor thermoelectric materials in the late 1950s, there was general optimism regarding the ultimate efficiency of such devices. Today, the best bulk thermoelectric devices have a conversion efficiency of about 10%, well below the predictions of near 35%, widely stated during the late 1950s and early 1960s, and certainly much less than Carnot efficiency. Given the significance of the discovery of a material with a ZT >> 1, both scientifically and technologically, a continued search for such a material is warranted.

Development of a material with a ZT of 3 could make thermoelectric cooling competitive with conventional gas compression systems. Development of a material with a ZT of 4 to 5 could render mechanical engines obsolete. Achieving the kind of efficiencies defined by a ZT > 3 could be as revolutionary to energy science as the development of the transistor was to the electronics industry. There are strong indications that large ZT values (i.e., 2 to 5) may be found in heterostructures, in which mobility enhancement due to the physical separation between carriers and ionized impurities occurs.

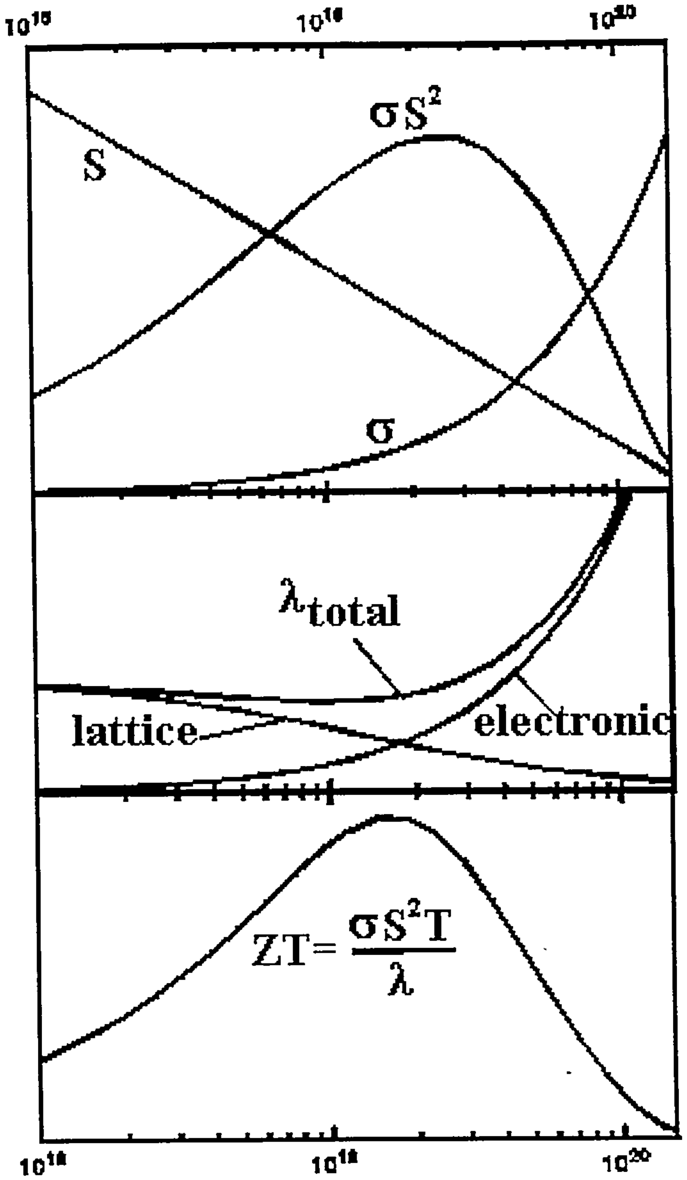

Fig. 1. Idealized Schematic Showing the Relationship Between Electrical Conductivity, Seebeck Coefficient, and Thermal Conductivity on the Dimensionless Quantity ZT

Electrical transport in materials spans over 20 orders of magnitude; ZT itself is a transport property (or a combination of transport coefficients) of materials. Why then, have we not observed ZT = 50 or even 10 in bulk materials since thermodynamics places no upper bound [2] on ZT? Comparisons have been made between the state of thermoelectrics research in the mid- to late-1990s and that of superconductivity in the early 1980s, prior to the discovery of the high T_C oxides. In both cases, little progress in achieving a "significant" breakthrough had been realized for a number of years, and both fields were regarded as somewhat "stagnant." An intriguing question is whether multi-layer "quantum wells" and other heterostructures will ultimately herald a new revolution in thermoelectricity, just as the copper oxides did in the case of superconductivity.

It is the objective of this dissertation to examine several different types of semiconductor materials for common characteristics that give rise to large values of ZT. These materials necessarily fall into the category of either conventional band-type semiconductors or low density of states metals with a gap or pseudo-gap at the Fermi level.

Extending the range of such a comparative study to include "good" metals and ceramics might seem pointless. However, it should be noted that the Seebeck coefficient of $Cu_{0.5}Ni_{0.5}$ is reported to have a magnitude of 73μV/K at 1200K [3], comparable to many conventional semiconductor thermoelectric materials. Even some pure metals have respectably large Seebeck coefficients. For example, at 1273K, the Seebeck coefficient of "pure" Pd has a magnitude of 41 μV/K due to its partially-filled d-bands. The key is the derivative of the density of states with respect to energy, evaluated at the Fermi energy, or

$$S \propto \left. \frac{\partial N(E)}{\partial E} \right\|_{Ef} \qquad (2)$$

In other words, sharp features in the density of states near E_f tend to give large values of the Seebeck coefficient. In the case of Pd, it is thought that an interaction of energy bands at the Fermi surface is responsible not only for the large Seebeck coefficient, but also for the large electrical resistivity and the anomalous value for the Wiedemann-Franz ratio [4]. On the other end of the conductivity spectrum, many low mobility ceramics have been found to also possess reasonable figures of merit. For example, despite a low carrier mobility of 0.1 to 1.0 cm^2/V-s found in the compound B_4C, this material appears to possess a surprisingly large ZT, ranging from 0.3 [5] to nearly 1.0 [6] at 1000°C. The reason for the large Seebeck coefficient and nearly glass-like thermal diffusivity [7] in these so-called "hopping" conductors remains a theoretical challenge. Even high T_c superconducting oxides such as $La_{2-x}M_xCuO_4$ where M = Ba, Sr, Ca have been examined for thermoelectric applications and have been found to have ZT values in excess of 10^{-4}, within an order of magnitude of the best-known semiconductors [8].

1.3 Historical Perspective and Materials Selection Criteria

In the early years of the nineteenth century, there was general disagreement as to the exact cause of the earth's magnetic field. While investigating this phenomenon in 1823, Thomas Seebeck performed an experiment in which two dissimilar conductors were connected and one of the junctions was heated relative to the other. When a compass was placed in the vicinity of this closed circuit, a deflection was observed [9]. At the time, Seebeck erroneously concluded from this experiment that the temperature difference between the earth's poles and the equator was somehow responsible for the earth's magnetic field. While his conclusion was incorrect (although consistent with the results of his observations), he proceeded to catalog various metals available at that time and found that the deflection was related to the electrical resistivity of the material. A similar experiment was performed some 12 years later by Peltier who observed the formation of a temperature difference between the junctions when an electrical current was passed through a circuit [10] . Unfortunately, Peltier failed to make the connection between his work and the earlier discovery of Seebeck. However, in 1838 Lenz repeated Peltier's earlier experiment and correctly concluded that heat is generated or liberated at a junction depending on the direction of current [11]. He demonstrated this principle by freezing water at a bismuth-antimony junction and then melting the ice by reversing the current.

Why should it be that a voltage is generated in a closed loop under the influence of a temperature gradient? To answer this question, one may consider the conduction electrons in the material as an ideal gas. Then, the kinetic energy of the gas particles near the hot end will be greater than that of the particles near the cold end. Thus, there will be a thermally-driven *diffusive* flux of electrons from the hot to the cold region of the material. In the steady state and open circuit limit, charges build up at the cold end until the diffusive flux is balanced by the resulting electrostatic potential difference. The magnitude of the resulting electric field, E, is proportional to the temperature gradient in the material. Writing this as

$$\frac{\Delta V}{\Delta x} = E = S\frac{\Delta T}{\Delta x} \qquad (3)$$

the proportionality constant, S, is a material property called the Seebeck coefficient in units of volts per degree. If such a material were connected to an external load, the charge flow could be made to generate thermodynamic work. In the situation described by this example, the material would be considered an n-type, or electronic conductor and the resulting Seebeck coefficient would be negative. However, there are a few metals that exhibit a positive Seebeck coefficient. This means that the (conventional) current flow and the heat flow are in the same direction (both toward the cold end in this case). The reason for this is based on electron scattering, a phenomenon not described by the free electron gas model. If the scattering rates are strongly temperature dependent, then the mean free path length of electrons at the hot end may be so much less than at the cold end that the electrons actually diffuse *against* the temperature gradient. The noble metals are examples of materials exhibiting a positive Seebeck coefficient whereas most other transition metals exhibit a negative Seebeck coefficient. A positive Seebeck coefficient can also occur in semiconductors where by doping, either electrons or holes can be the dominant charge carrier.

The thermoelectric effect is described by the dimensionless figure of merit, ZT;

$$ZT = \frac{S^2\sigma T}{\lambda} = \frac{S^2\sigma T}{\lambda_e + \lambda_{ph}} = \frac{S^2\sigma T}{L_o\sigma T + \lambda_{ph}} = \frac{S^2}{L_o + \frac{\lambda_{ph}}{\sigma T}} \qquad (4)$$

where S is the Seebeck coefficient, σ is the electrical conductivity, λ is the total thermal conductivity given by the sum of λ_e and λ_{ph}, the electronic and lattice components, respectively, and T is the absolute temperature. This expression is derived from a thermodynamic analysis of conservation of energy in a thermoelectric heat engine operating between T_h and T_c. It represents the irreversible heat losses which reduce the efficiency of such a thermoelectric material from the ideal Carnot value of $(T_h-T_c)/T_h = 1 - T_c/T_h$, and for which Carnot efficiency is maximized for the largest possible temperature difference. The exact relationship between conversion efficiency, η, and the quantity ZT was developed initially by Ioffe and is given in equation 5.

$$\eta = \frac{T_h - T_c}{T_h} \frac{\sqrt{1+ZT_M} - 1}{\sqrt{1+ZT_M} + \frac{T_c}{T_h}} \qquad (5)$$

where the subscript "M" refers to the temperature at which the Z versus T curve reaches a maximum, i.e., at the optimum operating point. Equation (5) shows that the efficiency increases as the quantity $(1+ZT)^{½}$ is increased. As the quantity ZT is allowed to increase to infinity, the efficiency of the heat engine approaches the limiting Carnot value for the given temperature difference. Obviously, materials with a large Seebeck coefficient, a high electrical conductivity, and a low thermal conductivity will yield the highest energy conversion efficiency.

Three broad electrical classifications of materials exist: metals, semiconductors, and insulators (superconductors will be neglected since the Seebeck coefficient in the superconducting state is zero). Metals tend to have a relatively low ZT and are not generally considered attractive candidates for power generation or cooling applications. Why is this so? If we consider a normal metal, that is, one for which the Wiedemann-Franz law applies, the electrical and thermal conductivity are *coupled*, so that increasing one results in a concomitant increase in the other with the result that there is no *net* improvement in efficiency. The Wiedemann-Franz law states that $\lambda_e = L_o\sigma T$ where λ_e is the electronic, or polar component of the thermal conductivity, σ is the electrical conductivity, T is the absolute temperature, and L_o is the Lorentz number. Since the total thermal conductivity can be expressed as a sum of that due to lattice vibrations (phonons) and that due to electrons (electronic) viz. $\lambda = \lambda_l + \lambda_e$ then equation (4) can be written

$$ZT = \frac{S^2 \lambda_e T}{L_o T(\lambda_l + \lambda_e)} \qquad (6)$$

But in a metal, virtually all the heat is transported by electrons so $\lambda_l \approx 0$. In this case equation (6) becomes

$$ZT = S^2/L_o \qquad (7)$$

so that the efficiency, through the parameter ZT, depends only on the magnitude of the Seebeck coefficient. The Mott formula for the Seebeck coefficient of metals predicts that S should be linear in the high temperature limit, and have an absolute magnitude on the order of 1 μV/K. This relatively small Seebeck coefficient is mainly a consequence of the degeneracy in the electronic configuration of metals, and accounts for the low ZT values that have been observed. However, it is known that some metal solid solutions have a surprisingly large Seebeck coefficient; for example, $Cu_{0.5}Ni_{0.5}$ is reported to have an S = 73μV/K at 1200K [12] which may be due, in part, to magnetic scattering effects of the Ni atoms. Indeed, most real systems involve complex interactions that require more sophisticated models than that proposed by Mott. The relationship between ZT and Seebeck coefficient for metals, given by equation 5, implies that phonon behavior may have no significant impact on the transport parameters in metal systems since virtually all thermal conduction is electronic.

There are also unusual low temperature effects such as phonon drag that are not explained by simple transport models. Phonon drag is the coupling of electrons and phonons that can occur in certain strongly interacting systems. Phonons of the appropriate wavelength can effectively "drag" electrons down the temperature gradient and contribute to the transport of energy. This results in an enhancement to both the Seebeck coefficient and to the electrical conductivity but is more pronounced on S because it is a first order effect, whereas the contribution to σ is a second order effect. The magnitude of the phonon drag contribution to the Seebeck coefficient is usually a few microvolts per degree, but recent calculations suggest that the effect could be as large at ~ 50 μV/K and occur at much higher temperatures than previously thought [13]. The Kondo effect is another well-known phenomenon that results in an enhancement to the thermopower of certain dilute solutions containing magnetic impurities. The conduction electrons undergo a spin-flip upon interacting with the localized moment of 3d or 4d impurities [14]. Heavy-fermion materials exhibit a behavior similar to that of concentrated Kondo systems due to the scattering effects of the rare earth moments. In any case, a metal, in which the heat is transported primarily by carriers, having a Seebeck coefficient of at least 122 μV/deg, (at any temperature), would have a conversion efficiency equal to that of the best known material. The identification of such a metal would be considered a significant breakthrough. Numerous intermetallic compounds exists which have metal-like behavior, however, an appreciable fraction of the heat in these systems is carried by phonons. While it may seem qualitatively reasonable that metals should have a low Seebeck coefficient, there exists no proof of this either from thermodynamics or from solid state theory. While purely speculative, it may turn out that the limiting value of S in a material for which the Wiedemann-Franz law rigorously holds is on the order of (k_B/e) where k_B is Boltzman's constant and e is the electronic charge.

If one examines the relationship between carrier concentration and each of the three macroscopic parameters that determine Z, namely Seebeck coefficient, electrical resistivity, and thermal conductivity, one finds a narrow range of values corresponding to the maximum Z. High carrier concentrations such as those normally found in metals yield a favorably high electrical conductivity but a low Seebeck coefficient. Moreover, the thermal conductivity also tends to be high, as described above. In insulators, the Seebeck coefficient can be quite large, on the order of millivolts per degree, and the thermal conductivity can be relatively low. However, the electrical conductivity and hence ZT also tends to be relatively low. In general, the quantity Z tends to maximize within a rather narrow range of carrier concentration values centered near 10^{19} cm^{-3}. The implication of this result is that the best thermoelectric materials should be heavily doped semiconductors.

Semiconductors constitute a broad class of materials, which have rather unique properties that are well suited for thermoelectric applications. Because of their characteristic gap in the density of states at the Fermi energy, semiconductors tend to have a relatively large Seebeck coefficient compared with that of metals. In particular, those semiconductors that have large numbers of relatively flat energy bands tend to have the highest Seebeck coefficient, on the order of hundreds of microvolts per degree. This is because the Seebeck coefficient is related to the effective mass which, in turn, is given by the (inverse) curvature of the energy bands in reciprocal space. The electrical properties of semiconductors can also be tailored by doping to achieve a compromise between electrical and thermal conductivity. Even so, the Seebeck coefficient is approximately proportional to $n^{-2/3}$ in the parabolic band approximation, where n is the carrier concentration, which means that excessive doping of a semiconductor can reduce the Seebeck coefficient by moving the Fermi level closer to the conduction band for n-type materials or to the valence band for p-type materials, and thereby lowering ZT. One can think of the Seebeck coefficient as a measure of the energy transported per charge carrier, which is proportional to the difference in energy between the conduction band edge and the Fermi level. In an intrinsic semiconductor, the Fermi level lies halfway between the conduction band edge and the valence band. As the carrier concentration is increased through doping, the presence of donor states raises the Fermi level closer to the conduction band thereby decreasing the magnitude of this energy difference. In the degenerate limit, the Fermi level actually lies within the conduction band, and the Seebeck coefficient approaches zero. Another consideration is that the presence of minority, or intrinsic carriers decreases the Seebeck coefficient since electron/hole pairs constitute no *net* charge but carry energy. For this reason the band gap should be sufficiently large to avoid the onset of intrinsic conductivity within the anticipated temperature range of the material. Generally, systems for which $E_g \geq 10k_BT$, where E_g is the magnitude of the band gap, satisfy this requirement.

Conventional semiconductor theory predicts that the best thermoelectric materials are those possessing high carrier mobility, low lattice thermal conductivity, and large effective mass. This concept was originally developed by Ioffe [15] based on generalized Fermi-Dirac statistics for the general class of broad band n-type semiconductors with spherical energy surfaces, and was later refined by Chasmar and Stratton [16] who formulated the expression

$$Z(T) = \beta(T) = \frac{(m^*)^{3/2}\mu}{\lambda_{ph}} \tag{8}$$

where m* is the carrier effective mass, μ is the mobility, and λ_{ph} the lattice component of the thermal conductivity. The obvious implication is that materials with large effective masses, high mobility, and low lattice thermal conductivity will tend to have the largest figure-of-merit. A large effective mass implies something about the Fermi level and its relationship with the conduction (or valence) band edge. The inverse relationship between effective mass and curvature of the energy bands (e.g. dispersion relation) suggests that relatively flat band should give rise to large effective mass values. The requirement for high carrier mobility, μ, implies a preference toward covalent as opposed to ionic bonding. Seminal work on establishing a quantitative relationship between mobility and chemical bonding in semiconducting materials was performed by Walker [17] and subsequently by Goodman [18]. Indeed, the common bulk thermoelectric materials such as Si-Ge, Bi_2Te_3, and PbTe all share a high degree of covalency in their chemical bonding. The third parameter, lattice thermal conductivity, is seen to be inversely related to Z. Consequently, a highly disordered material is desirable from the standpoint of thermal conductivity. A number of mechanisms contribute to the lattice thermal resistivity, and all involve increasing the phonon scattering rate. "Intrinsic" factors such as phonon-phonon and electron-phonon scattering are often augmented by "engineered" or "extrinsic" effects such as mass and strain fluctuation, void fillers (rattlers), charge carriers from dopants, mixed-valence cations, grain boundaries, and precipitates. Phonon-phonon scattering gives rise to the familiar T^{-1} dependence of thermal conductivity above the Debye temperature. Phonon-electron scattering primarily affects the long wavelength, lower energy phonons which have wavenumbers closest to that of the electrons. Point defect scattering, sometimes referred to as "mass fluctuation" scattering most often refers to the scattering that occurs when a displacement wave encounters a zero dimensional disruption in the periodicity of the lattice as described by Klemens [19] and Goldsmid [20] . For example, silicon and germanium are isovalent species but have different atomic masses and exhibit complete miscibility. When one is substituted for another in a host lattice, the electron scattering is minimal, while the difference in mass strongly scatters the short wavelength phonons. This phenomenon has been extensively studied. An excellent example of this is provided by the seminal work of Dismukes, et al. [21], who reported an increase in thermal resistivity of a factor of 2 to 5 in zone leveled Si-Ge solid solution alloys containing either B, P, or As dopants at a level of 1.5×10^{20} cm^{-3}, compared with that of the "pure" endpoints. Their remarkable data is reproduced in Fig. 2. Other factors giving rise to point defect scattering include dislocations, impurities, and vacancies. The "β" parameter referred to in equation 8 has an implicit temperature dependence. For simple broad band semiconductors, λ_{ph} varies as T^{-1}, μ is proportional to the carrier relaxation time (to a first approximation), and the dependence of m* requires identification of the specific scattering mechanisms operative.

As mentioned previously, large effective masses are generally associated with flat bands. Complex unit cells and heavy atoms contribute to a low lattice thermal conductivity by frustrating the propagation of phonons and by decreasing the velocity of sound through the lattice.

High carrier mobility is commonly found to accompany covalent bonding, which is favored by a small electronegativity difference between component atoms. However, it is recognized that most alloys and compounds are neither completely covalent, nor completely ionic. The best known bulk materials today are solid solution alloys of silicon with

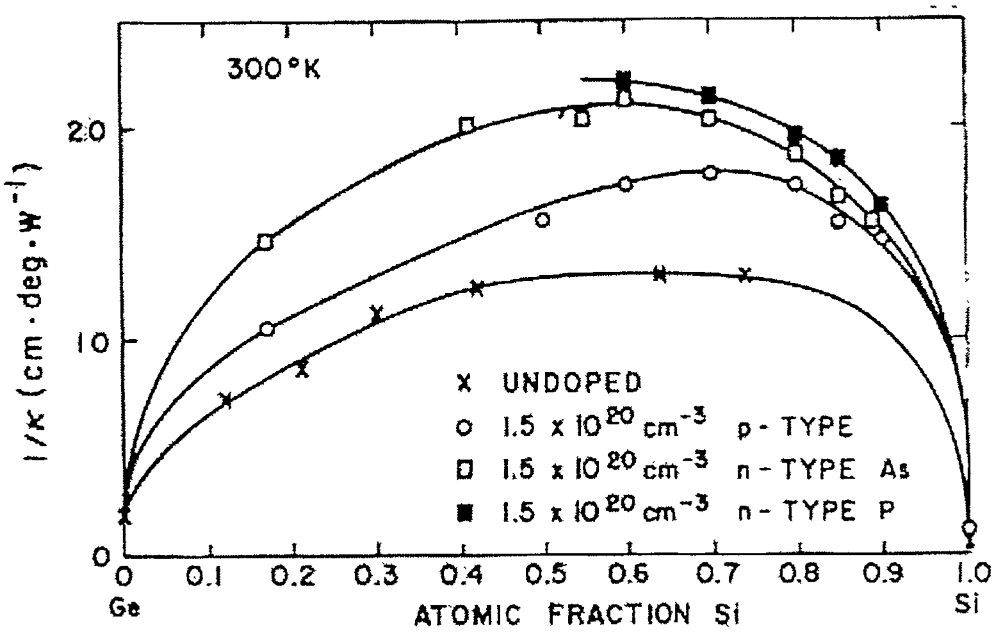

Fig. 2. Thermal resistivity of Si-Ge solid solution alloys
as a function of Si/Ge ratio and dopant
(after Dismukes, et. al., 1964)

germanium, lead with tellurium, and bismuth with antimony. These materials all have a maximum ZT near unity and are characterized by a large fraction of covalent bonding. Other than this, none of these alloy semiconductors have a particularly complex unit cell (Si-Ge is diamond cubic with 8 atoms per unit cell) nor are the band structures remarkable. While numerous binary semiconductors are currently known which have far more complex structures, heavier atoms, and more complex band structures, none has been found to date for which the ZT significantly exceeds unity. Most efforts to improve existing materials involve methods to decrease the phonon thermal conductivity by solid solution alloying and by a dispersion of fine second phase particulates within the grains. Both methods serve to disrupt the periodic order in the lattice and thus decrease the mean free path of phonons.

Over the years, an enormous number of alloys systems has been examined for thermoelectric applications. While some type of property data are known about most of the 4,950 possible binary alloys (crystal structure, density, solubility limits), only about five percent of the possible 161,700 ternary systems have been examined. In other words, little is known about the majority of the possible three-component combinations and even less about the vastly greater number of quaternary and higher order systems. During the last few years, a common thread appears to be emerging among materials research efforts spanning diverse applications: new materials which exhibit extraordinary properties are typically more complex than traditional materials. On one hand, complexity may imply a complex atomic structure. For example, quasicrystalline materials are well-ordered, aperiodic structures that have shown tremendous technological potential in hydrogen storage applications compared with conventional binary crystalline intermetallic compounds. On the other hand, complexity can be associated with a material's composition. Recent developments with rare earth oxide-based phosphors have pointed towards enhanced luminescent efficiency through the incorporation of multiple lanthanide and transition metal cations. In particular, theories describing the transport of conventional band-type thermoelectric semiconductors predict that the lattice thermal conductivity decreases with the number of atoms in the unit cell. Consequently, all other factors being equal, more complex crystal structures should offer the promise of lower lattice thermal conductivity and hence higher efficiency. Ultimately, the quest for high ZT materials is complicated by the fact that increasing the electrical conductivity leads to a deleterious decrease in Seebeck coefficient in band-type conductors. And in systems described by the Wiedemann-Franz law, a decrease in (electronic) thermal conductivity is accompanied by a decrease in the electrical conductivity. Therefore, a careful study of the structure-property relationships in a number of somewhat diverse alloy systems provides an excellent foundation for the transition to more complex, multicomponent materials.

1.4 Rationale for Integration

In virtually any experimental study, a larger sampling size affords better statistics and a more accurate description of the physical phenomenon of interest. Extending this argument to multiple alloy systems, one might expect to develop a more complete understanding of the behavior of any *particular* system through a study of the similarities and differences between diverse alloy systems, within a given framework. For example, while it might be unreasonable to expect new insights into the behavior of conventional band-type conductors by studying thermally-activated polaron hopping systems, there are some mechanisms which share common attributes such as lattice thermal conductivity. The interaction between carrier and the lattice in hopping systems may alter the phonon spectrum compared with that of itinerant conductors, but phenomenologically, the process of heat conduction is the same.

Obviously, the thermoelectric response depends on the type of material. For example in insulators, since the Seebeck coefficient is roughly proportional to the energy difference between the Fermi energy and the conduction or valence band edge (i.e., $S \sim (E_c - E_f)$), materials with the largest Seebeck coefficients are insulators, where the Fermi energy lies deep within the band gap. However, the electrical conductivity is also low, giving rise to a low figure of merit.

In contrast, conduction in metals is a function of the density of states at the Fermi energy; only states near the Fermi energy contribute to current. Ioffe [22] developed a generalized expression for the Seebeck coefficient for monovalent metals:

$$S \approx \pi^2 \frac{k_B}{e} \frac{kT}{\eta} \qquad (9)$$

where η is the magnitude of the Fermi energy and e is the electronic charge. This yields a typical value of 5 μV/K, comparable to that observed in most ordinary ("good") metals.

For semiconductors that can be described by the Boltzman equation for an electron gas, one can derive the following expression for the Seebeck coefficient of a semiconductor in terms of the scattering parameter, r, and the reduced Fermi energy, η^*,

$$S = \frac{k_B}{e}((r+2)+\eta^*) \qquad (10)$$

which is maximized by selection of a semiconductor with the largest reduced Fermi energy, that is, when the Fermi level lies deep within the energy gap. The magnitude of the energy gap is the primary factor governing the Seebeck coefficient of (intrinsic) semiconductors and insulators.

The general category of semiconducting materials can be partitioned into two subcategories, those in which charge carriers move by itinerant motion through relatively broad energy bands, and those for which the charge carriers move by a thermally activated hopping mechanism. In broad band semiconductors, both the electrical conductivity and the Seebeck coefficient are functions of the carrier density. If one can make the assumption that $\lambda_e << \lambda_{ph}$ (i.e., most of the heat is transported by the lattice) then

$$S \sim 2(k_B/e) = 172\ \mu V/K. \qquad (11)$$

For simple band-type conductors describable by Boltzman statistics, it is common to express the electrical conductivity, σ, as a function of carrier concentration, n, and mobility, μ, as

$$\sigma = ne\mu \tag{12}$$

While there is no explicit temperature dependence in this relationship, one immediately recognizes that it must be either the carrier concentration or the mobility that carries a temperature dependence (or both), because σ itself can be a strong function of temperature, particularly in semiconductor materials. The carrier concentration in metals, being strongly degenerate, does not vary significantly with temperature, and it is the mobility, through the scattering rate, which gives rise to the observed increase in resistivity with temperature. On the other hand, the carrier concentration in semiconductors increases exponentially with temperature, given by

$$n = n_o \exp\left\{-\frac{E_g}{2k_BT}\right\} \tag{13}$$

where E_g represents the magnitude of the energy gap. However, band-type semiconductors are not the only materials giving rise to activated conduction behavior.

Narrow-band materials such as many oxides, frequently exhibit hopping conduction. The mean free path is comparable to the lattice spacing, and the carriers are described as localized particles that move in response to a thermally-activated diffusion process. This diffusive motion is referred to as "hopping". If the interaction between the carrier and the lattice is sufficiently strong, the carrier polarizes the lattice and forms a quasiparticle referred to as a polaron. The motion can be treated as a simple diffusion process where the diffusivity, D, is related to the mobility, μ, by the Einstein equation,

$$D = \mu kT \tag{14}$$

Then, one can write the electrical conductivity, σ, as in the case of itinerant conductors as

$$\sigma = ne\mu \qquad (15)$$

so that

$$D = \left(\frac{\sigma}{ne}\right) k_B T \qquad (16)$$

and thus

$$\sigma = \frac{neD}{k_B T} \qquad (17)$$

The diffusion coefficient can be expressed in terms of the atomistic parameters of jump distance, a, probability that a particle will leave its original plane, β, and the probability that a jump will occur, τ^{-1}.

$$D = \beta a^2 \tau^{-1} \qquad (18)$$

One can also write an expression for the jump frequency in terms of the activation energy for a jump, ΔG, by

$$\tau^{-1} = N \tau_o^{-1} \exp\left(\frac{-\Delta G}{k_B T}\right) \qquad (19)$$

where N is the number of sites to which one of these polarons can jump. Therefore, one can write the conductivity in terms of the atomistic parameters as

$$\sigma = \frac{ne}{kT}\left[\beta a^2 N\tau_o^{-1}\exp\left(\frac{-\Delta G}{k_B T}\right)\right] \qquad (20)$$

According to Wood [23], these expressions hold for charge carriers hopping between equivalent sites. In some boron-rich borides, the transport properties are explicable only if the carriers hop, or jump between inequivalent sites.

Consequently, dismissing a particular material as either a band conductor or a polaron hopping conductor based solely on conductivity data could be misleading and lead to an evaluation of its thermoelectric potential based on incorrect interpretation of experimental data. It is precisely these subtleties that make a comparative study intriguing and rich with experimental insights.

1.5 Overview of Material Systems

This dissertation is presented in an alternate format, consisting of five papers that either have been published in referred journals or have been submitted for publication as of the time of this writing. These manuscripts describe fundamental research on the processing and properties of four distinct alloy systems: silicon-germanium, zinc oxide, half-Heusler MNiSn where M = (Ti, Zr, or Hf), and rare earth selenides.

Silicon germanium alloys have formed the backbone of on-board power for a number of planetary probes such as Pioneer I and II, Voyager I and II, Ulysses, Galileo, and Cassini. The remarkable success of these materials is evidenced by the fact that these missions have accumulated over 250,000,000 device-hours without a single failure. Still, the low conversion efficiency of standard (i.e., 1960's vintage) silicon-germanium of 6 to 8 percent motivated studies during the 1980's to improve the performance of this material through the addition of GaP and other additives. A number of studies investigating the effects of microstructural refinement were also performed during this time period. The first two papers describe studies to understand and control the effects of second phase oxygen and the dopants phosphorus and gallium phosphide on the thermoelectric properties of Si-20 at. % Ge alloys. This ratio of silicon to germanium had been previously established as offering the best compromise between low thermal conductivity and high melting point and band gap.

The third paper discusses the electrical and thermal properties of gallium-doped ZnO as a potential thermoelectric material. A combination of reasonable carrier mobility and moderate Seebeck coefficient gave this material an unusually high figure of merit for wide band-gap oxides. Typically, ZT values less than 0.1 are found in oxide systems, however, samples of ZnO:Ga were found to possess a ZT near 0.3, within a factor of three of the best production material, Si-Ge, for high temperature conversion applications. While it appears unlikely that ZnO can be chemically modified, or doped, to offer performance comparable to other more conventional materials, a study of its transport properties provides new insights and possibly applications for wide band gap oxides.

The fourth paper summarizes research into a class of intermetallic compounds known as "half-Heuslers." The structure of these intermetallics is characterized by four interpenetrating fcc sub-lattices, one of which is a vacancy lattice. The resulting configuration gives rise to a gap in the density of states at the Fermi level and semiconducting transport properties. Electronic doping with antimony and bismuth were found to result in remarkable improvements in the electrical properties, while isostructural alloying (i.e., same crystal structure) was shown to lower the thermal conductivity of these compounds.

Finally, the fifth paper provides an overview into the processing and characterization of a series of rare earth selenide compounds based on the formula RSe_x, where R = (Nd, Gd) and $x \cong 1.480$. These alloys were found to offer low, glass-like thermal conductivity which gives rise to a ZT greater than unity. The electrical properties are strongly dependent on composition. Partial substitution of Nd for Gd was shown to stabilize the high temperature cubic (Th_3P_4) phase, desirable for thermoelectric applications.

CHAPTER 2. MECHANICAL ALLOYING

2.1. Overview

Several of the alloy systems discussed in this dissertation were prepared by mechanical alloying (MA), a high energy ball milling technique. Consequently, it is appropriate to provide an overview and general background pertaining to this approach. The technique was originally developed by Benjamin [1] for the preparation of oxide dispersion strengthened (ODS) alloys, and has been extensively applied to various material systems. MA has been used to prepare amorphous metastable alloys, in addition to crystalline phases and ODS alloys. Alloys formed by MA have been commercially produced and in service for many years. For example, INCO's MA 754 nickel based ODS alloy had production rates approaching 100 tons/year in 1994 [2]. Applications include aircraft gas turbine engines and flame stabilizers for oil fired burners in power plants [3].

The type of high energy ball mill has a profound effect on the alloying of the precursor materials. Three basic types of ball mills are available: the shaker mill, the attritor mill, and the planetary mill. In a shaker mill, the precursor materials are loaded into a sealed vial along with a number of balls; the vial is then subject to vigorous shaking action. The nature of this highly energetic milling allows the use of either large chunks or fine powders as the precursor materials. An attritor consists of a sealed tank filled with small grinding balls. The precursor materials are loaded into the tank along with the balls. An impeller is placed in the tank and agitates the balls at high speed. This type of mill requires the precursor materials to be in the form of a fine powder; the mill is unsuitable for breaking up large chunks of material. A planetary mill consists of one or more large vials, into which the precursor materials and grinding balls are loaded. The vials are placed onto a large platform, referred to as the sun wheel, which lies horizontally and rotates at a rapid rate. The vial itself is secured to a second wheel upon the large wheel which rotates in the opposite direction of the sun wheel. The balls and precursor material are forced against the outside wall of the vial by the rotation of the sun wheel. The rotation of the vial causes a rolling motion of the balls and material within the vial which results in the comminution of the material. Although planetary mills can be used to break down larger pieces of material, they are more suitable for grinding and mixing powders. A number of commercial ball mills are available for milling, although most were designed to break down and mix material in short periods of time rather than for forming alloys through extended grinding periods. The first commercial oxide dispersion strengthened materials were mechanically alloyed using an attritor mill [1]. Laboratory scale experiments have often been carried out in shakers mills. One standard mill that is frequently employed is the Spex 8000 mixer/mill from Spex Industries. This type of mill was employed for the work described in Chapters 3, 4, and 5 of this dissertation.

2.2. Mechanical Alloying Theory

Ball milling has long been used as a method of mechanical comminution to achieve small particle sizes. Benjamin [1] first used mechanical alloying in an attritor mill to form oxide dispersion strengthened alloys. Since then mechanical alloying has been applied to many systems to form either crystalline or amorphous alloy powder. The material in a ball mill undergoes repeated fracture and cold welding during milling. Accompanying this process is a temperature rise in the powders that enhances diffusion between particles. Solid solubilities can be enhanced in mechanically alloyed systems. This was demonstrated by Sui [4] with the Al-Co system and Fecht [5] for the Al-Zr system. Sui attributed the enhancement of solubility to elastic strains.

Koch [6] classified mechanical alloying as occurring for three types of systems: ductile/ductile, ductile/brittle, and brittle/brittle. Benjamin [1] is credited for initially examining the formation of oxide dispersion strengthened alloys in ductile/ductile systems. These alloys consisted of a Ni-Al-Ti master alloy crushed to -200 mesh combined with nickel, chromium, thorium oxide, and yttrium oxide powders. Ten kilograms of the powder was combined in a Union Process Model 10-S Szegvari Attritor with 175 kg of +6 cm nickel pellets as the grinding media. The material was ground for 40 hours at 132 rpm under a sealed air atmosphere. Material was removed during processing for optical metallographic analysis. Alloying initially began with the formation of composite metal particles along with unprocessed metal fragments in the powder. The composite particles became more uniform in structure with increased milling time. A striated structure develops in the composite particles as seen by chromium platelets. The amount of unrefined powder also decreases. Further processing eliminates the large chromium platelets from the composite particles. It was thus seen that mechanical alloying in ductile materials occurs through repeated fracture and cold welding. Benjamin and Volin [7] also used a high speed shaker mill with 0.79 cm diameter steel balls to form an alloy of chromium and iron powders. They identified five steps leading to the formation of an alloy. The particles first begin to flatten into plates. Cold welding between particles then begins which results in a lamellar structure within the particles. The lamellar structure becomes finer and more convoluted as milling progresses. Alloying is enhanced due to temperature induced diffusion between the lamella. The fine spacing of the lamella leads to shortened diffusion paths, and the high density of defects also leads to enhanced diffusion. Milling eventually reached a point at which the spacing between lamella could no longer be resolved. Alloying appears to occur similarly in both the attritor and shaker mill.

In the ductile/brittle system, the brittle material fragments and become trapped between the ductile powders as the ductile powders cold weld together. As these particles weld together during continued milling, the size is refined in such as way as to result in a fine dispersion of the brittle material within the ductile material. This is believed to be the method that occurs for ODS alloys.

For brittle/brittle systems the method of alloy formation is not as well understood. Davis and Koch [8] first observed evidence of alloying in the Si-Ge system. X-ray diffraction studies of timed millings indicated that the lattice parameter of Si and Ge gradually changed to the point where a single alloy formed. The observation of material transfer between the components suggested the occurrence of cold welding and diffusion. The cause of transfer may be due to local temperature rises, microdeformation, surface deformation, hydrostatic stresses in the powders during milling, and a frictional wear mechanism. Davis [9] also noted that, for Si-Ge, cooling the vial with liquid nitrogen during milling suppressed alloy formation. They concluded that alloy formation in brittle/brittle systems is thermally activated. Brittle/brittle systems exhibit granular morphologies rather than the lamellar microstructures common for ductile/ductile systems. Alloying is then defined as having occurred when the granular microstructure disappears and is replaced by a homogeneous microstructure. Interparticle necking was also observed in the Si-Ge and Mn-Bi systems.

The mechanical alloying process is difficult to understand and model due to the inability to directly observe the process as it occurs. Davis et al. [9] examined the brittle/brittle Si-Ge and $NiZr_2$-$Ni_{11}Zr_9$ systems in an attempt to understand MA in brittle systems and apply the observations to forming a model of MA in general. They found that there is evidence both for and against large temperature increases in the powder during collisions. The fact that many systems do not undergo recrystallization during MA is taken as evidence by the authors that the temperature increases are no larger than the recrystallization temperature for the system being milled. For example, MA in ductile systems exhibit deformation bands and MA in amorphous systems do not undergo recrystallization. However, Davis et al. do not consider the time aspect of recrystallization. Recrystallization requires both time and temperature since it is a nucleation and diffusion process. During the short periods of ball impact, the temperature could rise above the recrystallization temperature and rapidly be quenched by the surrounding powder before nucleation and recrystallization occur. Davis et al. studied MA with Fe-C martensite powder, and used the decomposition of martensite to cementite as indicated by DTA of the powders to trace temperature increases with ball milling. A series of curves relating the temperature to the percent cementite converted were generated from literature data. Two MA runs were performed using natural and forced air convection while a third used liquid N_2 cooling of the vial. The natural and forced air convection runs gave similar results, suggestive of thermally activated decomposition in the martensite powders. In a plot of powder temperature versus MA time, the natural and forced air convection runs had a positive slope while the liquid N_2 run had zero slope. All three runs have an intercept ranging from 538 to 540 K for the powder temperature. They interpreted the liquid N_2 run as evidence of nonthermal processes enhancing the decomposition of martensite. It was concluded that an upper limit to the temperature increase in the powders was 538 to 550 K. The natural and forced air convection runs demonstrated an increase in temperature with time. The liquid N_2 run maintained a constant temperature throughout the run. Their results with Si-Ge led to the conclusion that MA for brittle systems is thermally activated with temperature increases in the powder in the 200 to 300K range. Computer modeling of the Spex 8000 mill indicated that the number of impacts between balls with enough kinetic energy to increase the total particle temperature are rare. These results led Davis et al. to speculate on the mechanisms that lead to alloying in brittle systems. These mechanisms are surface melting, temperature enhanced microdiffusion, temperature enhanced deformation, microdeformation, and material transfer by frictional wear. They concluded that the temperature increases based on their experimental work as well as the findings of the computer model indicate that localized melting during ball impacts is unlikely.

Maurice and Courtney [10] also developed a model for mechanical alloying in the Spex and attritor mill for ductile metals. The cold welding of particles is assumed to proceed by two methods: direct seizure with no sliding of the particles and indirect seizure caused by the particles sliding across each other during a collision event. Direct seizure occurs from normal impacts. In their model collision events between milling tools were modeled on Hertzian impact theory which assumes no energy loss in a collision, i.e. perfectly elastic. Maurice and Courtney believe that Hertz's theory applies to the types of collisions present during mechanical alloying. They assume that most collisions are nearly perfectly elastic which allows the use of Hertzian impact theory as an approximation. They assume gradual compression of the balls during an impact, which means that any kinetic energy loss in the collision becomes stored elastic energy in the ball which is released as the bodies recover. The presence of powder between the milling tools, whether ball/ball or ball/vial wall collisions, is believed to only slightly perturb the Hertz model of collisions developed. Since the powder particles are considerably smaller than the balls, they view the collision process events as upset forging of the powder between two parallel plates. Maurice and Courtney calculated that the energy consumed in particle deformation is less than the elastic energy of the Hertz impact of the balls. Only a small portion of the available energy is utilized in the plastic deformation of the powder particles. In an attritor, this is a few fractions of a percent whereas for the more energetic Spex mill it can range to several percent. Further calculations showed that the temperature increase between the surface and the bulk of a powder particle following a collision is on the order of 1 K. They concluded that the majority of the collisions experienced during milling would not generate sufficiently high temperatures to produce chemical alloying over large distances. The balls in a Spex mill are estimated to have an impact velocity, and therefore a momentum, approximately an order of magnitude higher than for the attritor mill. Presumably, this is why the Spex mill alloys materials much faster than the attritor.

2.3. Amorphization

One of the more exciting applications of MA has involved the amorphization of metals. Schwarz, Petrich, and Saw [11] examined the amorphization reaction in the Ni-Ti system. Solid state amorphization reactions require both a large negative heat of mixing in the amorphous phase and a fast diffusing element in the system. These two conditions imply that a thermodynamic driving force must exist for the amorphization reaction, and that the reaction must occur at a reasonable rate. The authors examined two possible processes that may lead to amorphization during ball milling. The first is that amorphization takes place during MA through the formation of melt pools in the powder particles trapped between colliding balls. The amorphous phase results from the rapid solidification of these melt pools. Continued fracture and bonding of the powder particles would lead to the formation of larger volumes of amorphous powder until the amorphization reaction is complete. The second is that amorphization occurs via solid state reactions similar to the reactions that occur in the amorphization of multilayered thin films. One difference in the conditions leading to the formation of amorphous phases is that in ball milling the interdiffusion of the elements is enhanced by the accumulation of point defects and high dislocation densities from plastic deformation. Their experiments on Ni-Ti used a Spex 8000 mill with a steel vial and sixty 0.25 inch diameter steel balls. They estimated a ball velocity of 1 m/s was attained. Without cooling, the frictional forces of milling raised the vial temperature 30 K above ambient temperature. The vial was cooled to about 240K in order to enhance the fracture of the metal powders and to avoid the formation of coatings on the milling tools. Milling led to the formation of a layered structure which was refined through the fracture and cold welding process. As the material alloyed it also work hardened which increased the fracture rate. X-ray diffraction patterns of the milled material showed that the sharp crystalline peaks lose their intensity and begin to broaden as milling proceeds. The resulting broad maxima are interpreted as the formation of the amorphous phase. When the powder milled for 5 hours was heat treated for 5 hours at 578K, the amorphous reaction proceeded. The amorphous phase did not form over the entire composition range for Ni_xTi_{1-x}, an amorphous phase resulted for $x = 0.32$ to 0.75. At $x = 0.75$ a mixture of amorphous phase and small crystallites of Ni_3Ti were present. At $x = 0.8$ the amorphous phase and Ni-rich terminal solution were present. This represented an enhanced solubility of Ni in the MA powder. In comparing rapid solidification and MA for forming amorphous alloys in the Ni_xTi_{1-x} system, they found that the composition range of amorphous alloys is larger for MA. This leads to the conclusion that the amorphization reaction does not involve rapid solidification in MA. They conclude that the pressures experienced during ball collisions are two to three orders of magnitude lower than those needed to form surface melting in shock wave consolidated powders. The amorphization reaction occurs through a process similar to the reaction in multilayered thin films. The MA powder consists of swirled layers with high dislocation and defect densities which is raised in temperature during collisions of the milling tools. These conditions are favorable to interdiffusion leading to the amorphization reaction as in thin films. In the MA process grain boundaries and dislocations act as short circuit paths for interdiffusion. The nucleated amorphous phase will not inhibit the interdiffusion of Ni and Ti in MA as it does with thin films; the repeated fracture of the particles also fractures and disperses the amorphous phase which allows fresh surfaces to react.

Johnson [12] believes that the formation of amorphous alloys from elemental powders occurs by the formation of high dislocation densities during MA. The high dislocation densities enhance the mobility of the atoms in the interface of two metals. Ball impacts will cause the temperature to increase which enhances diffusion and allows the solid state amorphization reaction to progress. Johnson believes that amorphization by MA and by interdiffusion in isothermal diffusion couples occur by this method. He does not believe that the crystal solid solution is destabilized by dislocation densities and interfacial densities in microdomain structures produced by MA. This is because the stored energy of severe cold working is a small fraction of ΔH_f. In intermetallic compounds, however, the production of defects leads to the formation of antiphase boundaries or atomic site defects. These induce chemical disorder which can lead to stored energies comparable to ΔH_f.

Hellstern and Shultz [13] have formed amorphous $Cu_{60}Zr_{40}$, $Co_{55}Zr_{45}$, and $Fe_{40}Zr_{60}$ through ball milling in a planetary ball mill. They predict that transition metal-transition metal alloys that can be amorphized by melt spinning, evaporation, or sputtering can also be prepared by MA. Fecht et al. [5] formed amorphous alloys in the Zr-Al system by ball milling with a high energy Spex mill. They found that three metastable phases formed during MA rather than the thermodynamically stable intermetallic compounds that normally form. They believe the amorphization reaction occurs when the α-Zr phase lowers its free energy by incorporating Al atoms up to a concentration at which a metastable equilibrium is reached with the amorphous phase. As the amount of Al introduced into the α-Zr lattice increases, the free energy of the crystalline phase increases to the point where the amorphous phase has a lower free energy. Since low processing temperatures are used in MA, the concentration of Al at which this occurs is increased which leads to enhanced solid solubility before the amorphous phase and the crystalline phase attain equal free energies. The crystalline phase then transforms to a glass. An increase in the heat capacity C_p above the normal ambient value was observed, which was related to the degree of chemical and topological disorder in the crystal of the ball milled powder compared to that of an ideal Zr-Al solid solution. Mechanical alloying refines the grain size and incorporates high angle grain boundaries and defects into the lattice. This leads to an increase in C_p of 5%. This increase has a direct bearing on the processing characteristics, since heat capacity affects a material's ability to dissipate thermal energy. The crystal to glass transition is caused by the layered structure that develops between the Al and Zr during MA. A concentration profile of Al in Zr develops with a higher Al concentration at the Al-Zr interface. The transformation becomes localized at the interfaces during the early alloying stages, and the glass phase grows as milling progresses. The formation of a metallic glass requires chemical disorder in the Zr crystal. Energy is stored in the lattice through the formation of defects via MA. This energy is a significant portion of the enthalpy of fusion of the compound phases. Since MA is a low temperature process, the rate of recovery is low. Fecht states that alloying with 15% Al reduces the melting point of α-Zr from 1820 K to approximately room temperature.

2.4. Mechanical Alloying of Si-Ge Alloys

Davis and Koch [8] initially observed evidence of alloying in the Si-Ge system by MA. Milling was performed on elemental Si and Ge powders using a Spex 8000 mixer/mill, a tool steel vial, and 440C stainless steel balls of 7.9 mm diameter, and a ball to powder mass ratio of 5:1. Milling was carried out under both air and Ar environments. X-ray diffraction indicated that SiO_2 and GeO_2 formed quickly when milling was performed in air. A partial vacuum also formed in the vial following 8 hours of milling, suggestive of oxidation of the powders. Neither oxide lines nor partial vacuum within the vial were detected when milling was performed under Ar. Deviations from initial stoichiometry were observed as determined by lattice parameter measurement using x-ray diffraction. The authors assumed this was due to reaction of the Si powder with the milling media. SEM analysis indicated that the particles were made up of smaller particles cold welded together. Davis, McDemott, and Koch [9] found that alloying of Si-Ge was retarded by chilling the vial, which indicated that the formation of Si-Ge alloys required elevated temperatures.

MA of the Si, Ge and Si-Ge systems utilizing a planetary ball mill has also been examined. Gaffet and Harmelin [14] examined the crystal to amorphous phase transformation in pure Si. They used a Fritsch Pulverisette P7/2 and P5/2 planetary mill to ball mill pure Si in a tempered steel vial with 5-14 gm steel balls under purified Ar. It was found through both x-ray diffraction and selected area diffraction (SAD) in transmission electron microscopy (TEM) analysis that both a crystalline phase and an amorphous phase were present in the milled powders. Similar results were obtained by Gaffet [15] for the ball milling of Ge with the planetary mill. In both cases it is believed that refinement of the particle grain size leads to a destabilization of the diamond cubic lattice which then transforms to the amorphous phase. Gaffet, Faudot, and Harmelin [16] also studied MA in the Si-Ge system using a planetary mill. Planetary ball milling led to the formation of an alloy as with the Spex mill. X-ray diffraction deconvolution found three crystalline grain sizes along with an amorphous phase. They also observed a loss of Si with ball milling. This was attributed to reaction of the Si with the milling tools. The crystalline peaks found were of a diamond cubic solid solution alloy; those corresponding to elemental Si or Ge were absent. They also found that the amorphous phase and the crystalline phase had the same composition. Pixius et al. [17] also examined the mechanical alloying of Si-Ge in a planetary mill. They found that long milling times introduced lead to high wear on the grinding media.

Doping of MA $Si_{80}Ge_{20}$ alloys had not been attempted prior to the work described in the first two papers of this dissertation. The method for making standard Si-Ge alloys for thermoelectric applications traditionally involved melting of the Si-Ge alloy. Phosphorus is then added to the high temperature melt followed by rapid solidification to avoid segregation of the Si and Ge during crystallization of the melt. There are still compositional differences present in the alloy despite the rapid cooling. Homogenization of the alloy involves crushing and grinding the ingot followed by hot pressing. This step is repeated to further homogenize the alloy. MA offers the advantage that the formation of a usable alloy is a two step process: MA followed by hot pressing. The addition of volatile dopants such as P to the melt are avoided, making the control of stoichiometry of the alloy easier.

2.5. References

1. J. S. Benjamin, Met. Trans. **1**, 2943 (1970).
2. J. M. Poole and J. J. Fisher, Mat Tech 9(1/2):21-25 (1994).
3. J. J. Fischer and J. H. Weber, Advanced Materials and Processes, 10/90, 43.
4. H. X. Sui, M. Zhu, M. Qi, B. Li, and D. Z. Yang, J. Appl. Phys **71** (6) 2945 (1992).
5. H.J. Fecht, G. Han, Z. Fu, and W. L. Johnson, J. Appl. Phys. **67** (4), 1744 (1990).
6. C. C. Koch, Ann. Rev. Mater. Sci. **19**, 121 (1989).
7. J. S. Benjamin and T. E. Volin, Met. Trans. **5**, 1929 (1974).

8. R. M. Davis and C. C. Koch, Scripta Met. **21**, 305 (1987).
9. R. M. Davis, B. McDermott, and C. C. Koch, Met. Trans. A, **19A**, 2867 (1988)
10. D. R. Maurice and T. H. Courtney, Met. Trans. A, **21A,** 289 (1990).
11. R. B. Schwarz, R. R. Petrich, and C. K. Saw J. Non-Cryst. Solids, **76**, 281 (1985).
12. W. L. Johnson, Prog. Mat. Sci., **30**, 81, (1986).
13. E. Hellstern and L. Shultz, Appl. Phys. Lett., **48** (2), 124 (1986).
14. E. Gaffet and M. Harmelin, J. Less Common Metals, **157**, 201 (1990).
15. E. Gaffet, Mat. Sci. Eng. **A136**, 161 (1991).
16. E. Gaffet, F. Faudot, and M. Harmelin, Mat. Sci. Eng., **A149**, 85 (1991).
17. K. Pixius, W. Wunderlich, J. Schilz, and W. Amend, Phys. Stat. Sol. (a) **146**, 109 (1994).

CHAPTER 3. PARASITIC EFFECTS OF OXYGEN ON THE THERMOELECTRIC PROPERTIES OF $Si_{80}Ge_{20}$ DOPED WITH GaP AND P

A paper published in the Journal of Applied Physics, **72** (1992) 1423 - 1428

B. A. Cook, J. L. Harringa, S. H. Han, and B. J. Beaudry

3.1. Abstract

The presence of oxygen in silicon-germanium can have a significant effect on the sintering, microstructural, and transport properties of these alloys. A neutron activation study was performed to follow the total oxygen content during the preparation of mechanically alloyed n-type Si-20 at. % Ge alloys using either fine powders, polycrystalline Czochralski chunk, or single-crystal float zoned starting materials. The alloys were prepared with a nominal composition of $Si_{0.747}Ge_{0.187}(GaP)_{0.016}P_{0.034}$. The total oxygen concentration was measured in the starting materials, after 6 h of mechanical alloying in a helium environment, after hot pressing, and after a 3 h, 1100 °C heat treatment in fused silica ampoules. Alloys that contained oxygen levels in excess of 2.0 at. % exhibited low carrier mobility and low thermal conductivity, whereas those that contained less than 0.6 at. % oxygen possessed high mobility and thermal conductivity. The microstructure, as observed by optical metallography and scanning electron microscopy, was found to differ greatly with oxygen content as the low oxygen alloys showed relatively large, well-defined grains, and the high oxygen alloys showed evidence of poor sintering and limited grain growth.

3.2. Introduction

For more than 15 years space power generation has relied on the conversion of thermal to electrical energy provided by silicon-germanium alloys in radioisotope thermoelectric generators (RTGs) (1). Despite recent promising work on the characteristics of advanced materials (2), the rigors of long-term testing, bonding, and vaporization studies make it likely that Si-Ge alloys will remain the material of choice in RTGs for the foreseeable future.

In order to improve the performance of these materials, it is important to understand the role of impurities that are an inevitable consequence of handling and processing the raw materials. Central to this is the role of oxygen, since it is ubiquitous and highly reactive. While there is an exhaustive amount of information available on the role of oxygen in silicon up to the solubility limit, little has been published on the effects of oxygen in silicon-germanium alloys especially with regard to the transport properties. It was first pointed out by McVay et al. in 1974 (3) that the processing of silicon-germanium alloys using an agate mortar and pestle introduces SiO_2 contaminants into the alloy. Savvides and Goldsmid (4) also refer to SiO_2 contamination in the hot pressed Si-Ge they studied, but no mention was made of the effect on transport properties. Bhandari and Rowe (5) mention that oxygen may be responsible for some degradation of electrical properties observed in hot pressed Si-Ge relative to zone-leveled alloys. More recent studies by Vining et al. (6) on hot pressed, sintered $Si_{80}Ge_{20}$ prepared by a variety of comminution techniques showed that total oxygen contents can range from 0.3 to 6.7 at. %, as measured by neutron activation. A further recent TEM characterization of Si-Ge alloys used in the MOD-RTG program performed by Owusu-Sekyere, Jesser, and Rosi (7) showed that these alloys contained 30 to 400 nm SiO_x crystallites at a density of 800 cm^{-2}, with x presumably near 2.

The question of the effect of oxygen in Si-Ge(GaP) alloys bifurcates. First, the physical nature of the oxygen defect itself must be identified. The heats of formation of SiO_2 and of Ga_2O_3 are both quite large and negative (-878.6 kJ/mole and -1075.3 kJ/mol, respectively) indicating that the formation of these compounds is thermodynamically favored. Stūdies by Gosele and Tan (8) show that oxygen precipitates in silicon consist of either amorphous or crystalline SiO_x with $x \cong 2$. Since oxygen solubility in silicon is approximately 10^{18} cm^{-3} (0.002 at. %) near the liquidus (9), virtually all excess oxygen is expected to exist as a second phase compound. Doremus(10) showed that in an oxidized silicon-germanium mixture the silicon is oxidized, but not the germanium. The presence of these second phase oxides is likely to manifest itself in a slight shift of the lattice parameter as silicon is oxidized and the bulk composition of the alloy is shifted toward a more germanium-rich value. Second, the effect of these second phase impurities on the transport properties must be identified. The presence of neutral second phase impurities can lower carrier mobility through impurity scattering and by increasing the number of grain boundary potential barriers if a sufficiently fine-grained microstructure is produced. Alloys having significantly different oxygen contents would likely exhibit microstructural variations that would in turn provide information about the nature of the sintering process. Normal solid-phase sintering is a diffusion-controlled process and proceeds through the reduction of surface energy. Oxides can reduce diffusional transport during sintering so that a heavily oxygenated specimen may show limited grain growth during hot pressing, especially if the oxide is well dispersed. The thermal conductivity would also be expected to decrease with an increase in the concentration of neutral second phase impurities. In semiconductors doped to a level of 10^{20} cm^{-3} or higher, a decrease in the electronic component of the thermal conductivity would account for most of the observed reduction in total thermal conductivity in large grained alloys. The lattice thermal conductivity would be affected to a lesser degree from phonon-impurity scattering provided the impurity density is sufficiently high to at least affect the mean free path of acoustical phonons in the solid at a given temperature. Grain boundary scattering, determined by the microstructure, is not a significant contribution to the lattice thermal conductivity at the typical operating temperatures of thermoelectric power generation materials.

The objective of this study was to determine the maximum tolerable oxygen level in current n-type Si-Ge thermoelectric materials as a compromise between high figures of merit (a fundamental material parameter) and reasonable preparation and processing conditions. A starting point is to evaluate the variation in fundamental thermoelectric properties with the amount and distribution of oxygen in commonly obtained starting materials.

3.3. Experiment

$Si_{0.747}Ge_{0.187}(GaP)_{0.016}P_{0.034}$ alloys were prepared by the mechanical alloying (MA) of the elemental constituents and GaP. The details of this high energy ball milling technique as applied to the preparation of thermoelectric materials have been reported previously (11,12) and therefore will not be discussed here. The interested reader is also referred to one of the many review articles on MA in the literature for details of the process itself (13-17). The composition was developed at the General Electric Astro-Space Division (King of Prussia, PA) under the Improved Thermoelectrics Materials Program sponsored by the U.S. Department of Energy. Two of the alloys, 51B-5 and 51B-6, consisted of appropriate amounts of -325 mesh silicon powder (Aesar, 99.8%), -200 mesh germanium powder (Cerac, 99.999% stated purity), 6 mm GaP pieces (Cerac, 99.999% stated purity), and 3 mm P pieces (Cerac, 99.99% stated purity) ground and sieved to -200 mesh. These materials were ball milled in a helium-filled hardened tool steel vial. Another set of two, 51-30 and 51-31, were prepared by ball milling +20 mesh silicon chunks (Aesar, 6N), +20 mesh germanium chunks (Johnson Matthey, 5N), 6 mm GaP pieces (Cerac, 5N), and 3 mm P pieces (Cerac, 4N) under the same conditions. A third set of alloys, one of which was designated 51-37, was prepared using single crystalline, <111>-oriented, 1500 ohm cm, float zoned silicon as the starting material (Virginia Semiconductor, Fredricksburg, VA) along with the chunk Ge, GaP, and P as mentioned above. The alloys were all hot pressed at 1130°C for 45 minutes with an applied pressure of 138 MPa (22 ksi) under a vacuum of 1×10^{-7} Torr. One sample from each of the first two lots, 51B-6 and 51-31, was sealed in helium-filled fused silica ampoules and heat treated at 1100 °C for 3 h followed by an air cool. All compacts were sent, along with samples of the silicon powder and chunks, to IRT Corporation (San Diego, CA) for oxygen analysis by fast neutron activation. In this technique the sample is subjected to a neutron fluence of 1.5×10^9 neutrons/cm^2, which is well below the level at which radiation damage would be expected. After return of the samples, the alloys were characterized by optical metallography, scanning electron microscopy, x-ray diffraction, and scanning Auger microscopy. In addition, the mobility, carrier concentration, electrical resistivity, thermal conductivity, and Seebeck coefficient of each alloy were measured.

3.4. Results

The results of neutron activation analysis on samples of the -325 mesh silicon powder, chunk Czochralski silicon, single-crystal float zoned silicon, and a mixture of the

Table 1. Oxygen content of silicon powder, chunk silicon, single-crystal silicon, and alloy after various stages of processing. (Values are in parts per million atomic.)

Material	Powdered Si + Ge oxygen content	Chunk Si + Ge oxygen content	Single Crystal Si oxygen content
Si only	13340	1600	900
Si, Ge, GaP, P mixture	16500	800	... a
MA 6 h	22100	4600	... a
As-pressed	22200	5700	2500
Heat treated	23000	6000	

[a]Measurements were not performed during the intermediate stages.

components (pre-MA) and of the alloys after MA, hot pressing, and heat treatment are shown in Table 1.

The component silicon chunk material purchased as 5-9's pure contained substantially more oxygen than expected. During processing the largest single source of oxygen contamination appears to be the MA-to-hot pressing sequence where approximately 0.5% oxygen is picked up. The actual MA of the materials occurs under helium gas in a sealed vial. Little admission of atmosphere into the vial is expected due to an o-ring seal. Rather, the primary contributing factor of the oxygen pickup during this step is believed to be the glove box environment, which is introduced into the vial along with the starting materials, and within which the fine, post-MA powders are handled. The first two sets of alloys were handled in a glove box supplied with tank helium gas in which the moisture content was visually monitored using P_2O_5 powder. Additional sources of oxygen were present such as wiping tissue, weighing paper, and various plastic products. The alloys prepared from the float zoned silicon, however, were handled in a glove box supplied with higher purity helium in which all paper and plastic products had been removed. The moisture and oxygen contents of the gas were minimized by using the gettering effects of Linde 13X molecular sieve and zirconium/titanium alloy chips heated to 750°C, respectively. The oxygen pickup of alloys prepared in the low oxygen glove box amounted to only 0.16%. The hot pressing sequence appears to be only a minor source of oxygen in the powder specimen.

Scanning laser mass spectroscopy was used to determine trace impurities in the silicon powder, chunk silicon, and chunk germanium. The silicon powder was found to contain 700 ppma Fe, 56 ppma Al, 80 ppma Ca, and 5000 ppma K. In contrast, the chunk silicon contained less than 10 ppma non-oxygen impurities, the highest of which was 6 ppma Cu. It is worth noting that the chunk germanium was found to contain only 12 ppma oxygen and less than 1 ppma other impurities.

That the alloys have markedly different oxygen contents is evident from the photomicrographs shown in Fig. 1 of 5IB-5 (high oxygen) and 51-30 (intermediate oxygen). (The microstructure of the heat treated 5IB-6 and 51-31 alloys are indistinguishable from their shown counterparts.) There is a dramatic difference in microstructure and grain size; the high oxygen alloy contains grains so small that none are visible at 1000X while the intermediate oxygen alloy has well-defined grains of 3 to 18 μm in size. Most of these grains are in the 4 to 7 μm range. Another significant observation is the relatively clean grain boundaries of the intermediate oxygen alloy. There are few, if any, second phase particles observed. It is also interesting to note the occurrence of twinning in several of the grains. These may be annealing twins generated during hot pressing.

Two of the samples, 51B-5 (containing 2.2 a/o O) and 51-30 (containing 0.57 a/o O) were observed with a TEM. Images of the intermediate oxygen sample, 51-30, can be seen in Figs. 2 (a) and 2(b). As shown in the 18.5kX photograph in Fig. 2(a), the range of grain sizes in this material is about 0.8 to 2 μm. A number of inclusions are observed within the grains, whereas second phase particulates are not seen in the grain boundaries. Several dislocation tangles are observed within the upper-centered grain, and the dark lines in the grain boundaries are due to the thickness contrasts. Figure 2(b) shows a typical grain of the intermediate oxygen material at 60kX. The size of the large particles is about 35 nm, and the small particles are about 5 nm. Thickness contrast is observed in the grain boundary. The distribution of these inclusions is uniform within the grain. They could be SiO_2, Ga_2O_3, or P_2O_3, but no qualitative analysis was attempted. Figure 3 shows the corresponding image obtained on the high oxygen content sample (51B-5) in which a large number of second phase inclusions can be seen in the grain boundaries. The grain size of this alloy is

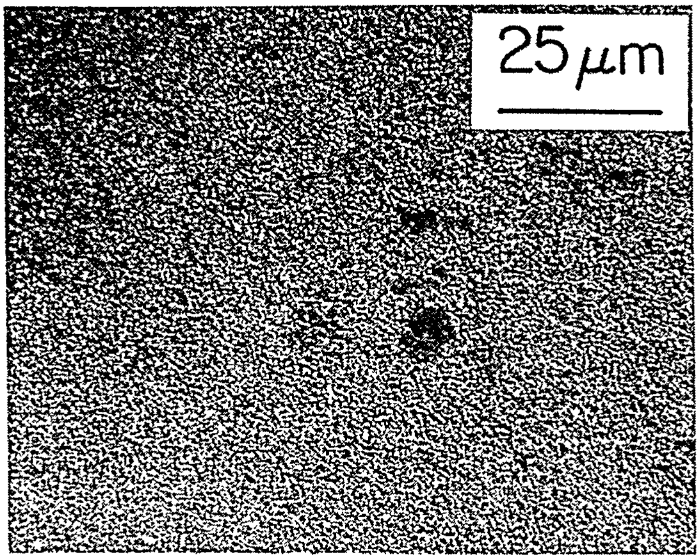

1 (a).

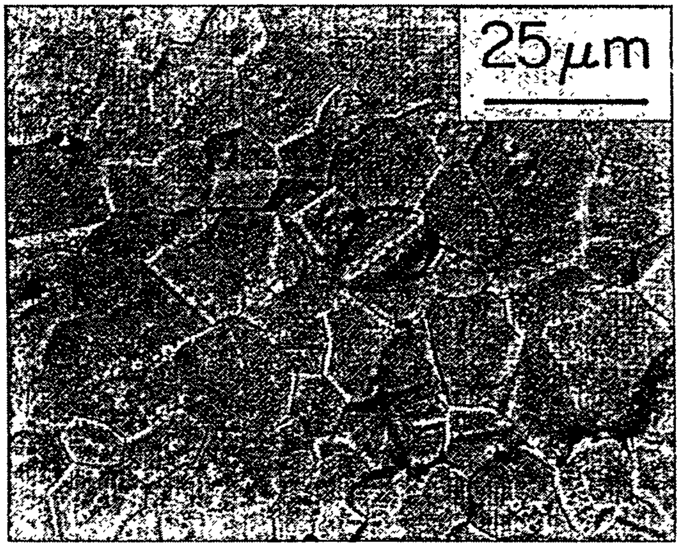

1 (b).

Fig. 1. Microstructure of n-type Si-20 at. % Ge alloys containing (a) 2.2 at. % oxygen and (b) 0.57 at. % oxygen.

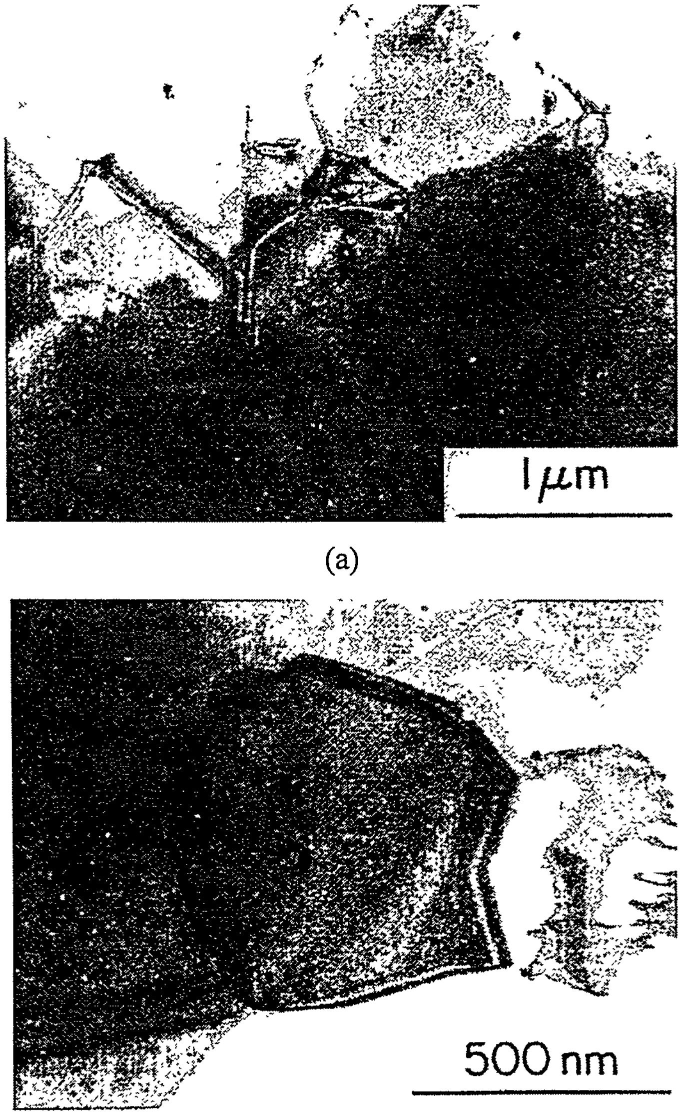

(a)

(b)

Fig.2. TEM images of n-type Si-20 at. % Ge alloy containing 0.57 at. % oxygen at (a) 18500X and (b) 60000X.

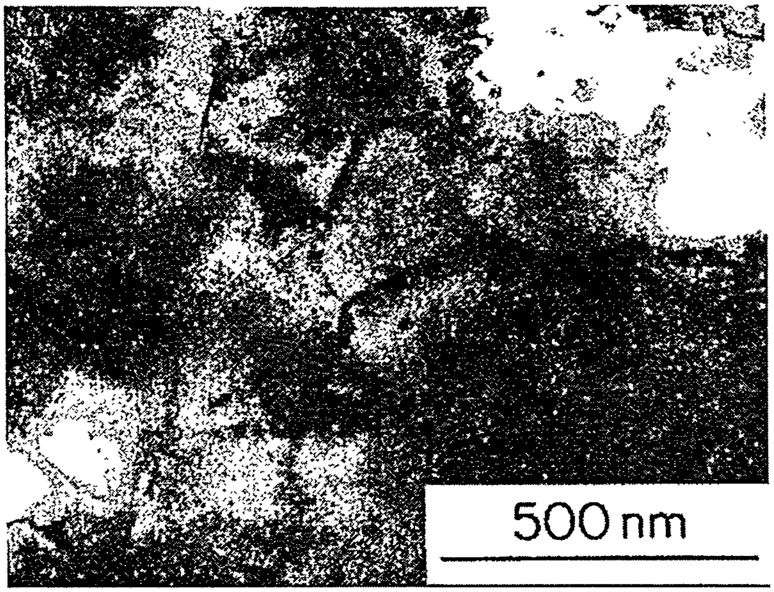

Fig. 3. TEM image of n-type Si-20 at. % Ge alloy containing 2.2 at. % oxygen.

considerably smaller than that of the low oxygen counterpart; there is a large fraction of grains in the 0.16 to 0.51 μm size range in this sample.

The size distribution of the inclusions is almost the same as that of intermediate oxygen material. A number of second phase inclusions are located within the grains as well as in the grain boundaries. The grain size of the high oxygen content alloy (51B-5) is relatively small compared to that of the intermediate oxygen material (51-30) because the second phase particles in the grain boundaries exert a restraining force upon the grain boundaries during grain growth. This kind of pinning force depends primarily on the size of the second phase inclusions and their number. As the oxygen content increases, the number of inclusions, related to the oxygen content, also increases.

The lattice parameter, a_0, of the two as-hot pressed and two heat treated alloys is shown in Table 2 along with that of the as-pressed alloy prepared from single-crystal float zoned silicon. The a_0 values deviate slightly from that of an ideal Si-20 at. % Ge alloy (0.5472 nm) (18). There is a systematic increase in the observed a_0 as the oxygen content is increased from 2500 to 22000 ppma. However, we believe the observed change in lattice parameter is due to the change in bulk composition and not a manifestation of oxygen in solution. According to the neutron activation analysis the high oxygen content alloys (51B-5/51B-6) have approximately 2 at. % more oxygen than the lowest oxygen alloys. If all excess oxygen (above the maximum solid solubility) is tied up as SiO_2, this would consume approximately 4 x 10^{20} silicon atoms per cm^3 which would in turn shift the overall composition of the alloy by a corresponding amount toward the germanium-rich end. Converting the lattice parameter data to composition and neglecting the effects of dopants yields an increase of the germanium to silicon ratio of 3 at. %.

Table 2. Lattice parameter data for high and low oxygen alloys (Nelson-Riley extrapolation).

Alloy	Oxygen Content (ppma)	a_o (nm)
51-37	2500	0.5464
51-30	5700	0.5466
51-31	6000	0.5466
51B-5	22000	0.5471
51B-6	23000	0.5470

The room temperature electrical properties of these alloys are shown in Table 3. As expected the high oxygen content alloys show a significant degradation in electrical mobility due to the larger number of scattering sites. This results in a significant degradation to the electrical power factor ($S^2\sigma$) which amounts to nearly 33% at higher temperatures. In general, the temperature dependence of the electrical conductivity and Seebeck coefficient follow the behavior measured at room temperature.

The thermal diffusivity, α_0, was measured as a function of temperature for these alloys and converted to thermal conductivity using the relation

$$\lambda = C_p d\alpha, \qquad (1)$$

where λ is the thermal conductivity, d is the density, and C_p is the heat capacity. For this study C_p values reported by Amano et al. (19) on Si-20 at. % Ge alloys doped with GaP and P

Table 3. Electrical properties of n-type $Si_{80}Ge_{20}$ alloys with different oxygen contents (25 °C).

Designation	Oxygen (at. %)	σ^a $(\Omega\text{-cm})^{-1}$ ($\times 10^3$)	n^b ($\times 10^{20}$ cm^{-1})	μ^c (cm^2/V-s)	S^d (μV/°C)
51-37	0.25	1.92	2.5	47.7	-88
51-30	0.57	1.63	2.1	50.2	-86
51-31	0.60	2.12	3.6	38.0	-68
51B-5	2.22	0.41	1.1	22.0	-110
51B-6	2.30	0.62	2.0	19.0	-93

[a] σ denotes electrical conductivity.
[b] n denotes carrier concentration.
[c] μ denotes carrier mobility.
[d] S denotes Seebeck coefficient

were used ranging from 0.6596 J g^{-1} deg^{-1} at 300°C to 0.7636 J g^{-1} deg^{-1} at 1000°C. Table 4 lists each alloy and corresponding λ at 300°C. The densities of all samples were found to be within 2% of the 3.0 g cm^{-3} theoretical density for this composition, The effect of the oxygen impurities is quite pronounced with a 25% to 30% reduction in λ in the alloys containing high oxygen levels. This is maintained throughout the temperature range 300 to 1000°C. There is a weak temperature dependence of λ up to 800°C above which there is a noticeable increase with temperature.

Table 4. Thermal conductivity of n-type $Si_{80}Ge_{20}$ alloys with different oxygen contents (T = 300 °C)

Alloy	λ (W/cm-°C)
51-37	0.046
51-30	0.044
51-31	0.045
51B-5	0.031
51B-6	0.033

3.5. Discussion

The search for materials having higher conversion efficiencies (i.e., figures of merit, Z) must involve an evaluation of the behavior of the fundamental physical parameters that affect Z. An understanding of these parameters is necessary in order to make meaningful comparisons between various materials or between similar materials processed under different conditions.

A useful way of examining the effect of oxygen on Z is to evaluate how the fundamental parameters of mobility, μ, and lattice thermal conductivity, λ_L, are themselves affected. Chasmar and Stratton introduced a parameter called β, which relates these variables to Z in a fundamental way. Specifically, in the single-band approximation for n-type conductivity with spherical energy surfaces, Z is proportional to β and

$$\beta = \frac{2(2\pi m^* k_B T)^{3/2} e}{h^3}\left(\frac{k_B}{e}\right)^2 \frac{T\mu}{\lambda_L} \qquad (2)$$

where T is the temperature, e is the electronic charge, k_B is Boltzmann's constant, and m^* is the effective mass. This expression can be simplified as

$$\beta = C(T)\frac{m^{*3/2}\mu}{\lambda_L} \qquad (3)$$

where

$$C(T) = \frac{2(2\pi k_B T)^{3/2} e}{h^3}\left(\frac{k_B}{e}\right)^2 T \qquad (4)$$

Larger $m^{*3/2}\mu/\lambda_L$ ratios would therefore suggest a higher Z. Table 5 shows the calculated ratio μ/λ_L at 300 °C for the five alloys studied along with the experimentally measured average figure of merit, Z, between 300 and 1000 °C (the normal operating temperature range of thermoelectric materials in space power generation converters). The band structure and hence the effective mass is expected to be unchanged by varying the oxygen content. The thermal conductivity was separated into its electronic polar, λ_P, and lattice components by the Wiedemann-Franz relationship using the Sommerfeld value of the Lorentz number, 2.45 x 10^{-8} $W\Omega/K^2$. Slack and Hussain point out that use of the classical value is reasonable even in a three-band conduction model. The bipolar term was taken as zero since the temperature is relatively low and little electron hole pair formation is expected. Moreover, the high doping level in these alloys is expected to quench the bipolar contribution. An assumption was made that the room temperature carrier concentrations are equal to those at 300 °C. Empirical data taken on heavily doped and hot pressed Si-Ge (GaP) alloys (22) show this to be a reasonable approximation. The mobility was then estimated by taking the 300 °C resistivity value and combining with the carrier concentration, e.g., $\mu = (\rho n e)^{-1}$. In each case the alloy with the lower oxygen content had a higher μ/λ_L ratio and a higher average Z. These results strongly suggest that a low oxygen alloy is desirable. The improvement in β (and hence Z) is due mainly to an improvement in mobility with lower oxygen. The λ_L values do not change significantly despite the large difference in microstructure. The magnitude of Z is strongly dependent on carrier concentration; the heat treatment applied to 51-31 has actually increased n beyond a range that yields a reasonable Seebeck coefficient. In fact, of the five alloys

Table 5. μ/λ_L ratios for oxygen analysis alloys (T = 300°C)
(<Z> is a 300 to 1000°C average expressed in °C x 10^{-3}).

Alloy	λ_{tot}[a]	λ_P[a]	λ_L[a]	μ/λ_L[a]	<Z>[b]
51-37	45.9	18.5	27.4	1.20	0.80
31-30	44.6	15.6	29.0	1.14	0.71
51-31	45.5	19.0	26.5	0.92	0.70
51B-5	31.2	5.6	25.6	0.88	0.60
51B-6	33.8	7.2	26.6	0.60	0.56

[a] λ in mW/cm-°C
[b] <Z> in $°C^{-1}$ x 10^{-3}.

studied only 51-37 has a room temperature carrier concentration in a suitable range so that the Seebeck coefficient (and hence Z) is maximized (23), which somewhat complicates the comparison between alloys. Nonetheless, the variation in n can ultimately be traced to differences in sintering characteristics, which themselves can be traced to the observed variation in oxygen content. One would likely observe higher overall Z values in alloys having somewhat less nominal phosphorus.

The 51B-6 alloy was heat treated in air at 1200 °C for 100 h in order to determine if an improvement in mobility would result. After heat treatment the room temperature Hall resistivity had decreased to 0.82 mΩ cm and the carrier concentration had increased to 2.45 x 10^{20} cm^{-3}. Assuming λ_L does not change significantly, the ratio μ/λ_L would increase to about 0.9, comparable to that of 51-31 but still lower than that of the lowest oxygen alloy.

As previously mentioned, the preparation of ultralow oxygen SiGe(GaP) by hot pressing fine powders is difficult. We have found that common, commercially obtained silicon can contain relatively high quantities of oxygen. Use of low oxygen starting materials coupled with careful handling of the powders provides a significant reduction in the oxygen content of the alloys we have investigated. Another factor that may add to the complexity of the understanding of the transport parameters is the possible presence of carbon in these samples. Analytical determination of carbon content by material combustion indicates that the fine grained, high oxygen content alloys may contain on the order of 2-3 at. % carbon, which is comparable to the total amount of oxygen determined by neutron activation. Certainly this much carbon, depending on the form, could have a significant impact on grain growth and carrier scattering. The large grained, intermediate oxygen alloys were found to contain only 0.1 at. % carbon. The question naturally arises: how high a purity is needed in order to obtain optimum properties? To address this question the dominant mechanism governing carrier mobility in semiconductors must be considered. According to Fistul (24), mobility, particularly at room temperature, is governed mainly by scattering on impurity ions. The effect of electrically active dopants produces impurity ions up to a level of 2-3 x 10^{20} cm^{-3}. Therefore, from the standpoint of impurity scattering, there may be only marginal benefits in reducing the total oxygen content much below this value. Certainly the benefits of trying to obtain an alloy with, say, 10^{16} to 10^{17} oxygen atoms per cm^3 (0.00002 to 0.0002 at. %) are questionable, particularly when considering the enormous effort required to reach this level. Moreover, the relatively high amounts of carbon found by SAM analysis has implications for grain boundary potential scattering of carriers and may cause a further reduction in mobility. The possible presence of carbon in these alloys is a topic that warrants deeper investigation. At any rate, the production of a hot pressed SiGe(GaP) alloy having a total oxygen content of approximately 10^{19} to 10^{20} cm^{-3} (0.02 to 0.20 at. %) would be very interesting and should provide additional information on the peak mobility characteristics of these heavily doped alloys. We have observed that there is little difference in the lattice thermal conductivity between the high and low oxygen alloys which suggests that there is no reason to expect improvements in performance by deliberately oxygenating alloys in an attempt to pin grain boundaries.

3.6. Conclusion

The oxygen content of five hot pressed SiGe(GaP) alloys was correlated with the fundamental thermodynamic parameters of carrier mobility, μ, and lattice thermal conductivity, λ_L. Oxygen levels of 0.25 to 2.30 at. % were measured by neutron activation. Increased levels of oxygen were observed to lower the μ/λ_L ratio by reducing carrier mobility. A decrease in total thermal conductivity with increased oxygen content was due to a reduction in the polar component.

3.7. Acknowledgments

The authors wish to thank Professor K. A. Gschneidner, Jr. for reviewing this manuscript and for his continued interest in high temperature thermoelectric materials research. The optical metallography performed by Hal Salisbury is gratefully acknowledged. The Ames Laboratory is operated or the U.S. Department of Energy by Iowa State University under Contract No. W-7405-ENG-82. This project was supported by the Office of Special Applications.

3.8. References

1. E. Skrabek, in Proceedings of the Seventh Symposium on Space Nuclear Power Systems, edited by M. S. El-Genk and M. D. Hoover (Institute for Space Nuclear Power Studies, Albuquerque, NM, 1990), p. 819.
2. C. Vining, in Proceedings of the Eighth Symposium on Space Nuclear Power Systems, edited by M. S. El-Genk and M. D. Hoover (American Institute of Physics, New York, 1991), p. 458.
3. G. L. McVay, R. A. Lefever, and R. J. Baughman, Mater. Res. Bull. **9,** 735 (1974).
4. N. Savvides and H. J. Goldsmid, J. Mater. Sci. **15**, 594 (1980).
5. C. M. Bhandari and D. M. Rowe, Contemp. Phys. **21**, 219 (1980).
6. C. B. Vining, W. Laskow, J. B. Hanson, R. R. Van der Beck, and P. D. Gorsch, J. Appl. Phys. **69,** 4333 (1991).
7. K. Owusu-Sekyere, W. A. Jesser, and F. D. Rosi, Mater. Sci. Eng. **B3,** 231 (1989).
8. U. Gosele and T. Y. Tan, Appl. Phys. **A 28**, 79 (1982).
9. N. Needels, J. D. Joannopoulos, Y. Bar-Yam, and S. T. Pantelides, Phys. Rev. **B 43**, 4208 (1991).
10. R. H. Doremus, J. Appl. Phys. **66,** 4441 (1989).
11. B. A. Cook, B. J. Beaudry, J. L. Harringa, and W. J. Barnett in Proceedings of the Ninth International Conference on Thermoelectrics, edited by C. B. Vining (Jet Propulsion Laboratory, Pasadena, CA, 1990), p. 234.
12. B. A. Cook, B. J. Beaudry, J. L. Harringa, and W. J. Barnett, in Proceedings of the Eighth Symposium on Space Nuclear Power Systems, edited by M. S. El-Genk and M. D. Hoover (American Institute of Physics, New York, 1991), p. 431.
13. J. S. Benjamin, Sci. Am. **5,** 40 (1976).
14. R. M. Davis and C. C. Koch, Scripta Met. **21**, 305 (1987).
15. R. Sundaresan and F. H. Froes, J. Met. **8**, 22 (1987).
16. F. H. Froes, J. Met. **41**, 25 (1989).

17. S. H. Han, K. A. Gschneidner, Jr., and B. J. Beaudry, Scripta. Met. Mater. **25**, 295 (1991).
18. J. P. Dismukes, L. Ekstrom, and R. J. Paff, J. Phys. Chem. **68**, 3021 (1964).
19. T. Amano, B. J. Beaudry, K. A. Gschneidner, Jr., R. Hartman, C. B. Vining, and C. A. Alexander, J. Appl. Phys. 62, 819 (1987).
20. R. P. Chasmar and R. Stratton, J. Electron. Control **7**, 52 (1959).
21. G. A. Slack and M. A. Hussain, J. Appl. Phys. **70**, 5 (1991).
22. J. Fluerial and B. Borshchevsky, in Proceedings of the Ninth International Conference on Thermoelectrics, edited by C. B. Vining (Jet Propulsion Laboratory, Pasadena, CA, 1990), p. 206.
23. J. W. Vandersande and J. P. Fleurial, MOD-RTG Thermoelectric Materials Meeting, Sept. 1991 (unpublished).
24. V. I. Fistul, <u>Heavily Doped Semiconductors,</u>1st ed. (Plenum, New York, 1969), p. 129.

CHAPTER 4. $Si_{80}Ge_{20}$ THERMOELECTRIC ALLOYS PREPARED WITH GaP ADDITIONS

A paper published in the Journal of Applied Physics 78 (1995) 5474 - 5480

B. A. Cook, J. L. Harringa, S. H. Han, and C. B. Vining

4.1. Abstract

Controlled amounts of GaP and P were added to a $Si_{0.8}Ge_{0.2}$ matrix by a powder-metallurgical technique in order to evaluate the optimum composition for thermoelectric applications. Bulk determination of the gallium and phosphorus content in fully dense, hot pressed compacts was performed by inductively-coupled plasma atomic emission spectroscopy. The transport properties of the compacts were characterized by Hall effect measurements at room temperature and by measurements of electrical resistivity, Seebeck coefficient, and thermal diffusivity to 1000°C. Considerable variation in the electrical transport properties were found to accompany changes in the Ga/P ratio, in the total amount of dopant, and changes in other preparation conditions. Alloys with gallium phosphide additions exhibit carrier concentrations higher than those obtained in alloys doped only with phosphorus. Alloys with a nominal phosphorus content greater than 2.0 at. % were found to be overdoped and those containing less than 0.6 at. % phosphorus were found to be underdoped relative to the material's maximum figure of merit. Room temperature electron mobilities greater than 40 cm^2/V-s were commonly obtained in samples with a carrier concentration of $3x10^{20}$ cm^{-3} or greater. A 300 to 1000°C integrated average figure of merit ($Z=S^2/\rho\Lambda$) of $0.93x10^{-3}$ $°C^{-1}$ was achieved within an optimum composition range of 0.8 to 1.2 at. % P and 0.6 to 0.8 mole % GaP, which is 20 percent higher than current n-type Si-Ge alloys doped with 0.59 at. % P as used in the Voyager, Galileo, and Ulysses missions.

4.2. Introduction

Since Steele and Rosi (1) first demonstrated the remarkably low thermal conductivity of silicon-germanium solid solutions, efforts to better understand and optimize these alloys for use in thermoelectric applications have continued. The early work of Dismukes, et al.(2), provided an extensive background of both electrical and thermal properties of heavily doped, silicon-rich alloys and formed the groundwork for subsequent enhancements. Processing methods have since received considerable attention such as the application of hot pressed and sintered alloys (3), the study of grain-boundary scattering and the use of fine-grained alloys designed to lower the lattice thermal conductivity (4,5), application of high-temperature heat treatments to alter the microstructure and redistribute dopants (6,7), and control of second-phase oxygen (8). Moreover, the effects of gallium phosphide additions, once thought to reduce the thermal conductivity (9) and later identified as a mechanism to increase the solid solubility of phosphorus (10), have had considerable impact on the evolution of high performance Si-Ge thermoelectric alloys. The present state of theoretical modeling of the n-type $Si_xGe_{(1-x)}$ system suggests that the optimum dimensionless figure of merit (ZT) at 1300K is in the range of 1.1 ($Si_{0.8}Ge_{0.2}$) (11) to 1.2 ($Si_{0.7}Ge_{0.3}$) (12), without the introduction of artifacts such as inert, nanophase phonon scattering inclusions. Standard zone-leveled Si-Ge n-type alloys, doped only with phosphorus, have a ZT value 17-20% lower than the theoretical maximum. Recent experimental data on n-type alloys containing small (< 5 mole %) additions of GaP indicate that these additions can increase ZT_{max} to values near 1.0. Further improvements require optimization of the Ga/P ratio and control of the resulting microstructure.

Initial studies on the application of mechanical alloying (MA) for the preparation of n-type $Si_{80}Ge_{20}$ were performed on alloys with nominal 1.6 mole % GaP and 3.4 atomic % P additions (8). Analysis of the electrical properties of these alloys showed that while the high carrier concentration (3.5 to 4.2×10^{20} cm^{-3}) resulted in low electrical resistivities and electrical power factors close to the theoretically predicted maximum of 40 to 45 $\mu W/(cm\text{-}°C^2)$ at 600°C, it concomitantly causes a sharp decrease in power factor between 600°C and

1000°C. This rapid decrease in power factor causes a decrease in Z at the highest temperatures. An alloy having a lower carrier concentration, n, but higher carrier mobility should also provide low resistivity but in addition would possess an enhanced Seebeck coefficient, S, due to the logarithmic dependence of S on n.

A study was initiated to investigate the effects of the relative amount of gallium and phosphorus on the electrical and thermal properties of $Si_{80}Ge_{20}$ alloys and to improve the performance of the material in the 600°C to 1000°C range, while maintaining the high power factors observed near 600°C in the overdoped alloys. This paper summarizes efforts to identify the variables associated with the optimization of n-type $Si_{80}Ge_{20}$ alloys containing GaP and P as prepared by MA and hot pressing.

4.3. Experimental Details

Silicon-germanium alloys doped with gallium phosphide and phosphorus were prepared by a solid state reaction between stoichiometric quantities of elemental silicon, germanium, gallium phosphide, and phosphorus in a hardened tool-steel vial under a high-purity helium environment using a Spex 8000 high-energy vibratory mill. The Si and Ge were mixed in an 80:20 ratio and varying amounts of GaP and P were added to each charge. Table 1 lists the nominal dopant additions along with the nominal Ga/P ratios. The sample designated A94 was prepared with GaP only, in order to observe the amount of dissociation occurring between the gallium and phosphorus during preparation. Once the reaction was completed, as verified by X-ray diffraction, the powder was transferred to a graphite-lined die under helium and hot pressed at 1130 ^{o}C with an applied pressure of 140 MPa (22 ksi) under a vacuum of $1x10^{-7}$ Torr. The hot pressing time was typically 45 minutes, although some of the alloys (which are discussed separately below) were hot pressed for longer times in order to evaluate the impact of grain growth.

Samples for studies of Seebeck coefficient, electrical resistivity, Hall effect, thermal conductivity and metallographic and chemical analysis were cut from each hot pressed compact. Some of the samples were measured in an "as-pressed" condition after furnace-

Table 1. Sample identification and nominal compositions.

Sample ID	at. % P	at. % Ga	Ga/P
A90	1.25	0.50	0.40
A91	2.00	1.00	0.50
A92	1.88	0.63	0.33
A93	2.50	1.25	0.50
A94	1.60	1.60	1.00
A95	2.75	1.25	0.45
A96	3.00	1.25	0.42
A97	2.20	1.08	0.50
A98	1.90	0.80	0.42
A99	3.00	0.75	0.25
STD-1	1.10	0.00	0.00
STDM-4	3.40	0.00	0.00

cooling to ambient, while others were subjected to a thermal "reset" treatment at 1050°C for 20 minutes followed by air cooling. This temperature roughly corresponds to the point of maximum solubility of phosphorus in $Si_{80}Ge_{20}$ and facilitates comparisons between electrical resistivity and carrier concentration from sample to sample.

The room temperature carrier concentrations and Hall mobilities were measured on thin (0.1 cm) disks using the van der Pauw method (13) with four-point contacts equally spaced around the perimeter. The procedure described by Ndlela and Bates (14) was used in this study. A magnetic field of 1 T was applied during which time a minimum of four voltage readings were obtained and subsequently averaged for each of the four current directions. The field was reversed and the voltage samplings repeated. The intermediate Hall coefficients were averaged and the carrier concentration was determined from the relation $n = (R_He)^{-1}$. The accuracy of this technique is estimated at better than 1 percent of the true value. The electrical resistivity and Seebeck coefficient measurements were performed by a standard dc four-point probe technique (15) and by determination of the slope of the thermal emf versus temperature plot (16), respectively. Both properties were measured simultaneously on the same sample in a vacuum chamber (~ 10^{-7} torr) in the temperature range of 25 - 1000°C by a computer-controlled data acquisition system. A fifth-order polynomial regression was used to calculate the integrated power factors in the temperature range of 300 to 1000°C. The thermal diffusivity of a 1.27 cm diameter by 0.1 cm thick disk of the A92β sample was measured from 300°C to 1000°C by a standard laser flash diffusivity technique described in a previous publication (17). Briefly, both faces were coated with a thin (30μm) layer of graphite, and the sample was mounted in a low thermal conductivity holder machined from low density ZrO_2. The sample was placed in the center of a BN tube which was wound with Ta wire. This heater assembly was positioned inside a vacuum chamber such that a pressure of less than 10^{-7} Torr was maintained during the characterization. The front surface of the sample was irradiated by a pulse from a ruby rod laser. The zirconia sample holder minimized conductive heat losses from the material and the thermal transient was measured using an InSb detector. Corrections for finite pulse width and heat loss were applied using an in-house computer program. Thermal diffusivity values were calculated for each 5% rise in temperature between 5% and 95% of the maximum value. An average thermal diffusivity was then determined from these values. The thermal conductivity was determined from the product of the thermal diffusivity, density, and specific heat. Published data (18) were used for the thermal expansion coefficient and heat capacity.

4.4. Results and Discussion

The total bulk phosphorus and gallium contents of several hot-pressed compacts were determined by inductively coupled plasma - atomic emission spectroscopy (ICP-AES) and the results are summarized in Table 2. Total phosphorus loss consistently exceeded that of the gallium so that the actual Ga/P ratio was greater than the nominal value. This was not unexpected due to the high vapor pressure of phosphorus over silicon and germanium and the likely formation of a small amount of phosphorus vapor during MA. Based on these and also

Table 2. ICP-AES determination of P and Ga contents of several $Si_{0.8}Ge_{0.2}$ alloys.

Alloy ID	Nom. Ga (%)	Nom. P (%)	Nom. Ga/P	Actual Ga (%)	Actual P (%)	Actual Ga/P	Ga/P diff. (%)
A90α	0.50	1.25	0.40	0.49	1.10	0.45	11
A91α	1.00	2.00	0.50	0.93	1.56	0.60	19
A91γ	1.00	2.00	0.50	0.93	1.43	0.65	30
A92α	0.63	1.88	0.34	0.59	1.28	0.46	38
A93α	1.25	2.50	0.50	1.16	1.87	0.62	24

previous results, a difference of 40% between the nominal Ga/P ratio and the measured value appears to be an upper limit.

As the amount of excess phosphorus (i.e. above the solubility limit) is increased, there is a greater probability that partial liquefaction of SiP may occur during hot pressing, thereby increasing the rate of grain growth through liquid-phase sintering. According to the equilibrium phase diagram, SiP melts at 1131°C, which is within temperature-measurement error of the point at which these alloys were consolidated. Parallel studies on alloys doped only with phosphorus show strong correlation between grain size after hot pressing and the amount of phosphorus present in the bulk. Similar results are observed in these alloys although the presence of GaP complicates the comparisons. Of the alloys hot pressed for 45 minutes, the material with the smallest grain size, 0.5 to 1.0 μm, (A90α) contains 0.61 % P and 0.49 % GaP (Ga/P = 0.45). Significantly larger grains, on the order of 10 μm, are found in the A93α alloy, which contains 0.71 % P and 1.16 % GaP (Ga/P = 0.62). Consideration of the remaining alloys indicates that the A96 and A99 materials have the largest grain size, on the order of 20 to 25 μm each.

Hot pressing time can also have a strong influence on microstructure. To illustrate this effect, three compacts were prepared from the initial A92 charge. One each was hot pressed for 45, 60, and 75 minutes with a corresponding grain size progression of 0.5 to 1.0 μm, 5 to 10 μm, and 15 to 25 μm, respectively. As will be shown, microstructure can play an important role in the electrical transport of these alloys due to the existence of electrical potential barriers at the grain boundaries.

The impact of doping and microstructure on carrier mobility is shown in Fig. 1. The data points shown in the figure correspond to all samples prepared for this study, regardless of prior thermal history. The solid line labeled "Dismukes" represents the mobility of zone-leveled $Si_{0.8}Ge_{0.2}$ for samples doped with phosphorus up to about 2 x 10^{20} cm^{-3} (2), and the dashed line represents an extrapolation of those results to higher doping levels. The alloys near the upper right hand corner of Fig. 1, i.e. toward higher values of n and μ, tend to have a larger grain size than those with lower carrier concentrations, and this is believed to be a key factor as to why they have superior mobility. X-ray diffraction analysis indicates that the actual ratio of silicon to germanium was within 3% of the nominal 80:20 value based on lattice parameter determination.

That longer hot pressing times have a significant effect is seen by comparing the A92-alloys A92α, A92β and A92γ in reset condition (■), all corresponding to the same composition. Alloy A92α at (■, 2.8x10^{20}, 37.7) corresponds to a 45-minute hot pressing time while alloys A92β (■, 3.08x10^{20}, 40.0) and A92γ (■, 3.10x10^{20}, 42.1) correspond to 60-minute and 75-minute hot pressing times, respectively. The latter two points lie on the dashed line, corresponding to the highest mobility expected in $Si_{0.8}Ge_{0.2}$ for a given carrier concentration. In fact, several combinations of composition and hot pressing conditions are seen to yield points on the extrapolated Dismukes mobility curve. However, as mentioned previously, alloys with an excessively large carrier concentration will tend to have low Seebeck coefficients and less than optimal electrical power factors (S^2/ρ). For example, the A96β alloy (■), with 1.75 at. % P and 1.25 mole % GaP is overdoped, having a room temperature carrier concentration of 3.8x10^{20} cm^{-3}.

The effect of the 20-minute thermal treatment at 1050°C is clearly observed in the figure. For instance, alloy A92α in the as-pressed condition (which means the sample was cooled from the hot pressing temperature to ambient at the natural cooling rate of the furnace)

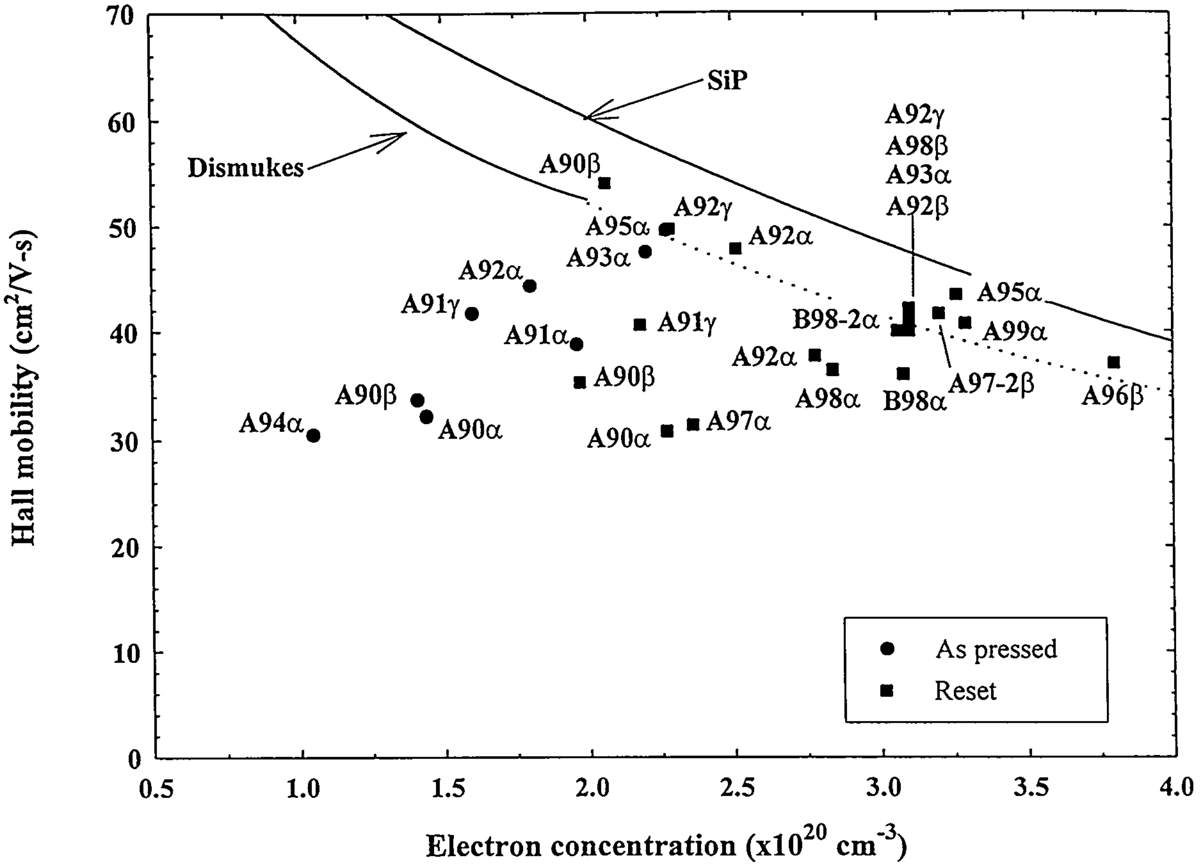

Fig. 1 Room-temperature Hall mobility as a function of measured carrier concentration. The mobility of phosphorus-doped Si is indicated by the solid line labeled SiP. The mobility of zone-leveled $Si_{0.8}Ge_{0.2}$ (Ref. 2) is indicated by the solid line up to n=2x10^{20} cm^{-3}, which has been extrapolated to higher carrier-concentration values, as indicated by the dashed line.

is represented by a solid circle (●), while the same sample following the thermal “reset” treatment is represented by a solid square (■). Another example is illustrated by the transformation of the A93α sample from the as-pressed condition (●) to the thermal “reset” (■) condition. In general, we have observed that this type of thermal “reset” shifts the carrier concentration along a path roughly parallel to the extrapolated Dismukes mobility curve.

It is also observed that there is a significant amount of dissociation between the gallium and the phosphorus from the GaP additive during processing, as is seen by examining the sample A94α. This alloy was prepared with 1.6 mole % GaP and no elemental phosphorus, in order to observe the degree to which dissociation takes place. If no dissociation of the GaP had occurred, the observed carrier concentration would be dominated by trace impurities in the starting materials, perhaps on the order of 10^{15} to 10^{16} cm^{-3}. However, since phosphorus is much more soluble than gallium in SiGe, dissociation of the GaP is expected to result in an n-type doping due to the phosphorus going into solution. In particular, sample A94α has a room-temperature carrier concentration of $1.1x10^{20}$ cm^{-3}, which corresponds to roughly 15 % dissociation of what is estimated to be the actual GaP content of the compact (taking losses into account).

The temperature dependence of the electrical resistivity, ρ, and Seebeck coefficient, S, of these alloys are shown in Figs. 2 and 3. The figures distinguish those samples which were measured in the as-pressed condition (Figs. 2a and 2b) from those which were thermally "reset" prior to measurement (Figs. 3a and 3b). Table 3 lists the integrated average resistivity, Seebeck coefficient, and power factor of these alloys between 300°C and 1000°C. The resistivities of all alloys to which elemental phosphorus had been added show a characteristic decrease with temperature above 800°C. While this might seem to be due to thermal excitation of electron-hole pairs, a simple calculation of the density of thermally activated electrons in the conduction band of a semiconductor with an energy gap of 1.1 eV yields a value of ~ 10^{18} cm^{-3} at 1000°C, which is on the order of 1% of the density of ionized impurity carriers. Thus, the 'turn-down' at high temperatures is more likely due to the effects of increasing solubility of phosphorus with temperature.

Complicating the interpretation of these results is the inherent 'metastability' of heavily doped Si-Ge alloys with time at elevated temperature due to the tendency for dopant precipitation. Each curve represents the combined effects of ionized impurity scattering, which is a thermally activated process, and dopant precipitation. The measurements of electrical resistivity and Seebeck coefficient were performed simultaneously on each sample and required 6 to 7 hours for a complete excursion from room temperature to 1000°C. In measurements of the dependence of carrier concentration on time at temperature, we have found that similarly doped samples show a decrease of 40% in carrier concentration after only 70 minutes at 600°C and approach a limiting decrease of 74% after 4000 hours. The electrical resistivity and Seebeck coefficient of the samples that had been thermally 'reset' tend to lie in a much narrower range than for those samples which were measured following a furnace cooling; in those samples significant dopant precipitation would have occurred.

The electrical power factor (S^2/ρ) of these alloys is expected to depend on the total amount of dopant added and on the Ga/P ratio, which is a measure of the amount of GaP in a sample. These effects are illustrated in Figures 4 and 5. Figure 4 shows the average power factor as a function of Ga/P ratio. The data do not follow any simple trend, which illustrates that the amount of GaP added to SiGe may not by itself be a strong predictor of a high power factor. Other factors must also be considered. Indeed, two samples of SiGe containing no gallium at all exhibit power factor values not much lower than the highest values obtained in this study.

In Figure 5 the average power factor is plotted as a function of the average Seebeck coefficient. Again, the results do not follow any simple relationship, indicating that additional factors such as processing variations and measurement errors may be significant. But the Seebeck coefficient is directly related to the carrier concentration and is therefore expected to provide an indication of the total amount of dopant in solution. And in spite of considerable scatter in the results, Fig. 5 nevertheless indicates that SiGe with GaP additions can achieve significantly higher carrier concentration values (as indicated by the lower

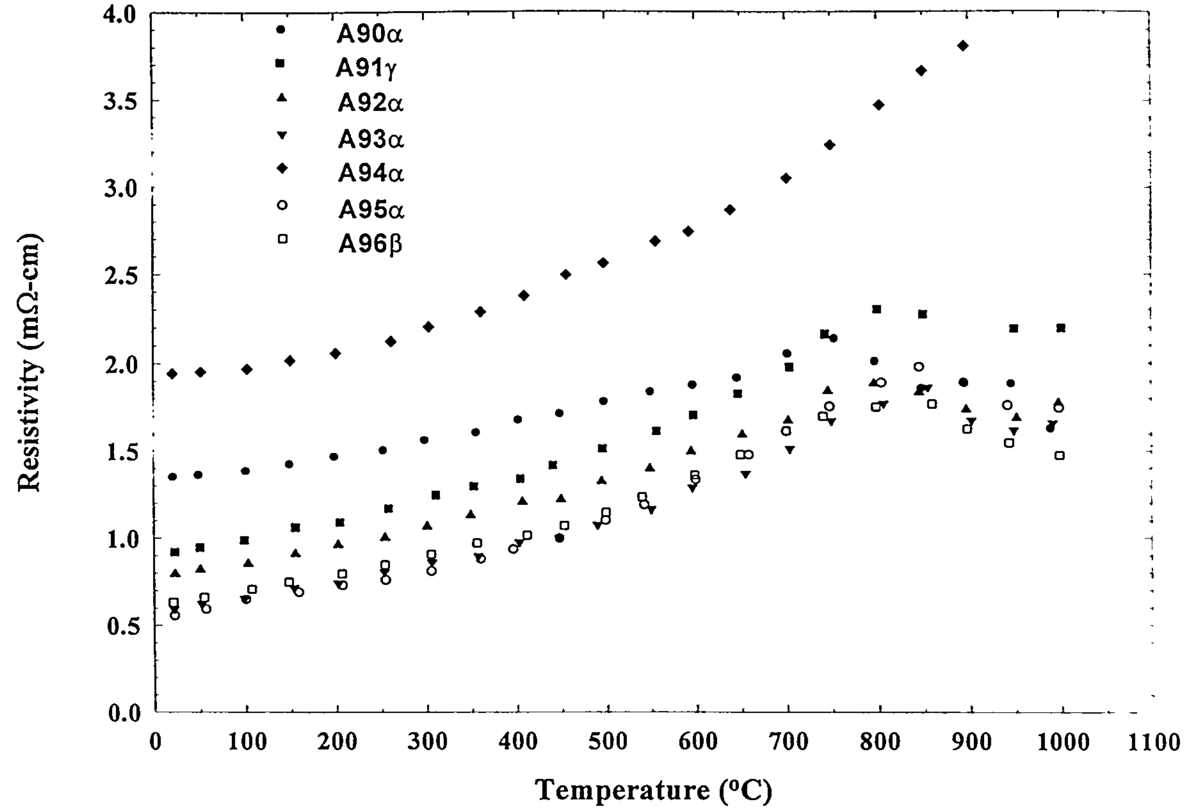

Fig. 2(a). Resistivity of selected "as-pressed" Si80Ge20 alloys containing various amounts of GaP and P.

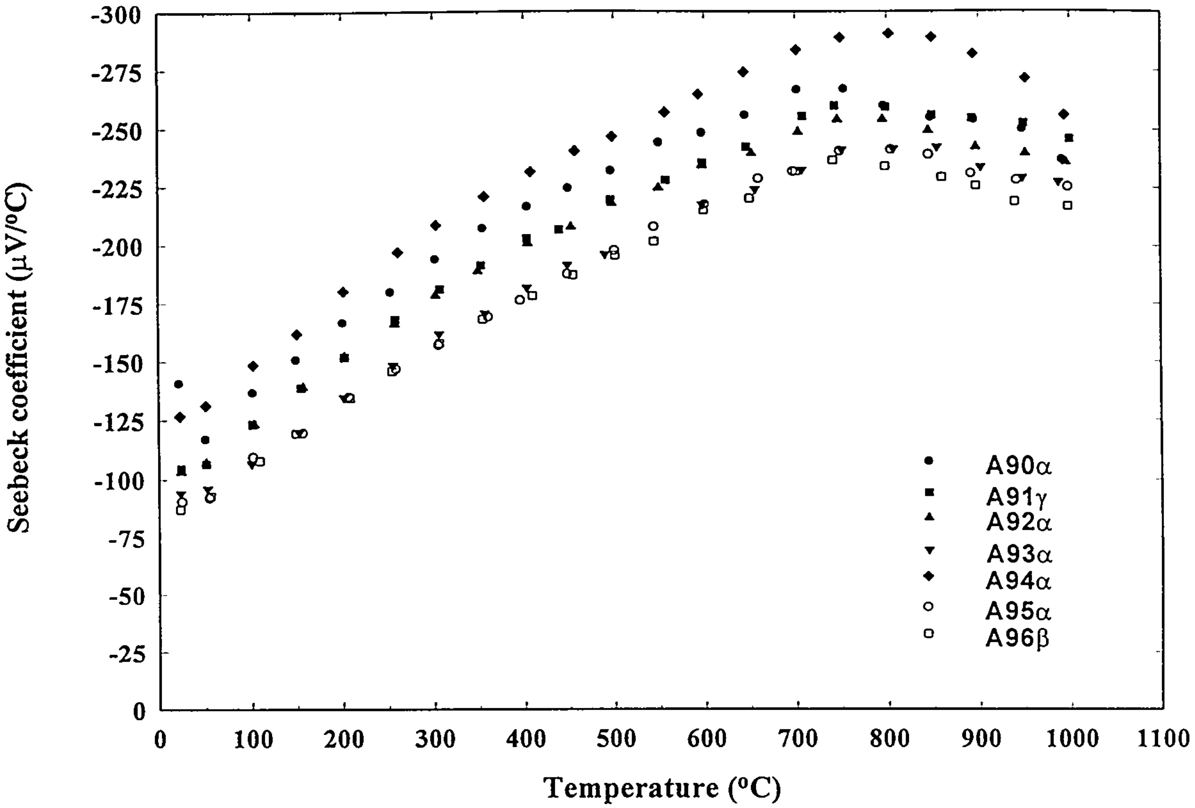

Fig. 2(b). Resistivity of selected "as-pressed" $Si_{0.8}Ge_{0.2}$ alloys containing various amounts of GaP and P.

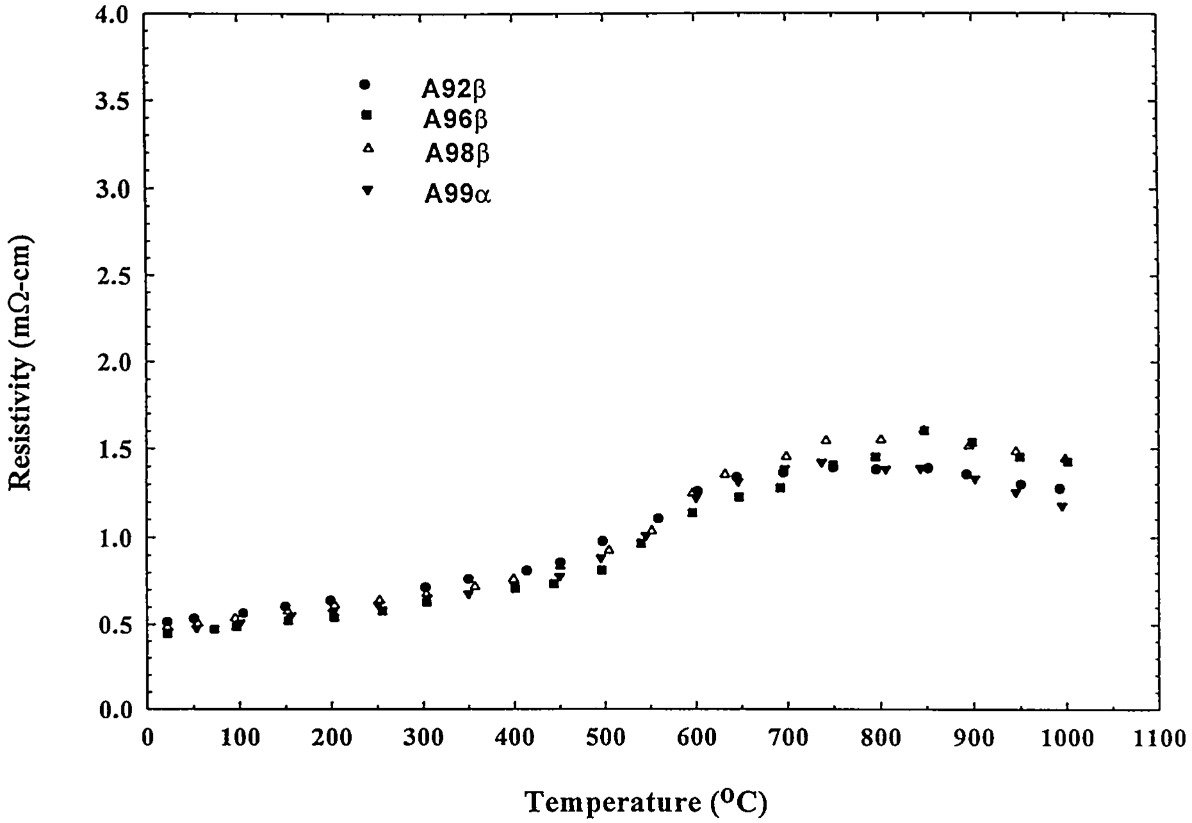

Fig. 3(a). Electrical resistivity of selected $Si_{0.8}Ge_{0.2}$ alloys containing various amounts of GaP and P and thermally treated ("reset") for 20 minutes at 1050°C prior to measurement.

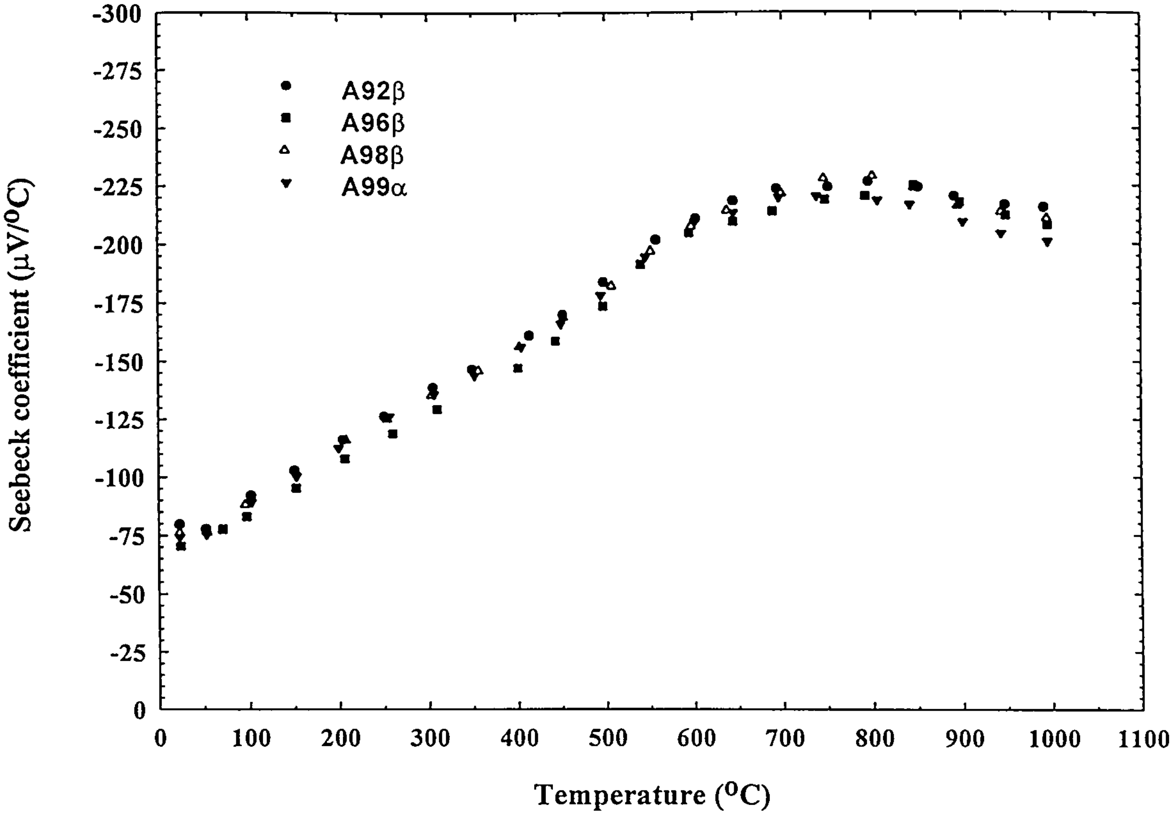

Fig. 3(b). Seebeck coefficient of selected $Si_{0.8}Ge_{0.2}$ alloys containing various amounts of GaP and P and thermally treated "reset") for 20 Minutes at 1050°C prior to measurement.

Table 3. Integrated average power factors (S^2/ρ) between 300°C and 1000°C of n-type $Si_{80}Ge_{20}$ alloys prepared with varying amounts of GaP and P. (Hot pressed 45 min. except where noted.)

Sample ID	Thermal History	<ρ> (mΩ-cm)	<S> (μV/°C)	<PF> (μW/cm-°C^2)
A96β	as pressed	1.394	-209.5	31.9
A95α	as pressed	1.434	-213.6	32.7
A94α	as pressed	3.034	-262.0	23.1
A93α	as pressed	1.368	-213.7	34.0
A92α	as pressed	1.538	-229.4	34.5
A91γ	as pressed	1.834	-234.3	30.4
A91α	as pressed	1.652	-217.6	29.1
A90α	as pressed	1.844	-242.7	32.0
A99α	reset	1.132	-195.0	34.3
A96β	reset	1.151	-193.9	33.4
A95α	reset	1.212	-203.3	35.1
A93α	reset	1.171	-205.5	36.6
A92α	reset	1.375	-205.6	31.3
A98β (60 min)	reset	1.229	-198.6	32.9
A92β (60 min)	reset	1.167	-200.5	34.7
A92γ (75 min)	reset	1.236	-201.0	33.0
A92γ (75 min + 20 hour heat treatment at 1225°C)	reset	1.443	-212.6	31.6
STD1-1	as pressed	1.556	-226.4	33.1
STDM-4	as pressed	1.43	-222.2	34.8

Seebeck values) compared to doping with phosphorus alone. This is particularly true for samples which have been thermally "reset". Figure 5 also suggests that the power factor decreases with average Seebeck values below about 205 to 210 μV/K, which is consistent with theoretical expectations.

Fig. 6 shows a typical microstructure of two alloys which were found to have nearly identical room temperature carrier concentrations: A90α, with an average grain size of 1 μm, and A95α, with an average grain size of 25 to 30 μm.

Since the mean free path of carriers at 300K is estimated to be on the order of 10 nm, one might expect little effect of grain size on mobility unless the material were truly "nanostructural". However, as Fig. 1 clearly shows, this is not the case, as there is nearly a 37% reduction in mobility, apparently due to the fine grain size of the A90 material. In general, the results from this study suggest that samples with low mobility values tend to have small grain sizes that are nevertheless considerably larger than the estimated mean free path.

Slack and Hussain (12) treated the effects of electrical potential barriers at grain boundaries using the approach of Murota and Sawai (19). They concluded that a significant (i.e., 20 to 40%) reduction in mobility could be expected to accompany a decrease in grain size from that of an infinitely large-grained crystal to 1 μm. Indeed, applying the Murota and Sawai relationship between grain size, L, effective width of the grain boundary, W (composed of two parts, that of the disordered region and that of the charge depletion region on each side of the boundary), the magnitude of the electrical resistance at the boundary, R_b, and the resistivity of a similarly-doped crystal of infinite grain size, $\rho(\infty)$, given by

$$\rho = \rho(\infty)\left(\frac{L}{L-W}\right) + R_b\left(\frac{L}{(L-W)^2}\right) \qquad (1),$$

one finds that the observed mobility values in this study are consistent with a grain boundary potential barrier of ~ 2.0×10^{-8} Ω-cm^2 . This value assumes a $\rho(\infty)$ of 5.6×10^{-4} Ω-cm (corresponding to a similar doping level) and a conservative estimate of 10 nm for the width

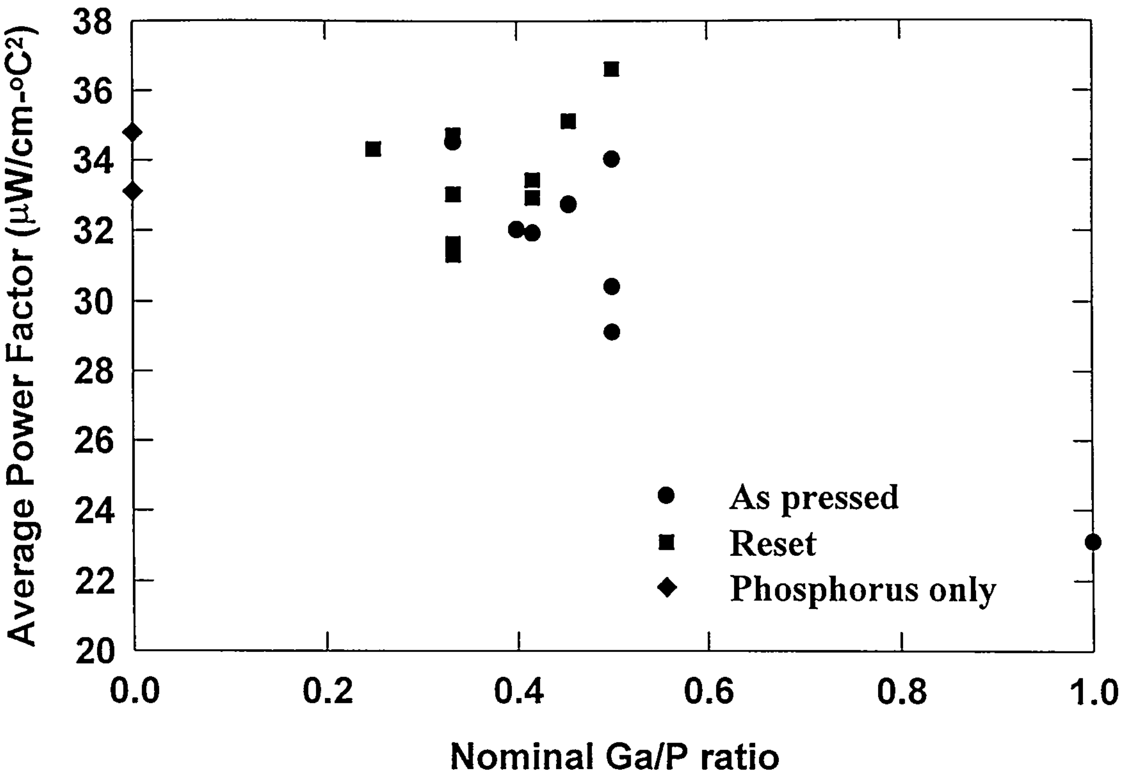

Fig. 4. Power factor (averaged between 300 and 1000 °C) as a function of nominal ratio of gallium to phosphorus for Si-Ge alloys doped with GaP (squares and circles) and doped with phosphorus only (diamonds).

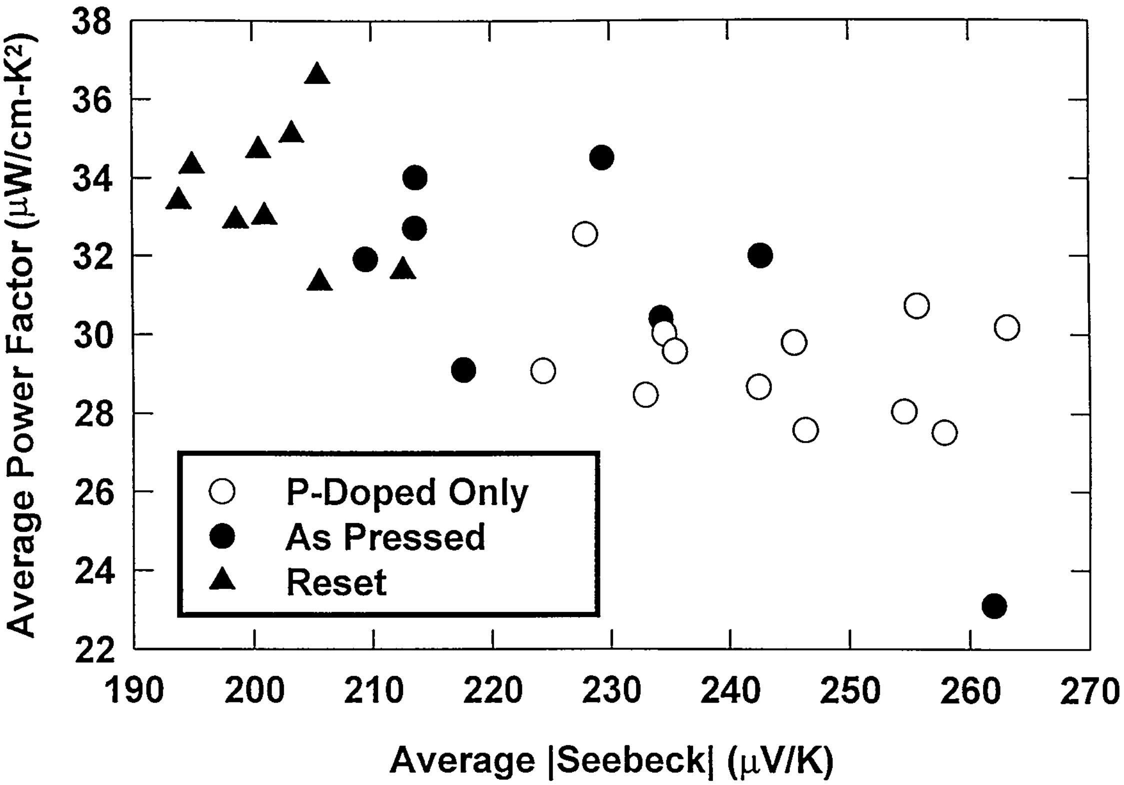

Fig. 5. Power factor as a function of Seebeck coefficient (both averaged between 300 and 1000 °C) for Si-Ge alloys with GaP (solid symbols) and doped with phosphorus only (open circles).

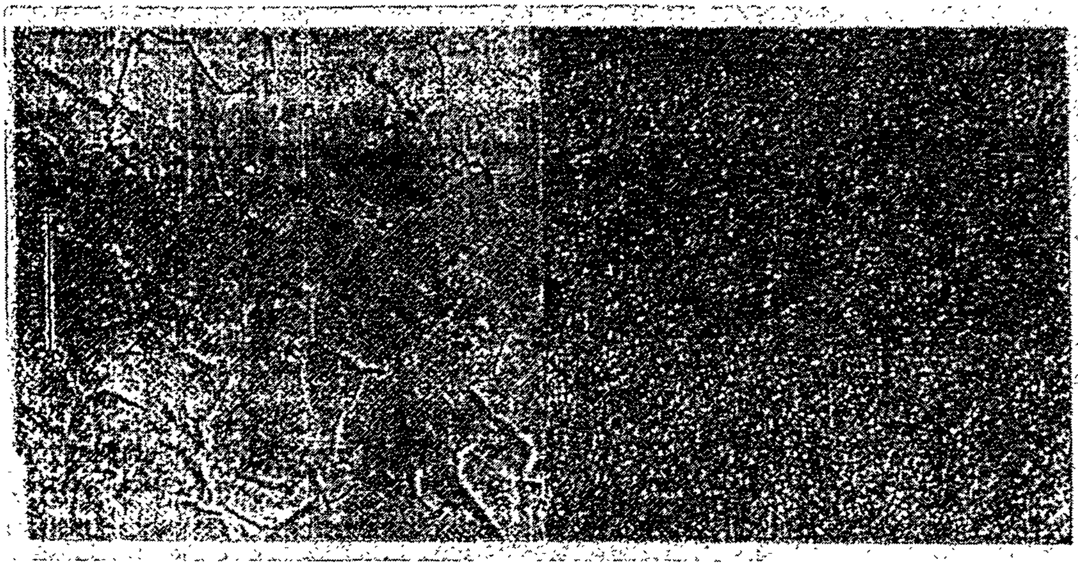

Fig. 6. Optical metallograph of two alloys having different nominal doping levels but similar electron concentrations. (Left: A95α prepared with 2.75 at. % P and 1.25 at. % Ga, Right: A90α prepared with 1.25 at. % P and 0.50 at. % Ga) (Reference scale= 25 microns)

of the grain boundary region, W. The value of $R_b = 9.6x10^{-8}$ Ω-cm^2 used by Murota and Sawai and by Slack and Hussain corresponded to oxygen-free silicon, and one would expect a lower potential barrier in such materials. An increasing amount of second-phase oxygen would be expected to increase the electrical barrier potential, thereby decreasing the mobility for a given grain size. Formation of scattering sites as a result of the second-phase oxygen is expected to be a relatively minor contribution to the carrier scattering. The total oxygen content of these alloys is estimated as 0.6 to 0.8 atomic percent, based on the results of neutron-activation analyses performed on similar samples prepared from the same starting materials. The room-temperature Seebeck coefficients of the aforementioned alloys were found to be similar, as expected: -90.4 μV/°C for the A95 material and - 88.4 μV/°C for the A90 sample. The results of this study tend to confirm Slack and Hussain's contention that large-grained, low-oxygen alloys are more desirable for thermoelectric applications at high temperature than fined-grained materials.

Since the mobility of many samples in this study approaches the values extrapolated from zone-leveled samples, it is unclear how much additional improvement in mobility (if any) would result by further reductions in the oxygen level. However if the trend established for the more heavily doped n-type alloys applies here, an additional improvement of 5 to 10 percent in power factor should be possible by using float-zoned silicon as the starting material, which would translate to an average power factor of 38 μW/(cm°C^2) between 300 and 1000°C. This value would agree with most theoretical models, which predict an optimum power factor near 40 μW/(cm°C^2) for the silicon-germanium system.

The thermal diffusivity of an alloy showing one of the highest power factors in this study, A92β, was measured from 300 to 1000°C. The thermal conductivity, Λ, calculated using the density, measured diffusivity and extrapolated specific heat values, is shown in Fig. 7. The integrated average thermal conductivity between 300 and 1000°C was determined to be 37.5 mW/(cm°C), which, when combined with the electrical data, gives an integrated average figure of merit ($Z = S^2/\rho\Lambda$) of $0.94x10^{-3}$ °C^{-1} and a maximum ZT of 1.1 at 1000°C. The figure of merit curve for this material is also shown in Fig. 7. Not only is the average Z

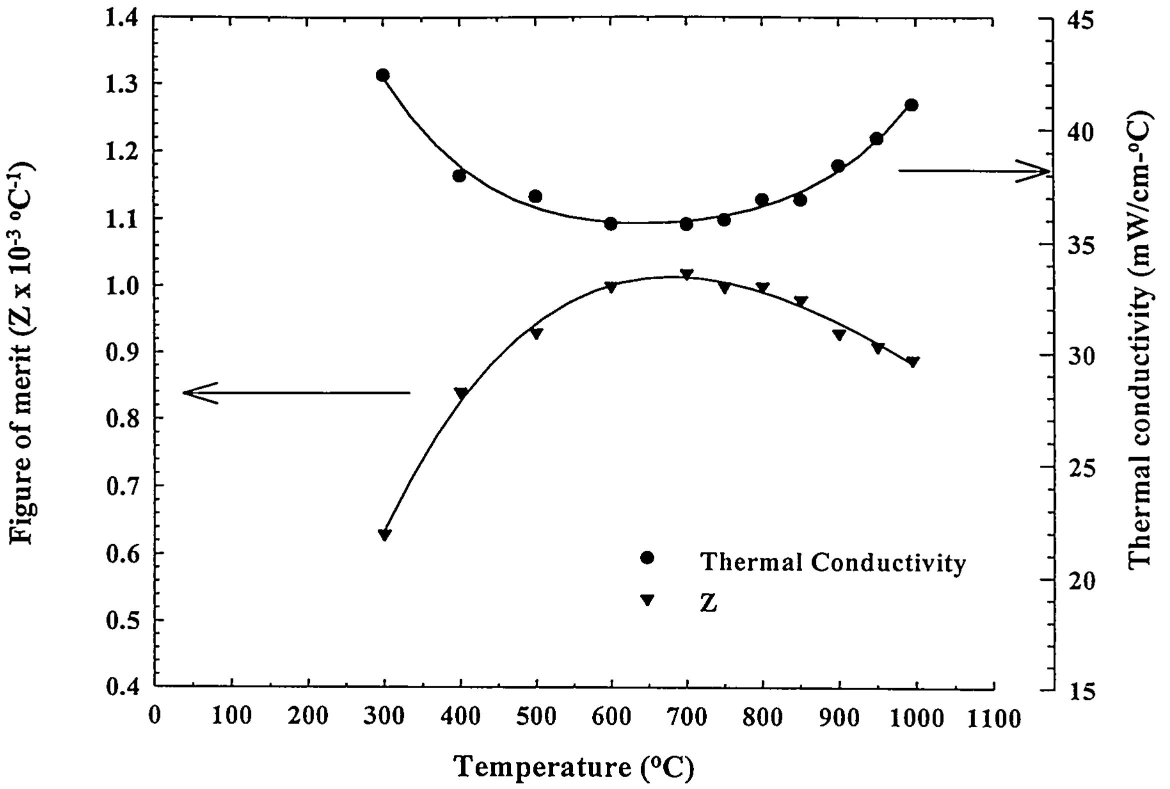

Fig. 7. Thermal conductivity (circles) and figure of merit (triangles) of A92β. (Nominal composition 0.63 mo. % GaP and 1.25 at. % P).

higher than that for the more heavily doped samples discussed in the introduction, the rate at which Z drops off near 1000°C is not as severe.

Due to the lower carrier concentration of the A92β composition, the ratio of the electronic to the phonon component of the total thermal conductivity at 1000°C is expected to be less than that of the more heavily doped material. Moreover, the rate at which the Seebeck coefficient falls off near 1000°C is also much lower than what has been observed on more heavily doped alloys; this low rate is primarily responsible for maintaining the comparatively high power factor between 800 and 1000°C.

A composition near that of the A92 material, i.e., containing 1.25 at. % P and 0.63 mole % GaP, is apparently close to the optimum for n-type $Si_{0.8}Ge_{0.2}$ alloys prepared by MA and hot pressing. However, it is likely that some of the beneficial effects of optimizing dopant concentration in a given alloy system may be offset by subsequent high-temperature diffusion bonding processes applied during device fabrication and, as mentioned, by the tendency for dopants to precipitate out of solid solution during long-term applications.

4.5. Conclusion

Nearly optimal electrical properties can be obtained in n-type $Si_{80}Ge_{20}$ alloys prepared by mechanical alloying and hot pressing having a nominal GaP content of approximately 0.6 mole percent and a Ga/P ratio of 0.25 to 0.50. The primary effect of the GaP additions appears to be an enhanced carrier concentration, as previously reported (10). Duration of the hot pressing sequence has a pronounced effect on the microstructure and hence the electrical properties. Alloys with an average grain size ≥5 to 10 microns and room-temperature values of carrier concentration $\geq 2\times10^{20}$ cm^{-3} had a mobility at or near the best values observed in zone leveled materials. Integrated average power factors of 34 to 35 $\mu W/(cm°C^2)$ between 300 and 1000°C were obtained by several combinations of composition and preparation procedure. A maximum value for the dimensionless figure of merit, of ZT = 1.1 was obtained at 1000°C. The integrated average figure of merit of an alloy having the highest power factor was determined to equal 0.94x10^{-3} °C^{-1}. Microstructure was shown to have a significant effect on carrier mobility through grain boundary potential scattering.

4.6. Acknowledgment

The Ames Laboratory is operated by Iowa State University for the United States Department of Energy under contract W-7405-ENG82. This project was supported by the DOE Radioisotope Power Systems Division. The advice and assistance of Bernard Beaudry is gratefully acknowledged.

4.7. References

1. Steele, M.C. and Rosi, F.D., J. Appl. Phys. **29**, 1517 (1958).
2. Dismukes, J.P., Ekstrom, L., Steigmeir, E. F., Kudman, I., and Beers, D.S., J. Appl. Phys. **35**, 2899 (1964).
3. McVay, G.L., Lefever, R.A., and Baughman, R.J., Mater. Res. Bull. **9**, 735 (1974).
4. Goldsmid, H.J. and Penn, A.W., Phys. Lett. **27A**, 523 (1968).
5. Parrot, J.E., J. Phys. C. : Solid St. Phys. **2**, 147 (1969).
6. Vandersande, J.W., Wood, C., and Draper, S., Mater. Res. Soc. Symp. Proc. **97**, 347 (1987).
7. Fleurial, J-P., Borshchevsky, A., Vandersande, J.W., Scoville, N., and Bajgar, C., Proc. IX Symp. on Space Nuc. Power Systems **1**, 326 (1992).
8. Cook, B.A., Harringa, J.L., Han, S.H., and Beaudry, B.J., J. Appl. Phys. **72**(4), 1423 (1992).
9. Pisharody, R.K. and Garvey, L.P., Proc. XIII IECEC **3**, 1963 (1978).
10. Fleurial, J-P., Borshchevsky, A., Proc. IX Int. Conf. on Thermoelectrics **1**, 206 (1990).
11. Vining, C.B., J. Appl. Phys. **69** 331 (1991).
12. Slack, G. and Hussain, M.A., J. Appl. Phys. **70** 2694 (1992).
13. L. J. Van der Pauw, Phillips Res Rep. **13**, 1 (1958).
14. Z. Ndlela, and C. Bates, J. Rev. Sci. Inst. **60**, 3482 (1989).

15. G. T. Meaden, Electrical Resistance of Metals (Plenum, New York, 1965), p. 143.
16. E. B. Hensley, Phys. Rev. **23**, 1122 (1952).
17. G. B. Kokos, K. A. Gschneidner, Jr., B. A. Cook, and B. J. Beaudry, J. Appl. Phys. **66**, 2356 (1989).
18. T. Amano, B. J. Beaudry, K. A. Gschneidner, Jr., R. Hartman, C. B. Vining, and C. A. Alexander, J. Appl. Phys. **62**, 819 (1987).
19. J. Murota, J. and Sawai, T., J. Appl. Phys. **53** 3702 (1982).

CHAPTER 5. ELECTRICAL PROPERTIES OF Ga AND ZnS-DOPED ZnO PREPARED BY MECHANICAL ALLOYING

A selection based on a paper published in the Journal of Applied Physics, 83 (1998) 5858.

B. A. Cook, J. L. Harringa, and C. B. Vining

5.1 Abstract

A series of n-type ZnO alloys doped with Ga and ZnS were prepared by mechanical alloying. Densities of 95 to 98 percent of theoretical density were achieved by hot pressing the milled powders at 1000°C and 1200°C, respectively. The electrical resistivity and Seebeck coefficient of alloys containing 0.25 to 3.0 atomic percent Ga were characterized between 22°C and 1000°C. The magnitude of the resistivity and Seebeck coefficient at 22°C ranged from 0.2 mΩ-cm and -25 μV/°C for the most heavily doped specimen to 1.1 mΩ-cm and -70 μV/°C for the lightly doped material. The alloys exhibit a positive temperature coefficient of resistivity and Seebeck coefficient with a nearly constant slope over the temperature range studied. Thermal diffusivity measurements on a specimen containing 1.0 atomic percent Ga were performed over the same temperature range. The thermal conductivity follows a T^{-1} dependence, decreasing from 180 mW/cm-°C at 22°C to 82 mW/cm-°C at 1000°C. An estimate of the maximum dimensionless thermoelectric figure of merit, ZT, in this system at 1000°C gives a value of 0.26, a factor of three to four less than current state-of-the-art materials such as Si-Ge. A significant reduction in thermal conductivity would be required to make these alloys competitive with existing thermoelectric power generation materials.

5.2 Introduction

The thermoelectric properties of a material can be expressed by the dimensionless figure of merit Z defined as

$$ZT = \frac{S^2 \sigma T}{\kappa} \qquad (1)$$

where S is the Seebeck coefficient, σ is the electrical conductivity, κ is the thermal conductivity, T is the temperature and the quantity $S^2\sigma$ is defined as the electrical power factor. The figure of merit of an alloy is a measure of its efficiency in converting heat to electrical energy. Doped Si-Ge alloys are the material of choice for high temperature power generation applications, particularly for interplanetary spacecraft power. While these devices have accumulated over $2.5\text{x}10^8$ device-hours without a single failure, efficiency remains relatively low at only about 6 to 8 percent. The search for materials with a higher figure of merit has been an ongoing process in recent years. Oxides have traditionally been disregarded as viable thermoelectric materials due to their large band gap and low electrical conductivity. However, a recent study by Ohtaki et al.[1] examined $(Zn_{1-x}Al_x)O$ alloys where $x = 0 - 0.1$ for high temperature thermoelectric applications and reported a dimensionless figure of merit of 0.31 in $(Zn_{0.98}Al_{0.02})O$ at 1000°C. Tanaka et. al.[2] have examined various ZnO alloys doped with other oxides for thermoelectric applications and reported a power factor (S^2/ρ) between 1.0 and 3.0 μW/cm-K^2 near 1000°C. Considerable interest has also developed in the application of ZnO thin films for optoelectronic devices such as transparent thermal mirrors and glass coatings. Wang et. al. [3] examined the electrical properties of transparent thin films based on ZnO doped with Al_2O_3, Ga_2O_3, In_2O_3, and Ge_2O_3 and found that elemental Ga can act as a dopant, thereby increasing the electrical conductivity. A more recent publication by Srikant and Clark [4] examined an anomalous variation in the band gap of ZnO films as the carrier concentration was varied between 10^{18} and 10^{20} cm^{-3}. They attribute this effect to quantum confinement of carriers in fine-grained samples by the presence of large potential barriers at the grain boundaries. The recent interest in the electro-optical properties of ZnO motivated this study of the electrical properties of ZnO doped with Ga. The possibility of isostructural alloying with ZnS provides a mechanism to decrease the lattice thermal conductivity, thereby improving thermoelectric efficiency.

5.3 Experimental Procedures

Bulk specimens of ZnO with either Ga or ZnS dopant were prepared by mechanically alloying (MA) and hot pressing. The precursor materials consisted of ZnO powder with a stated purity of 4-9's, Ga with a stated purity of 6-9's, and ZnS chunks with a stated purity of 4-9's, all from Johnson-Matthey. Compositions of the samples studied are listed in Table I. MA was carried out by milling the ZnO and additive powders in a Spex 8000 mixer/mill using hardened steel vial and 6 hardened steel balls. The material was milled for 3 hours after which the powder was transferred under high purity helium to a 1.27 cm diameter Mo foil-lined graphite die. The die assembly was then positioned in an RF hot pressing chamber. The powders were heated at a rate of 3 to 5 deg./min and were pressed at temperatures of either 1000°C or 1200°C in order to evaluate the effect of pressing temperature on the electrical properties. A pressure of 79MPa was applied for one hour in order to consolidate the powders, followed by a furnace cool to ambient. Samples were sectioned from the primary compact and ground for X-ray diffraction analysis using a powder diffractometer (Scintag, USA) and Cu radiation. The pattern for all samples was indexed and agreed with the calculated pattern for single phase hexagonal ZnO (space group $P6_3mc$). Room temperature carrier concentration and Hall mobility were measured on thin (0.1 cm) disks using the van der Pauw method [5] with four point contacts equally spaced around the perimeter. The procedure described by Ndlela and Bates [6] was used in this study. A magnetic field of 1 T was applied during which time a minimum of four voltage readings were obtained and subsequently averaged for each of the four current directions. The field was reversed and the voltage samplings repeated. The intermediate Hall coefficients were averaged and the carrier concentration was determined from the relation $n = (R_h e)^{-1}$. The accuracy of this technique is estimated at better than 1 percent. The electrical resistivity and Seebeck coefficient measurements were performed by a standard dc four-point probe technique [7] and by determination of the slope of the thermal emf versus temperature plot [8], respectively. Both properties were measured simultaneously on the same sample in a vacuum chamber (~ 10^{-7} torr) in the temperature range of 25 - 1000°C by a computer-controlled data acquisition system. A fifth-order polynomial regression was used to calculate the integrated power factors in the temperature range of 300 to 1000°C. The thermal diffusivity of a 1.27 cm diameter by 0.1 cm thick disk of one of the Ga-doped samples was measured from 300°C to 1000°C by a standard laser flash diffusivity technique. Briefly, both faces were coated with a thin (30μm) layer of graphite and the sample was mounted in a low thermal conductivity holder machined from low density ZrO_2. The sample was placed in the center of a BN tube, which was wound with Ta wire. This heater assembly was positioned inside a vacuum chamber such that a pressure of better than 10^{-7} Torr was maintained during the characterization. The front surface of the sample was irradiated by a pulse from a ruby rod laser. The zirconia sample holder minimized conductive heat losses from the material and the thermal transient was measured using an InSb detector. Corrections for finite pulse width and heat loss were applied using an in-house computer program. Thermal diffusivity values were calculated for each 5% rise in temperature between 5% and 95% of the maximum value. An average thermal diffusivity was then determined from these values. The thermal conductivity was determined from the product of the thermal diffusivity, density, and specific heat. Values for heat capacity were estimated from Kopp's rule.

5.4 Results and Discussion

Nearly fully dense bulk specimens of Ga-doped ZnO were consolidated by hot pressing. Samples hot pressed at 1000°C achieved 95 percent of theoretical density (5.68 g/cm^3) whereas those pressed at the higher temperature, 1200°C, achieved 98 percent of theoretical density. ZnO is an n-type conductor, as evidenced from the negative value of the Seebeck coefficient. Increasing the amount of Ga from 0.25 at. % to 3.0 at. % decreases the magnitude of the Seebeck coefficient, as shown in Fig. 1. The Seebeck coefficient of the doped ZnO samples monotonically increases with increasing temperature. By comparing the samples containing 0.5 at. % Ga (ZOG-6 @ 1200°C and ZOG-4 @ 1000°C) and those containing 1.0 at. % Ga (ZOG-2 @ 1000°C and ZOG-3 @ 1200°C) it is seen that the hot pressing temperature has a slight impact on the magnitude of the Seebeck coefficient. The implication from this limited data is that lower Seebeck coefficient results from higher hot pressing temperature. This is consistent with the electrical resistivity data, which are shown in Fig. 2. The samples exhibit metal-like conductivity over the temperature range studied, suggestive of phonon scattering as the limiting conduction mechanism. Characteristic of band-type semiconductors, an increase in the amount of dopant in solution decreases the magnitude of the electrical resistivity of these alloys.

Additional electrical characterization of these alloys was performed by Hall effect measurement at room temperature and the results are summarized along with compositional details in Table I.

Carrier concentration values ranged from 0.86×10^{20} cm^{-3} in the sample doped with 0.25 at. % Ga to 5.7×10^{20} cm^{-3} in the sample prepared with 3.0 at. % Ga. One sample, ZOGS-7, was prepared with 5.0 mo. % ZnS in addition to 0.5 at. % Ga and was found to have a carrier concentration of 10.80×10^{20} cm^{-3}, the highest value obtained in this study. The electron mobility values range from 38.8 to 68.5 cm^2/V-s, which are unusually high for localized electron, or hopping, conductors. Most oxides have carrier mobility in the range 0.1 to 1.0 cm^2/V-s. Such large values as obtained on the samples in this study are suggestive of conventional band-type conductivity, as supported by the electrical resistivity and thermopower data.

Results of thermal diffusivity measurements obtained on a 1.0 at. % Ga-doped ZnO sample (ZOG-2) are shown in Fig. 3. The thermal diffusivity continuously decreases over the entire temperature range suggesting that phonon scattering is the dominant mechanism. While the thermal conductivity values indicated are only an estimate, they are expected to be accurate to within about 10% by use of Kopp's rule for C_p. While the conductivity continuously decreases, it is approximately an order of magnitude too high to make this material an attractive high temperature thermoelectric material. The thermal conductivity at 300°C is estimated to equal 186 mW/cm-°C and decreases to 85 mW/cm-°C at 1000°C. These values are comparable to those reported by Ohtaki, et. al. [1] in a sample of ZnO doped with Al_2O_3 to an equivalent composition of 2.0 at. % Al. They reported a thermal conductivity of 402 mW/cm-°C at room temperature, which decreased to 54 mW/cm-°C at

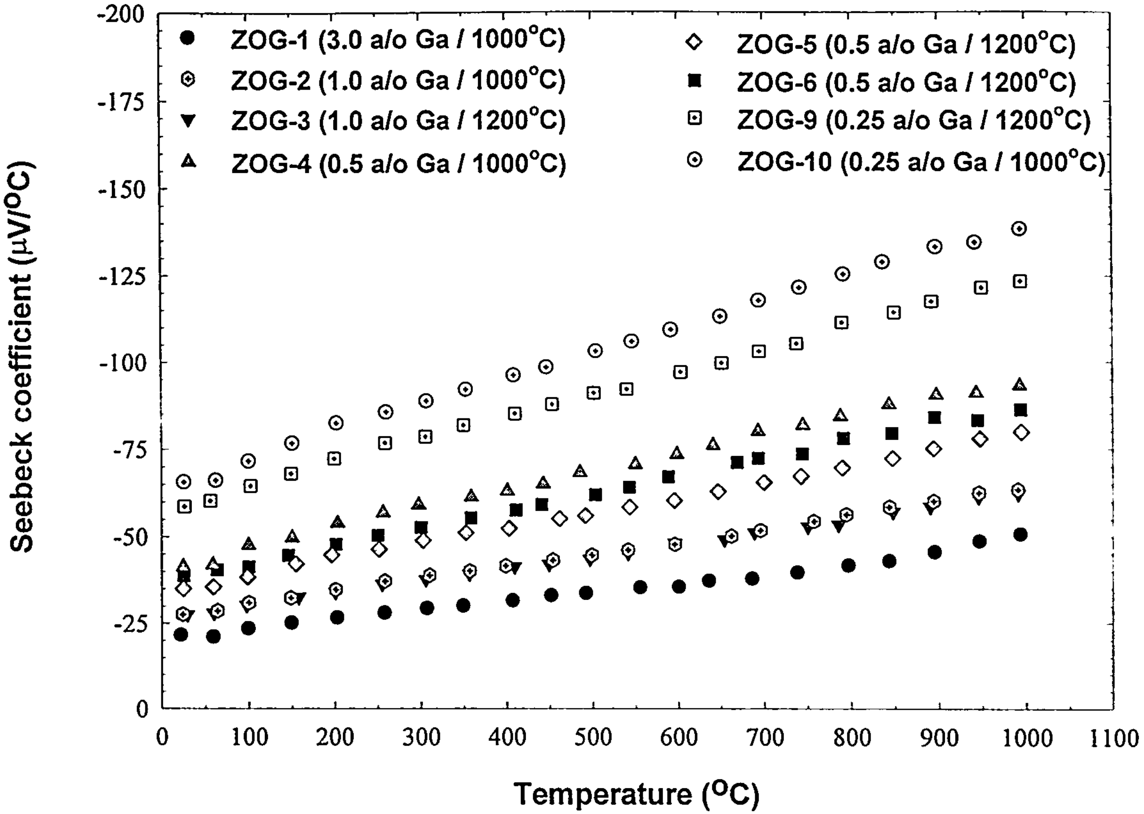

Fig. 1. Temperature Dependence of the Seebeck Coefficient of Ga-doped ZnO (Ga addition and hot pressing temperature indicated in legend).

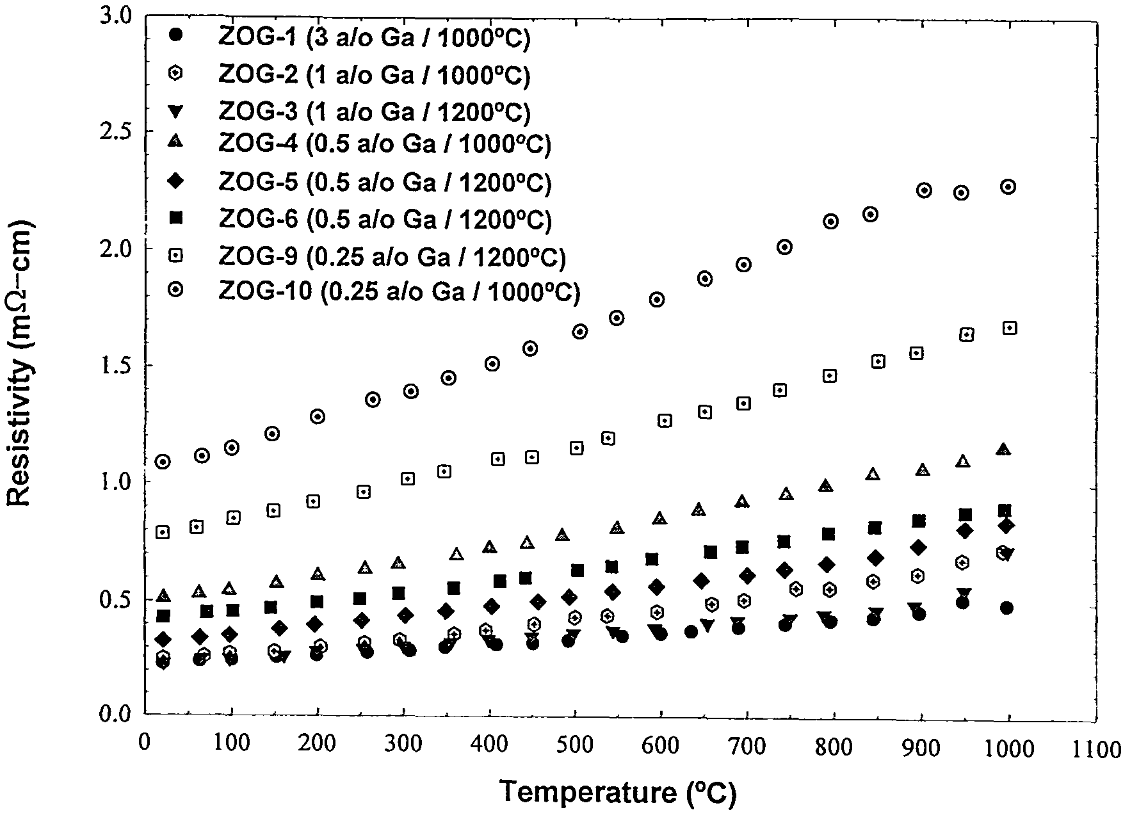

Fig. 2. Temperature Dependence of the Electrical Resistivity of Ga-doped ZnO (Ga addition and hot pressing temperature indicated in legend).

Table I. ZnO Compositions, Hot Pressing Temperatures, and Room Temperature Electrical Properties

Sample ID	Atom Percent Ga	Atom Percent ZnS	Pressing Temp. (°C)	ρ_o (mΩ-cm)	n_n (x10^{20}) (cm^{-3})	μ (cm^2/V-s)
ZOG-1	3	--	1000	0.23	5.7	46.7
ZOG-2	1	--	1000	0.25	4.2	60.5
ZOG-3	1	--	1200	0.23	4.29	62.8
ZOG-4	0.5	--	1000	0.51	1.79	68.3
ZOG-5	0.5	--	1200	0.327	2.79	68.46
ZOG-6	0.5	--	1200	0.429	2.13	68.37
ZOG-9	0.25	--	1200	0.779	1.22	65.49
ZOG-10	0.25	--	1000	1.084	0.86	67.38
ZOGS-4	0.5	5.0	1000	0.158	10.0	39.47
ZOGS-5	0.5	1.0	1200	0.388	2.30	69.34
ZOGS-6	0.5	3.0	1200	0.442	2.09	67.48
ZOGS-7	0.5	5.0	1200	0.151	10.80	38.83

1000°C. The maximum power factor of the 1.0 at. % Ga-doped ZnO was found to occur at 1000°C and had a magnitude of 10 μW/cm-°C^2 yielding an estimated ZT_{max} of 0.2.

It is possible to employ these data to estimate the maximum $S^2\sigma$ product in the Ga-doped ZnO system by constructing a Jonker plot [9] of the raw data. Assuming a simple band conductivity model, one can write

$$\sigma = ne\mu \qquad (2)$$

where σ is the electrical conductivity, n is the carrier concentration, e the electronic charge, and μ the carrier mobility. Also, if these materials can be described by simple band theory, then

$$S = \left(\frac{k}{e}\right)\left(\ln\left(\frac{N_E}{n}\right) + A\right) \qquad (3)$$

where S is the Seebeck coefficient, k is Boltzman's constant, N_E is the density of states at the Fermi level, and A is the scattering parameter which typically ranges between 0 and 2. By combining equations 2 and 3, one arrives at a simple expression for S in terms of ln(σ):

$$S = \left(\frac{k}{e}\right)\ln(\sigma) - \left(\frac{k}{e}\left(\ln\left(N_E e\mu\right) + A\right)\right) \qquad (4)$$

so that a plot of S versus ln(σ) should be linear with a slope equal to (k/e). Such a plot for the Ga-doped samples investigated in this study at a temperature of 1000°C is shown in Fig. 4. The linear regression reference line has a slope of (k/e) and, with the exception of one datum at high conductivity (i.e., the 3% Ga-doped specimen), the data fits the linear model reasonably well. This suggests that the above model is a reasonable first approximation and a prediction of $(S^2\sigma)_{max}$ can be used to extract meaningful information about the ultimate potential of these alloys as power generation materials. From the plot, a value of 12.6 is extracted for the logarithm of the intercept (i.e., $\ln(\sigma_o)$) and an $(S^2\sigma)_{max}$ of 11.9 mW/cm-°C^2 is obtained as shown in Fig. 5, corresponding to a resistivity of 2.75 mΩ-cm and a Seebeck coefficient of -180.85 μV/°C.

Of the samples investigated in this study, a maximum power factor at 1000°C occurred in the 0.25 at. % Ga-doped specimen (ZOG-10) and had a magnitude of 9.8 mW/cm-°C^2. A lower carrier concentration may serve to increase the Seebeck coefficient and hence increase the power factor, albeit the magnitude of the improvement is expected to be modest, at best. Even an optimistic ZT in this system at 1000°C would be 0.26, which is a factor of three to four less than current state-of-the-art materials such as Si-Ge.

Generally, alloying with an isostructural compound containing a heavier atomic species serves to decrease the lattice thermal conductivity by mass fluctuation scattering. This approach, while highly successful with other alloys such as Si-Ge, is only effective if a large fraction of the heat in the starting material is actually carried by phonons.

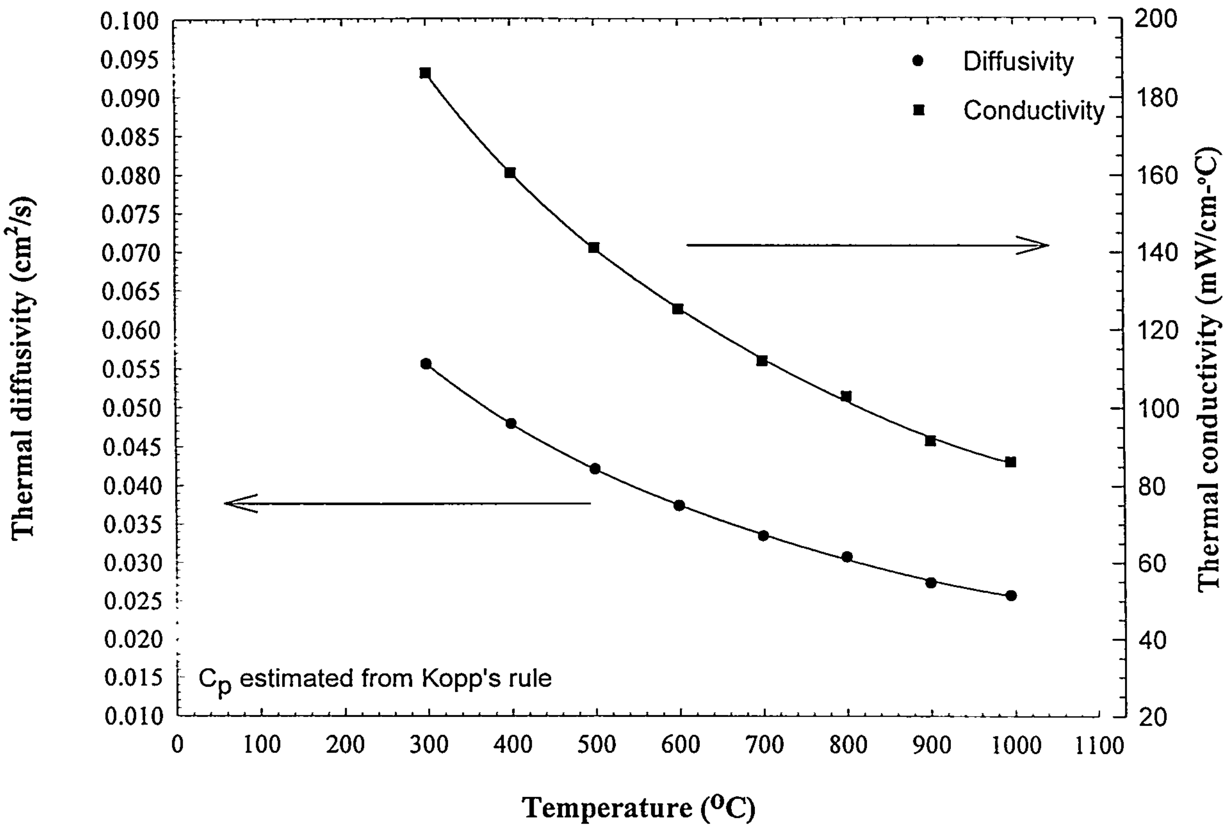

Fig. 3. Thermal diffusivity and estimated thermal conductivity of gallium-doped ZnO

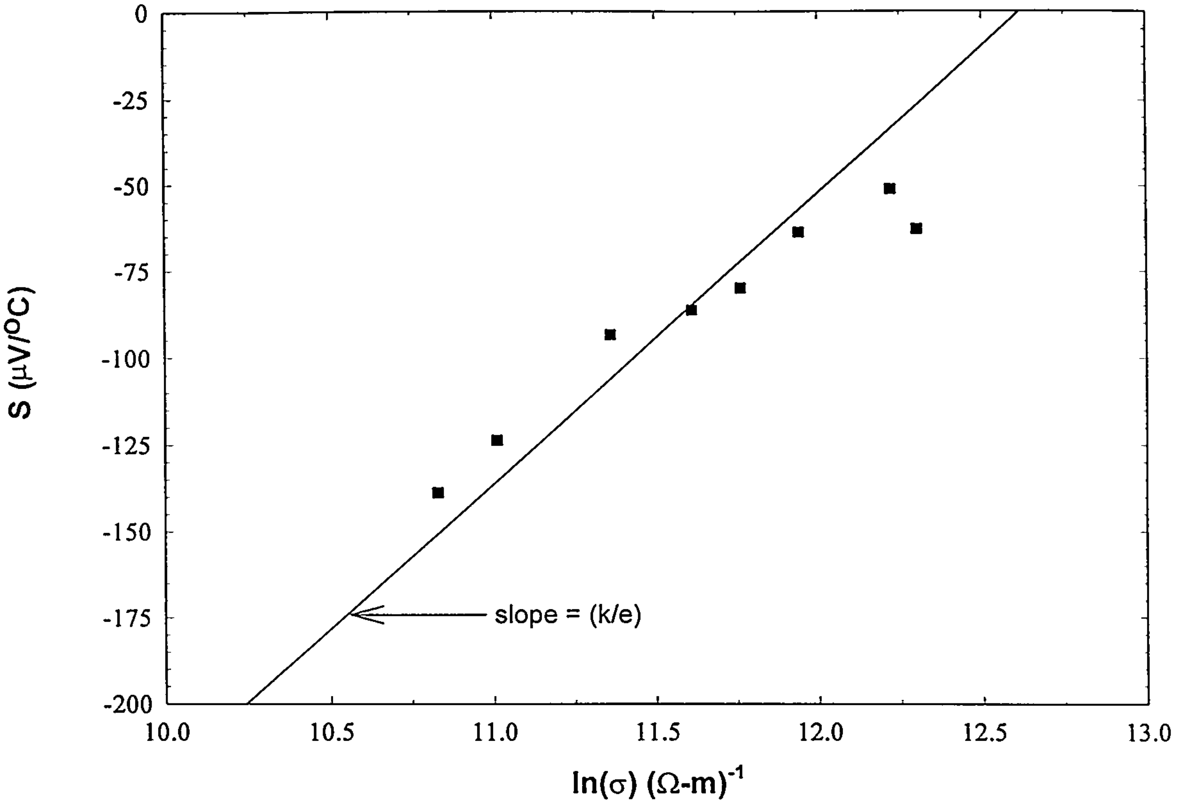

Fig. 4. Jonker Plot of Ga-doped ZnO Samples at 1000°C

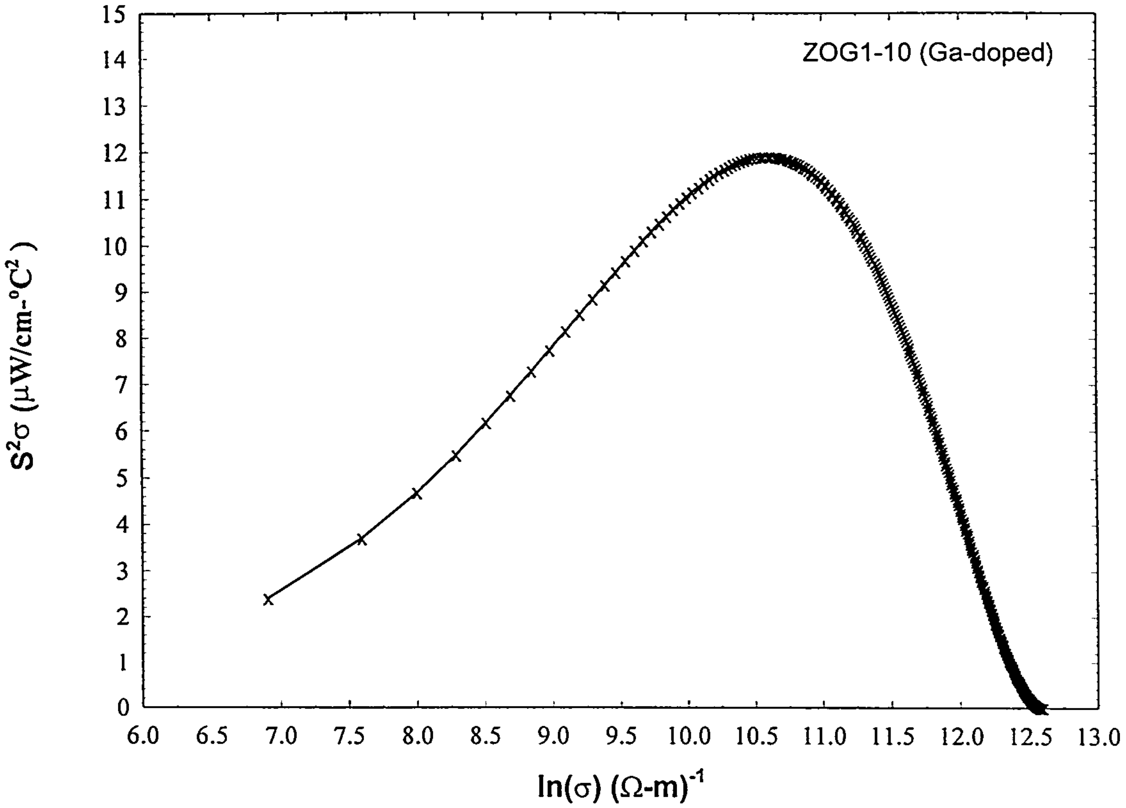

Fig. 5. Predicted ($S^2\sigma$) at 1000°C of Ga-doped ZnO

If most of the heat is transported by carriers, then the alloying method will most likely result in no net improvement in ZT. The electronic contribution at a particular temperature can be estimated from the Lorentz equation, $K_l = L_o \sigma T$, where L_o is the Lorentz number, σ the electrical conductivity, and T the absolute temperature. Assuming the classical Lorentz number of 2.44×10^{-8} W-Ω-K^{-2}, the polar contribution at 1000°C is 48.7 mW/cm-K giving a lattice contribution of 37.5 mW/cm-K. Therefore, the potential exists for some improvement by incorporating a few percent ZnS. As a test, the thermal diffusivity of one sample containing 5 mole percent ZnS, ZOGS-4, was measured within the 300°C to 1000°C temperature range. When converted to thermal conductivity, the results showed no significant decrease compared with the ZOG-2 specimen, primarily due to the increased carrier concentration (electronic contribution) in the ZOGS-4 material. After accounting for the difference in carrier concentration between these two samples (4.2×10^{20} cm^{-3} in ZOG-2 compared with 10.0×10^{20} cm^{-3} in ZOGS-4), the reduction in lattice contribution at 1000°C amounts to 36.5 percent (37.5 mW/cm-°C in ZOG-2 compared with 23.8 mW/cm-°C in ZOGS-4). Similar approaches which do not contribute to an increase in the electronic component of the thermal conductivity may prove useful. That the ZT in an *oxide* system is as large as observed in this study is itself noteworthy and suggests that related systems may be worthy of examination.

5.5 Acknowledgement

The Ames Laboratory is operated by Iowa State University for the United States Department of Energy under contract W-7405-ENG82. The ZnO samples were prepared by S. L. Purdum as part of a student research project.

5.6 References:

1. Michitaka Ohtaki, Toshiki Tsubota, Koichi Eguchi, and Hiromichi Arai, J. Appl. Phys. 79 (1996) 1816.

2. Y. Tanaka, T. Ifuku, K. Tsuchida, and A. Kato, J. Mat. Sci. Letters **16** (1997) 155.

3. R. Wang, L. H. King, and A. W. Sleight, J. Mater. Res., **11** (1996) 1659.

4. V. Srikant and D. R. Clarke, J. Mater. Res. **12** (1997) 1425.

5. L. J. Van der Pauw, Phillips Res Rep. **13** (1958) 1.

6. Z. Ndlela, and C. Bates, J. Rev. Sci. Inst. **60** (1989) 3482.

7. G. T. Meaden, *Electrical resistance of Metals* (Plenum, New York, 1965), p. 143.

8. E. B. Hensley, Phys. Rev. **23** (1952) 1122..

9. G. H. Jonker, Philips Res. Repts. **23** (1968)131.

CHAPTER 6: HIGH TEMPERATURE THERMOELECTRIC PROPERTIES OF MNiSn (M=Ti,Zr,Hf)

A selection based on papers published in the Proceedings of the XVIII International Conference on Thermoelectrics, Baltimore, MD (1999), in the Proceedings of the Fifth European Workshop on Thermoelectric Materials, Pardubice, Czech Republic (1999), and in the Journal of Material Science, 34 (1999) 323.

B. A. Cook[1], J. L. Harringa[1], G. P. Meisner[3] ,J. Yang[2,3], and C. Uher[2]

6.1 Abstract

The high temperature transport properties in a series of intermetallic half-Heusler alloys of the form MNiSn, where M = Ti, Zr, Hf, have been examined. The semiconducting nature of these materials due to the formation of a pseudo-gap in the density of states makes them promising candidates for intermediate temperature thermoelectric applications. Samples of pure TiNiSn, ZrNiSn, HfNiSn, and (Zr-Hf)NiSn were prepared by arc melting and homogenized by heat treatment. Doping effects were studied by substitution of Sb and Bi in the ZrNiSn, HfNiSn, and (Zr-Hf)NiSn compositions. Phase purity was determined by x-ray diffraction, and the microstructures were examined by scanning electron microscopy. The temperature dependence of the electrical resistivity and Seebeck coefficient of these samples was characterized between 22°C and 750°C. At room temperature, the data match closely with the results recently reported [1]. The thermopower initially increases with temperature, exhibits a broad maximum between 373K and 573K, and finally decreases to a common value, characteristic of the magnitude of the forbidden gap. The electrical resistivity decreases with temperature following a T^{-1} dependence. The large thermopowers in the doped samples were found to result from a large effective mass. An estimate of the

---

[1] Ames Laboratory, Iowa State University, Ames, IA, USA
[2] Department of Physics, University of Michigan, Ann Arbor, MI, USA
[3] Physics and Physical Chemistry Department, General Motors Research and Development Center, Warren, MI, USA

magnitude of the gap was made from a plot of ln(σ) versus reciprocal temperature, giving a value of 0.21 eV which is in good agreement with previous estimates.

6.2 Introduction

Certain classes of intermetallic compounds, based on MNiSn where M=Ti, Zr, or Hf have been shown to exhibit semiconducting behavior and relatively large Seebeck coefficients [2,3,4]. Results of band structure calculations [5] have shown that the semiconducting properties are due to the formation of a gap in the density of states at the Fermi level when one of the nickel sublattices in the MNi_2Sn Heusler structure is removed, leaving a sublattice of ordered vacancies. The resulting "half-Heusler" MgAgAs structure becomes particularly attractive for thermoelectric applications because of the potential to reduce thermal conductivity through isoelectronic alloying on the M sites, and to optimize the carrier concentration through substitution on the stannide or nickel sites. Results of initial studies on the synthesis and properties of TiNiSn [6] gave promising electrical power factors (S^2/ρ) in the 573 to 873K temperature range. Other researchers have examined substitutions for the Group IVA transition metal [7] and for the Group VIIIA transition metal [8]. Recent work by three of the authors (C. U., J. Y. and G. M.) on the Zr and Hf systems established the significance of structural disorder of the respective lattice sites on the low temperature thermal properties [9]. Since these alloys are formed by arc melting in which the casting is rapidly cooled, subsequent heat treatment is required to allow the atoms to diffuse onto their respective sublattice sites. Moreover, this study also demonstrated that a large fraction of heat is carried by phonons, opening up the possibility for reduction in thermal conductivity by alloying and other techniques. In addition, it was found that these alloys exhibited metal-like conductivity at low temperatures, changing over to semiconducting-like conductivity near ambient temperature. Such behavior is curiously reminiscent of paramagnetic to ferromagnetic transitions near the Curie point, where spin scattering of the carriers decreases upon entering the metal-like ferromagnetic state [10].

The objective of this study was to examine the elevated temperature electrical and microstructural characteristics of arc melted and annealed MNiSn, where M=Ti, Zr, and Hf.

This was accomplished in terms of the effects of isoelectronic alloying on the M sites, as well as the effects of antimony and bismuth doping on the Sn sites. Partial substitution of Hf for Zr reduces the lattice thermal conductivity by mass fluctuation disorder and leaves the electronic structure relatively intact since the electronegativity of Ti, Zr, and Hf are nearly identical. In this study, we report on the electrical resistivity and Seebeck coefficient of polycrystalline samples of TiNiSn, ZrNiSn, HfNiSn, $(Zr_{0.5}Hf_{0.5})NiSn$, $(Zr_{0.5}Hf_{0.5})NiSn_{0.995}Sb_{0.005}$, $(Zr_{0.5}Hf_{0.5})NiSn_{0.99}Sb_{0.01}$, and $(Zr_{0.5}Hf_{0.5})NiSn_{0.98}Bi_{0.02}$ as a function of temperature between 300 and 1050K.

6.3 Experimental Procedures

Stoichiometric quantities of the elemental constituents were weighed out and arc melted in an argon environment. Oxygen contamination in the specimens was minimized by first melting a Zr getter button three times before melting the components of the MNiSn. Each button was remelted at least three times to improve homogeneity. In the case of the TiNiSn samples, arc melting was accomplished by melting the Ni and Sn together, followed by addition of the Ti to form a smooth button. Samples for property measurements were sectioned from the castings using a diamond saw and had typical dimensions of 3 mm x 2 mm x 2.5 mm. Samples of the ZrNiSn, HfNiSn, and (Zr-Hf)NiSn were heat treated for 1 week at 1073K as an additional homogenization step. The TiNiSn samples were heat treated at 1113K for 3 weeks. Another set of TiNiSn samples was cut for metallography and Hall coefficient measurement from the heat treated rod, and a portion of the remainder was subjected to a final heat treatment of 1223K for a period of 2 weeks. No discoloration on the inner surface of the quartz was observed, nor was there any noticeable change in the ductility of the Ta wrapping. It was previously observed that the thermal and electrical properties were sensitive to the thermal history prior to characterization. An X-ray diffraction pattern of one of the samples ($Zr_{0.5}Hf_{0.5}NiSn$) was obtained with an automated powder diffractometer using Cu Kα radiation after grinding the sample to –200 mesh. Elemental microprobe analysis (EPMA) was performed on a piece of the $Zr_{0.5}Hf_{0.5}NiSn_{0.99}Sb_{0.01}$ sample using an ARL microprobe, equipped with six wavelength dispersive spectrometers. Additional chemical information was obtained by inductively-coupled plasma-atomic emission spectroscopy (ICP-AES) for the major components using an ARL Fisons 3410 Minitorch analyzer in which the material is solutionized in HNO_3 and HF and fed into a plasma torch. Electrical measurements were performed between room temperature and 750°C under vacuum using a standard 4-point dc technique described in a previous publication [11].

6.4 Results and Discussion

6.4.1 Microstructural and chemical analyses

Metallographic analysis showed the as-cast TiNiSn sample to be multiphase with clearly observed dendritic segregation, as seen in Fig. 1a. According to energy dispersive x-ray analysis, the dendrites correspond to Ti_6Sn_5. It is interesting to note that according to the equilibrium phase diagrams, the 6:5 phase does not exist in the Zn-Sn or Hf-Sn systems. The microstructure was significantly more homogeneous following a 3 week heat treatment at 1113K, and subsequent 2 week heat treatment at 1223K, as shown in Fig. 1b.

An x-ray diffraction pattern was obtained on ground powders from a small piece of one of the samples ($(Zr_{0.5}Hf_{0.5})NiSn$), following a 1 week heat treatment at 1073K. The results are shown in Fig. 2. The reflections are indexed to that of an fcc lattice, as expected, and Rietveld refinement of the pattern using GSAS indicated that the material is single phase with a lattice parameter of 0.6090 nm. Jeitschko [12] calculated the lattice parameter of ZrNiSn as 0.6113 nm, which is in good agreement with the results of the present study on the $(Zr_{0.5}Hf_{0.5})NiSn$ sample, considering the nearly identical covalent radii of Zr and Hf. A similar treatment of the homogenized TiNiSn samples gave a lattice parameter of 0.5930 nm, using a Nelson-Riley extrapolation routine, consistent with the smaller radius of the Ti atom. EPMA scans were performed on a sample of $Zr_{0.5}Hf_{0.5}NiSn_{0.99}Sb_{0.01}$ at two different grid sizes: 250-by-250 microns, covering essentially the entire sample, and two locations with 10-by-10 micron grids. After averaging 152 analyses, the measured elemental compositions are listed in Table I. The column "sig." is the standard deviation of the weight-% value among all good analyses (n=152); the "exp." column is the square root of counts, which is the theoretical lower limit of the standard deviation. Generally, a sample may be considered homogeneous

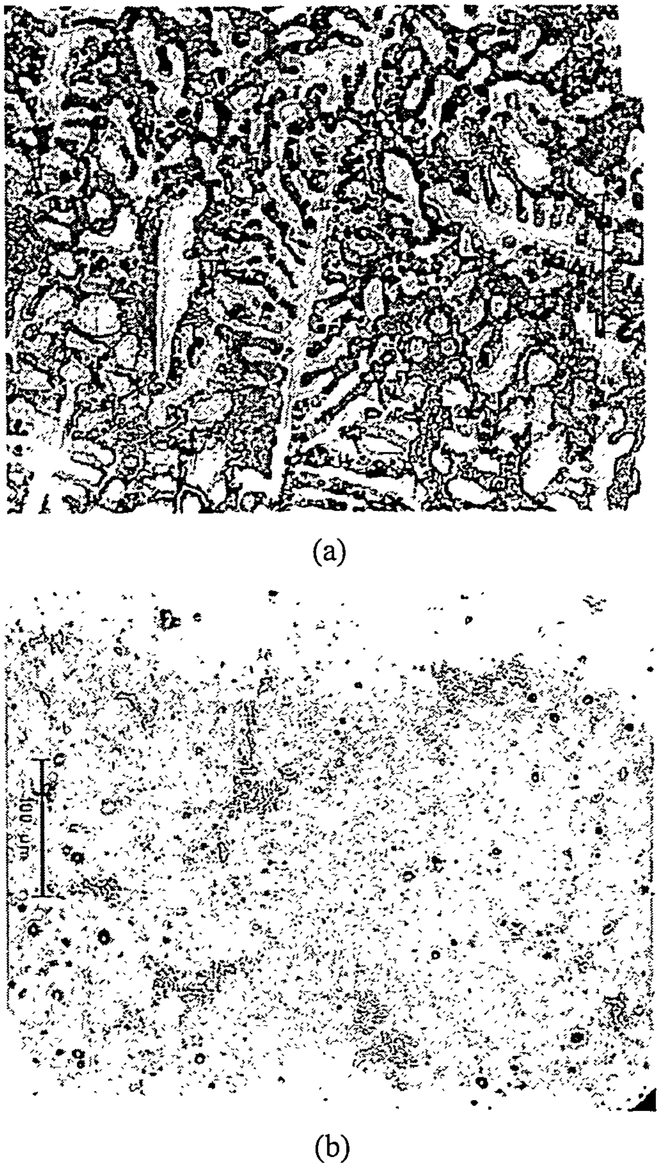

Fig. 1. Microstructures of arc melted TiNiSn.
a) as-cast b) after 3 week heat treatment at 1113K followed by additional 2 week heat treatment at 1223K
(reference scale = 100 microns)
(dendrite composition in the as-cast microstructure was determined by energy dispersive x-ray spectroscopy to be Ti_6Sn_5)

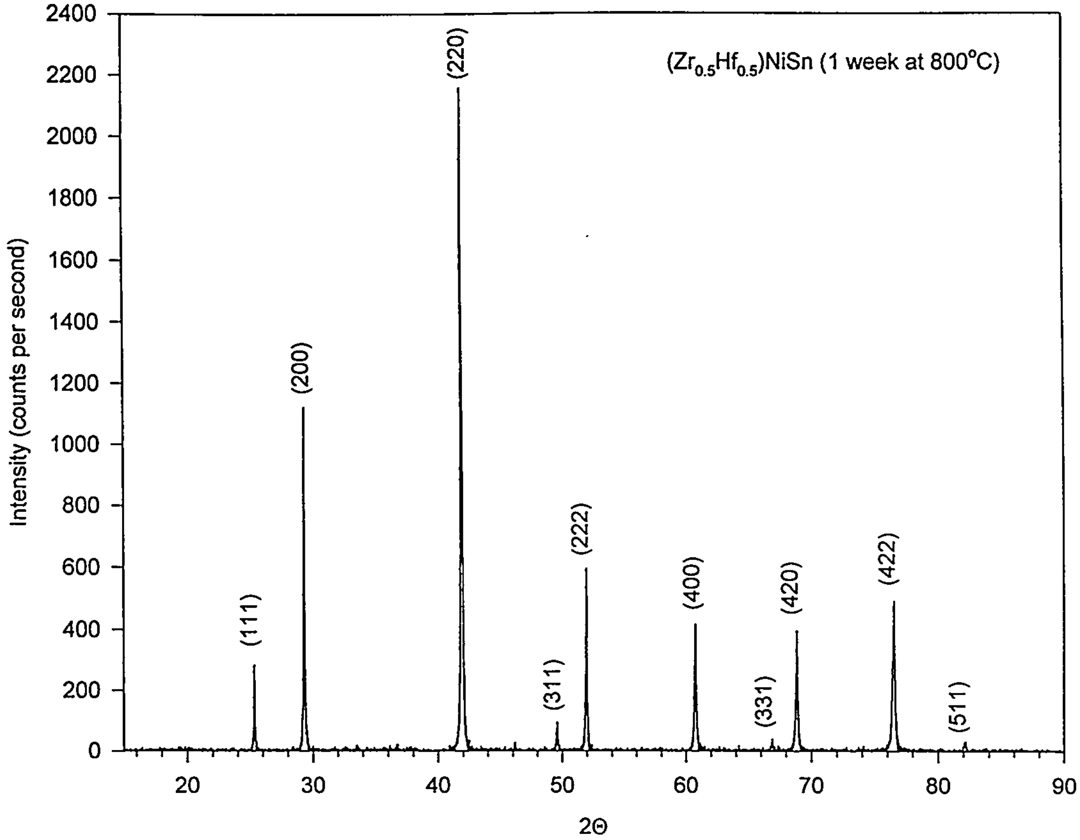

Fig. 2. X-ray Diffraction Pattern of (Zr$_{0.5}$Hf$_{0.5}$)NiSn Prepared by Arc Melting and Annealed for 1 Week at 1073K

Table I. EPMA results on a sample of $Zr_{0.5}Hf_{0.5}NiSn_{0.99}Sb_{0.01}$

Following a 1 week heat treatment at 1073K

element	weight-%	atom-%	nominal at. %	sig.	exp.
Zr	15.023	16.86	16.67	2.4%	2.2%
Hf	29.573	16.96	16.67	1.8%	1.8%
Ni	18.883	32.80	33.33	2.3%	1.2%
Sn	38.701	33.38	33.33	1.1%	0.6%

if sig.<=2*exp; these results indicate that there is no measurable heterogeneity in this material.

A second piece of the same sample was examined by ICP-AES for bulk composition. The results provide an overall indication of the relative amounts of each component, as shown in Table II. The totals do not sum to 100% due to the presence of a small amount of insoluble material.

6.4.2 Transport measurements

The temperature dependence of the electrical resistivity of the samples is shown in Fig. 3. The undoped samples exhibit semiconductor-like behavior throughout the entire temperature

Table II. ICP-AES analysis on a sample of $Zr_{0.5}Hf_{0.5}NiSn_{0.99}Sb_{0.01}$

following a 1 week heat treatment at 1073K

element	weight-%
Zr	13.3
Hf	26.6
Ni	17.0
Sn	34.6
Sb	0.40

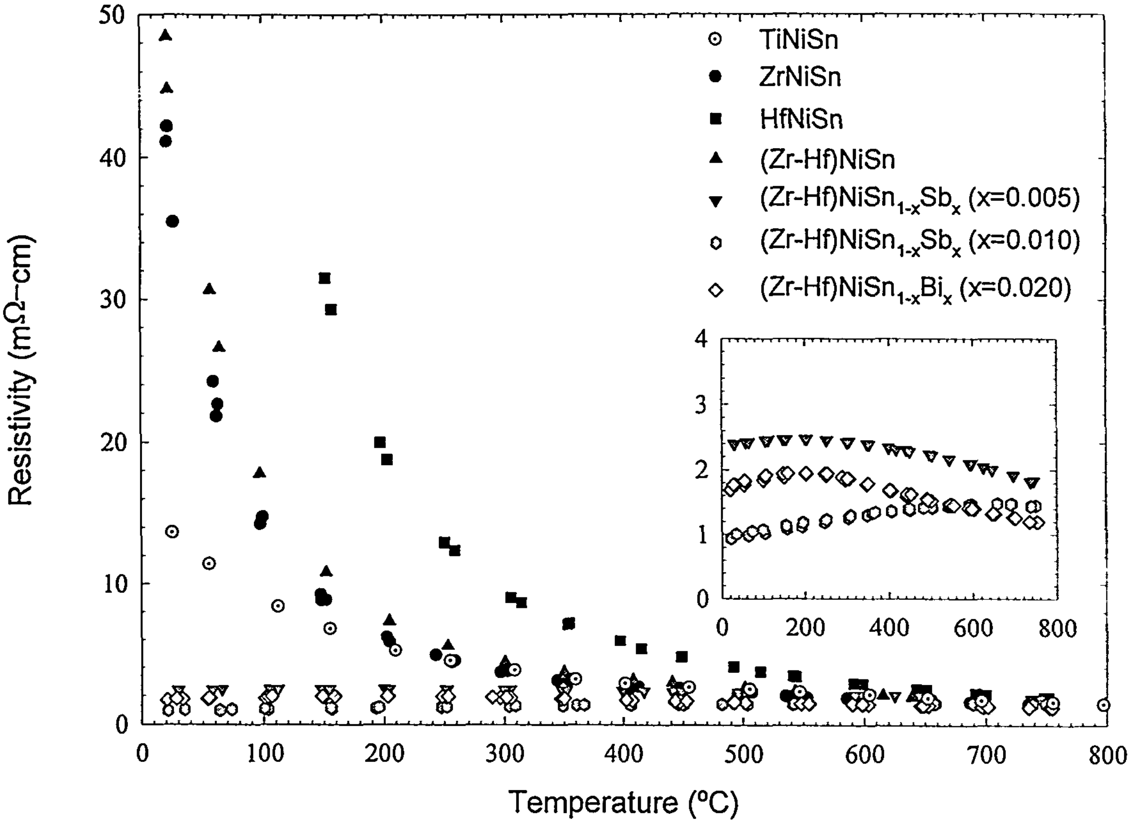

Fig. 3. Electrical Resistivity vs. temperature for MNiSn (where M = Ti, Zr, Hf). Also shown are curves corresponding to Sb doping (0.5 and 1.0 percent) and Bi doping (2.0 %) in the mixed (Zr-Hf) samples. The inset shows the three doped samples separately.

range. Near 293K, there is an appreciable difference between the magnitude of the resistivity of the ZrNiSn and the HfNiSn samples; the latter having a resistivity on the order of a factor of three higher, consistent with previous observations of the low temperature properties of these alloys. The resistivity of the isoelectronic alloy, $(Zr_{0.5}Hf_{0.5})NiSn$ is comparable to that of the ZrNiSn.

The objective of doping is generally to shift the Fermi level to a more favorable position. We have examined the behavior of the (Zr-Hf)NiSn system for different amounts of Sb substitution; 0.5% and 1.0 %, and Bi substitution; 1.0% and 2.0%. The effect of Sb-substitution on the Sn sites is significant, as shown in Fig. 3. The doped samples exhibit a metallic or semimetallic behavior, and the room temperature resistivity has decreased by one to two orders of magnitude. It is observed that as the temperature is increased, the resistivity of all samples approaches a common value. In a typical doped semiconductor, as the doping increases, the Fermi level shifts toward the conduction band (in the case of n-type materials). With an increase in temperature, however, the Fermi level approaches the intrinsic value, and at sufficiently high temperature the effects of doping are masked by intrinsic conduction.

One can estimate the band gap energy in the undoped semiconducting samples by assuming an Arrhenius relationship of the form

$$\sigma = \sigma_o \exp\left\{-\frac{E_g}{2kT}\right\} \qquad (1)$$

where E_g is the band gap energy, k is Boltzman's constant, and T is the absolute temperature. Plots of $\ln(\sigma)$ versus T^{-1} are shown in Fig. 4 for the ZrNiSn, HfNiSn, and $(Zr_{0.5}Hf_{0.5})NiSn$ samples. The experimental values for each sample are well fit to an exponential relationship, suggesting that the Arrhenius model is a good description for the conductivity of these materials in the high temperature regime. The fitting parameters give the following values for E_g: 0.21 eV for ZrNiSn, 0.24 eV for $(Zr_{0.5}Hf_{0.5})NiSn$, and 0.33 eV for HfNiSn. These values are roughly consistent with the increase in melting temperature of the group IVB element; Ti (1668°C), Zr (1855°C), and Hf (2233°C). The calculated values by Õgüt and

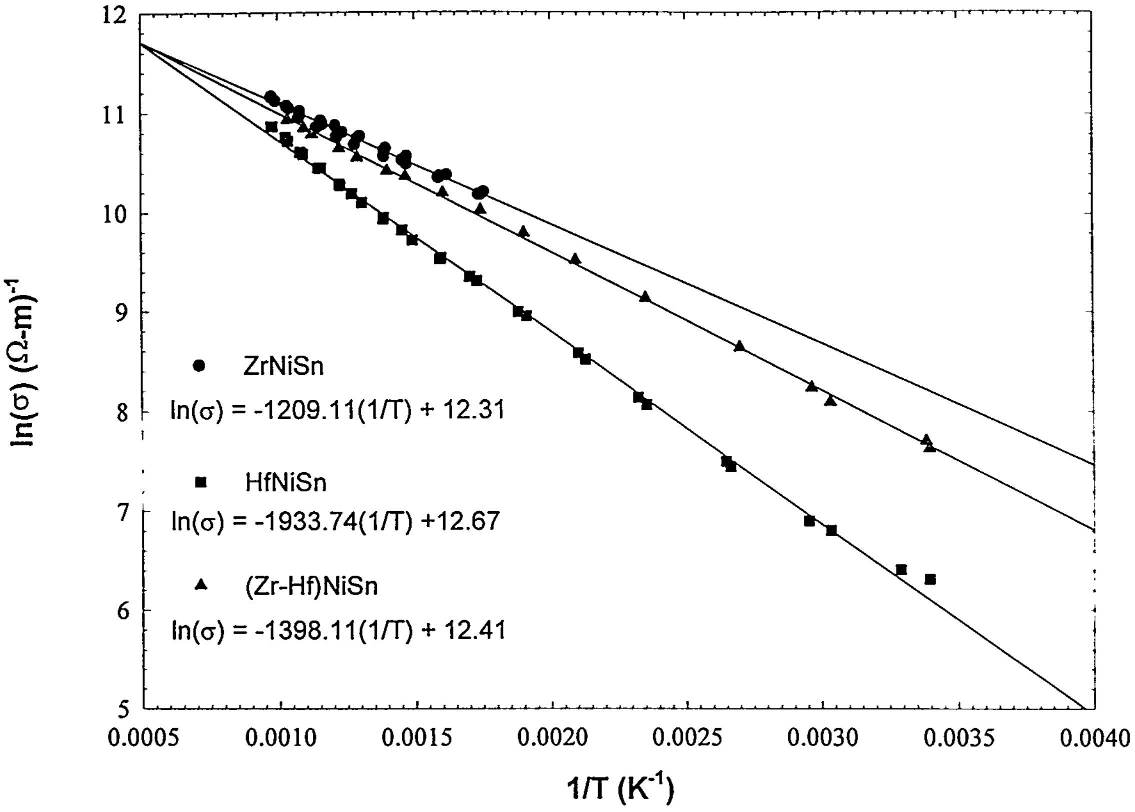

Fig. 4. Arrhenius plot of ln(σ) vs. reciprocal temperature for ZrNiSn, HfNiSn, and $(Zr_{0.5}Hf_{0.5})NiSn$ showing the estimated magnitudes of the gap in the density of states at the Fermi level.

Rabe [5] for the indirect band gap in ZrNiSn and HfNiSn are 0.51 eV and 0.48 eV, respectively. However, in that study they cite the results of previous work by Aliev, et al. [4] who estimated the magnitude of E_g as 0.19 eV for ZrNiSn and 0.22 eV for HfNiSn, based on electrical measurements. The discrepancy may be due, in part, to the degree of disorder or intermixing between the group IVA and Sn sites. The electrical properties of these alloys appear to be strongly dependent on the prior thermal history. According to the calculations of Ö & R, a 15 percent intermixing between Zr and Sn is sufficient to close the gap and form a semimetal. Consequently, if these calculations are correct, one would expect a lower apparent band gap for samples displaying significant intermixing between the Zr and Sn and between the Hf and Sn sites, as would be the case in the high temperature limit.

The Seebeck coefficient for these samples is shown in Fig. 5. The temperature-independent, metal-like behavior observed in the low temperature (< 150K) limit is replaced by a semiconductor-like behavior with relatively large magnitude and broad maxima. Doping with Sb shifts the maximum to higher temperatures. It is quite significant that while doping reduces the electrical resistivity by over an order of magnitude, the Seebeck coefficient of the doped samples is reduced by 15 to 25 percent at temperatures below 623K. For this reason, the $S^2\sigma$ product (referred to as the power factor) is considerably higher for the doped samples than for the undoped samples. In fact, the $(Zr_{0.5}Hf_{0.5})NiSn$ sample doped with 1 % Sb exhibits a peak power factor in excess of 35 $\mu W/cm\text{-}K^2$ over a broad region between 673K and 873K. The impressive electrical response is comparable to the best current-generation high temperature thermoelectric materials (Si-Ge solid solutions).

Additional samples of $Zr_{0.5}Hf_{0.5}NiSn$ containing small amounts of Bi were synthesized in order to compare the doping behavior with Sb. The electrical resistivity and Seebeck coefficient of one of these samples, prepared with 2.0 % Bi, is shown for comparison in Figs. 3 and 5, respectively. The bismuth reduces the resistivity to an intermediate value between that of the 0.5 and the 1.0 % Sb-doped samples up to about 873K and results in the lowest resistivity at temperatures greater than this. However, the Seebeck coefficient of the 2% Bi-doped sample is significantly lower than either of the Sb-doped specimens, resulting in a reduced power factor. Consequently, it does not appear that Bi is as effective a dopant in this

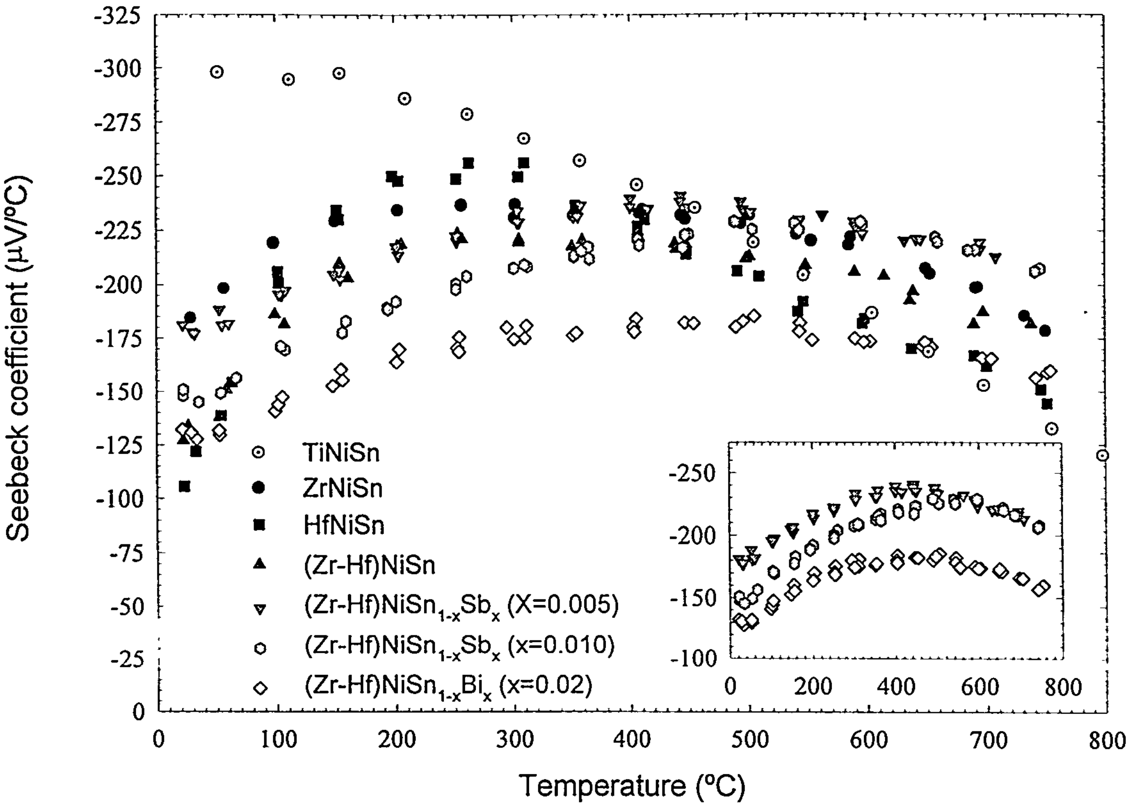

Fig. 5. Seebeck coefficient vs. temperature for MNiSn (where M = Ti, Zr, Hf). Also shown are curves corresponding to Sb doping (0.5 and 1.0 percent) and Bi doping (2.0 %) in the mixed (Zr-Hf) samples. The inset shows the three doped samples separately.

system as Sb. The relatively large thermopowers are believed to be a consequence of the large effective mass of the carriers in this system. One can estimate the effective mass by combining the results of Seebeck coefficient and Hall effect measurements, assuming a single band conduction model. When the distribution of carriers is described by Fermi-Dirac statistics, as in the case of partial degeneracy, one can write the carrier concentration, n, in terms of the effective mass, m^*, as

$$n = \frac{4}{\sqrt{\pi}}\left(\frac{2\pi m^* kT}{h^2}\right)^{3/2} F_{\frac{1}{2}}(\mu) \qquad (2)$$

where k is Boltzmann's constant, h is Planck's constant, T is the absolute temperature, μ is the reduced Fermi energy (in units of kT), and $F_{1/2}(\mu)$ is the Fermi integral, which has the form

$$F_{\xi}(\mu) = \int \frac{\xi^{x}}{(1+\exp(\xi-\mu)} d\xi \qquad (3)$$

The Seebeck coefficient, S, can be written as [13]

$$S = -\frac{k}{e}\left[\frac{(2+s)F_{1+s}(\mu)}{(1+s)F_{s}(\mu)} - \mu\right] \qquad (4)$$

where s represents the scattering parameter, which is taken as 0 for acoustic mode lattice scattering, 2 for ionized impurity scattering, and 1 for mixed scattering. The simplest approximation is to assume lattice (phonon) scattering. The carrier concentration and Seebeck coefficient at 293K for a number of samples studied are shown in Table III. The large effective masses account for the high Seebeck coefficient values observed in these materials. Doping with Sb and Bi changes the band structure to a more favorable curvature for high thermopower.

Table III. Transport coefficients of MNiSn samples at 293K

Sample	n (x10^{26} m^{-3})	S (μV/K)	m^*
ZrNiSn	0.2	-210	1.2
$(Zr_{0.5}Hf_{0.5})NiSn$	0.2	-203	1.2
$(Zr_{0.5}Hf_{0.5})NiSn_{0.995}Sb_{0.005}$	1.3	-149	2.2
$(Zr_{0.5}Hf_{0.5})NiSn_{0.99}Sb_{0.01}$	2.1	-196	4.7
$(Zr_{0.5}Hf_{0.5})NiSn_{0.99}Bi_{0.01}$	0.6	-242	3.1
$(Zr_{0.5}Hf_{0.5})NiSn_{0.98}Bi_{0.02}$	5.1	-139	5.0

The thermal conductivity of these alloys has been previously characterized from 4.2K to 293K [9]. It was found that the thermal conductivity is a function of both the doping and of the prior thermal history. While the peak in thermal conductivity corresponding to the low temperature T^3 to high temperature T^{-1} crossover diminishes significantly with prolonged annealing, the difference in room temperature values tends to be less pronounced. For example, the room temperature thermal conductivity of $(Zr_{0.5}Hf_{0.5})NiSn$ varies from 46 mW/cm-K with no heat treatment, to 53 mW/cm-K following a 1 week heat treatment at 1073K. The addition of 0.5% Sb increases the room temperature value to 60 mW/cm-K while the addition of 1.0% Sb increases this value still further to 66 mW/cm-K. Isostructural substitution on the M sites was found to have a significant effect on thermal conductivity. The thermal conductivity at 293K of ZrNiSn was reduced by a factor of 3, from 17.2 W/m-K to 5.3 W/m-K, by substitution of Hf in $(Zr_{0.5}Hf_{0.5})NiSn$. When thermal conductivity of the 1.0 % Sb-doped sample at 293K is incorporated into a high temperature T^{-1} model, a magnitude of 5.8 W/m-K is obtained at 773K. This yields a ZT of 0.5 when combined with the measured S^2/ρ value, which is the highest ZT yet suggested in the MNiSn system. If additional substitution on the Ni sites to further reduce the lattice thermal conductivity can be successfully combined with optimization of doping on the Sn sites, this material would have a ZT close to unity. Clearly, additional work is warranted to determine the extent to which further substitution can achieve this goal.

6.5 Conclusion

Intermetallic compounds having a gap in the density of states at the Fermi level are attractive candidates for low and intermediate temperature thermoelectric applications. Preliminary transport measurements on annealed MNiSn, where M=Ti, Zr, or Hf indicate that electrical power factors exceeding 35 μW/cm-K^2 within the 673K to 873K temperature range are achievable. Control of microstructure is a critical processing variable in the optimization of these alloys. Additional work is needed in order to understand the extent to which isostructural alloying on the Ni sites can result in further lowering of the thermal conductivity.

6.6 Acknowledgment

The Ames Laboratory is operated by Iowa State University for the United States Department of Energy under contract W-7405-ENG-82. The microprobe analysis of Dr. Alfred Kracher is gratefully acknowledged. This project was funded by DARPA.

6.7 References

1 C. Uher, J. Yang, S. Hu, D. T. Morelli, and G. P. Meisner, "Transport Properties of Pure and Doped MniSn (M=Zr, Hf)," Phys. Rev. B 59 (1999) 8615.

2 Z. M. Dashevsky, L.L. Dudkin, V.B. Eliseev, and R.V. Skolozdra, "New Materials for Thermoelectric Generation", X Int. Conf. on Thermoelectrics, D.M. Rowe, ed. (Babrow Press, Cardiff, UK, 1991) 186-190.

3 F.G. Aliev, *Physica B* **171** (1991) 199-205.

4 F.G. Aliev, N.B. Brandt, V.V. Moshchalkov, V.V. Kozyrkov, R.V. Skolozdra, and A.I. Belogorokhov, *Z. Phys. B - Condensed Matter* 75 (1989) 167-171.

5 S. Ögut and K. M. Rabe, *Phys. Rev. B* **51**, 16 (1995) 10443-10453.

6 B. A. Cook, J. L. Harringa, Z. S. Tan, and W. A. Jesser, Proc. XV Intl. Conf. On Thermoelectrics, Pasadena, CA, March 1996, IEEE Catalog Number $96^{TH}8169$, p. 122.

7 F.G. Aliev, V.V. Kozyrkov, V.V. Moshchalkov, R.V. Scolozdra, and K. Durczewski, *Z. Phys. B - Condensed Matter* **80** (1990) 353-357.

8 A.H. El-Sayed, G.J. Nieuwenhuys, J.A. Mydosh, and K.H.J. Buschow, *J. Phys. F: Met. Phys.* **18** (1988) 2265-2281.

9 C. Uher, J. Yang, S. Hu, D. T. Morelli, and G. P. Meisner, Phys. Rev. B 59 (1999) 8615.

10 G. Ji, X. J. Fan, J. H. Zhang, C. S. Xiong, and X-G Li, J. Phys. D: Applied Phys. 31 (1998) 3036.

11 B.A. Cook, J.L. Harringa, S.H. Han, and C.B. Vining *J. Appl. Phys*. **78** (1995) 5474-5480.

12 W. Jeitschko, Metall. Trans. 1 (1970) 3159.

13 A. H. Wilson, "The Theory of Metals," 2nd Ed. (University Press, Cambridge), 232 (1953).

CHAPTER 7: THERMOELECTRIC PROPERTIES OF HOT PRESSED $(Nd_{0.5}Gd_{0.5})Se_{1.50-X}$ WHERE X = 0.01, 0.02

A paper submitted to Journal of Applied Physics

B. A. Cook and J. L. Harringa
Ames Laboratory, Iowa State University
Ames, IA 50011-3020

7.1 Abstract

Rare earth selenides based on the composition $(Nd_{0.5}Gd_{0.5})Se_{1.50-x}$ where $0.005 \leq x \leq 0.030$ were prepared by vapor phase reaction, melting, and hot pressing. The transport properties of electrical resistivity, Seebeck coefficient, and thermal diffusivity were characterized between 300K and 1300K. In addition, the carrier concentration and mobility were characterized at 300K. Chemical composition and homogeneity were determined on several samples by electron microprobe and atomic emission spectroscopy. Partial substitution of Nd for Gd was found to stabilize the high temperature gamma (Th_3P_4-type) phase. This system is characterized by a low thermal conductivity, the temperature dependence of which indicates mixed scattering. Analysis of the Seebeck and carrier concentration data by a single band conduction model suggests the existence of a heavy electron band, responsible for the large thermopower in this system. Estimation of the maximum achievable electrical properties in this system was accomplished by construction of a Jonker plot. The results predict a maximum power factor (S^2/ρ) of 5.4 μW/cm-°C^2 corresponding to a resistivity of 5.5 mOhm-cm and a Seebeck coefficient of –172.3 μV/°C.

7.2 Introduction

Predictions of continual increases in the dimensionless figure of merit, ZT, of thermoelectric materials, made during the 1950's and 1960's [1], have largely given way to only modest, incremental progress. Recent studies [2,3,4] have provided experimental evidence that ZT=1 does not represent a fundamental physical limitation on electrical and thermal transport in bulk condensed matter, however, relatively few materials have been shown to fall into this category. One such material, substoichiometric gadolinium sesquiselenide, has been shown to have a ZT greater than unity at elevated temperatures. However, the existence of a sluggish second order phase transformation from the high temperature body centered cubic (Th_3P_4-type, or gamma) phase to the low temperature orthorhombic (U_2S_3-type, or eta) phase at 900°C precludes its use in practical thermoelectric generators. This transformation is highly undesirable since the lower symmetry orthorhombic polymorph has a much lower ZT than the cubic, and the accompanying volume change produces microcracks in the material [5]. There is also evidence of the existence of a beta, or oxyselenide phase, having a stoichiometry of $R_{10}Se_{14}O_1$, in systems for which R = La, Ce, or Pr [6]. Since neodymium is thought to be stable against formation of the beta and eta phases, partial substitution for gadolinium could serve to stabilize the gamma phase and make this material useful for device considerations. Verification of the hypothesis that addition of neodymium to gadolinium selenide could stabilize the cubic phase was a key goal of this work. A second objective was to identify compositions yielding the largest ZT in this system.

A number of phases exist in the rare earth (R) – chalcogen (X) system, for example RX, R_3X_4, R_2X_3, and RX_2. Compositions near the R_2X_3 are narrow gap semiconductors and, consequently, of most interest for thermoelectric applications. The cubic (γ) phase of $GdSe_x$ exists in a bcc Th_3P_4 "defect structure," in which the metal atoms are randomly distributed among 12 lattice sites. At the 2:3 composition, each unit cell contains 10-2/3 metal atoms in a disordered structure. The disorder on the metal sites results in a high phonon scattering rate and concomitant low lattice thermal conductivity. At this composition, written as R_2Se_3, the two R^{+3} atoms contribute 6 electrons which are accommodated by the three Se^{-2} atoms, resulting in no free carriers per formula unit. Consequently, the 2:3 composition is an electrical insulator. Addition of metal atoms to the 1-1/3 unoccupied sites per unit cell increases the carrier concentration, resulting in a transition to metallic conductivity. At the R_3Se_4 composition, the three R^{+3} atoms contribute a total of 9 electrons while the four Se^{-2} atoms can accommodate only 8. Thus, there is a net contribution of one conduction electron per formula unit. This "self-doping" characteristic of the rare earth chalcogenides has attracted the interest of other researchers investigating high ZT materials [7,8,9]. One of the first comprehensive studies on the preparation and properties of rare earth chalcogenides was performed by Cutler et al [10]. Their study examined the $Ce_{3-x}S_4$ system and established that this system behaves as a degenerate, n-type semiconductor with metallic-like conductivity. The R_2X_3 compounds are sensitive to oxygen as discussed by Guittard, Benacerraf, and Flahaut [11]. In their study it was reported that $GdSe_x$ reacts readily with oxygen or moisture to form an oxyselenide phase, consequently it is incumbent that handling of this material be carried out in a low oxygen environment. A related study by Ryan et al [12] on the CeS_y system associated a degradation in the electrical properties of this material specifically to oxygen contamination.

Experimental evidence obtained during this study has shown that a ZT greater than unity can be obtained within a range of compositions between the 1.470 and the 1.490. Samples with a composition within this range have been synthesized and characterized for chemical composition by ICP and EPMA. Transport properties (electrical resistivity, Seebeck coefficient, thermal diffusivity, and electron mobility) have been characterized for each composition.

7.3 Experimental Procedures

Preparation of $(Nd_{50}Gd_{50})Se_x$ samples was accomplished by a vapor phase reaction between electropolished $Nd_{50}Gd_{50}$ strips and Se shot in sealed quartz ampoules, followed by melting in W crucibles at 1750°C and subsequent grinding and hot pressing of the castings. The rare earth samples were prepared by arc melting high purity Nd and Gd (Ames Laboratory Material Processing Center) together to form buttons of $Nd_{0.5}Gd_{0.5}$. The buttons were remelted six times to ensure homogeneity and then cast into fingers. Weight losses during arc melting were negligible, consistently below 0.3 percent. The fingers were sectioned into 1 mm disks by a low speed diamond saw and each slice was rinsed in acetone and air dried. The slices were then rolled to strip geometry with a thickness of 0.61 mm. Each strip was electropolished, which forms a passivating chloride surface layer. The strips were then weighed in a high purity glove box along with the appropriate amount of selenium shot (Alfa-Aesar) and sealed in quartz ampoules under a slight negative pressure of helium, relative to ambient. Typical mass was 12 to 13 grams of powder per ampoule. In addition, approximately 1 weight percent of iodine was added as a catalyst for each alloy. As discussed by Gschneidner [13], with the exception of lanthanum and cerium, reaction between a chalcogen gas and rare earth metal results in formation of a tenacious coating which inhibits the desired reaction. Iodine vapor is thought to promote reaction between the rare earth strips and selenium shot by a two-step process as shown below.

i. $3I + R \rightarrow RI_3$

ii. $2RI_3 + 3Se \rightarrow R_2Se_3 + 6I$

The sealed sample ampoules were placed in a cool furnace, heated to 225°C overnight, and then held at 625°C for 3 days. Since the reaction between rare earth metal and selenium is highly exothermic, slow heating of the ampoules is essential to avoid overpressures which can rupture the tube. Evidence of unreacted Se was obtained by partially withdrawing the tube from the furnace; any unreacted Se would be observed as a condensate on the cold surface of the tube end. Usually, all of the Se had reacted after the 625°C step. The tubes were then heated to 850°C for 2 days, and to 1000°C for an additional 2 days. Discoloration of the ampoule was observed in numerous cases, indicating either that the reaction had not gone to completion or that the seal was imperfect, allowing oxygen to enter. The ampoules were opened in a low oxygen glove box to minimize exposure to air. The powder at this point in the processing corresponded to $RSe_{1.50}$ + unreacted metal; melting is required to obtain the desired stoichiometry. To this end, the contents of the tubes were transferred to W crucibles, which were loaded into an RF induction system equipped with inert gas pressurization capability. The samples were melted under positive pressure of Ar at 1750°C. The melting sequence produces a single phase $(Nd\text{-}Gd)Se_{1.50\text{-}x}$ casting. While the casting has the correct composition, an additional hot pressing step is required to produce a fine-grained material with sufficient mechanical strength for handling without fracture. The hot pressing is performed in a graphite die under vacuum of 10^{-7} Torr at temperatures ranging from 1100°C to 1500°C with an applied load of 70 MPa.

Numerous complications led to poor reproducibility in the early phases of this research. Samples prepared with non-electropolished $Nd_{50}Gd_{50}$ strips produced material with anomalously high resistivity, resulting in low power factors. Samples prepared with electropolished metal precursor strips exhibited considerably lower resistivity and good power factors.

A few samples prepared under identical conditions with $x = 1.47$ exhibited unexpected high resistivity and a reaction product that appeared distinctly different from the good quality $x = 1.48$ and 1.49 counterparts. The quartz tubes were found to turn greenish-yellow or appear frosted. Following melting, the powder produced from grinding many of the 1.47 cast ingots appeared orange, indicating the presence of polysenenides. A significant increase in the vapor phase reaction time gave improved results with finer powder and cleaner ampoules at the completion of the reaction.

Determination of the effects of hot pressing temperature on the properties of this system was accomplished by first vapor-reacting and melting a 250 gram "master" alloy of 1.48 composition, from which smaller portions were taken, ground, and hot pressed as described above. Concerns over possible oxygen pick up in this master alloy motivated preparation of a number of additional samples with varying Se/R ratios in smaller 10 to 12 gram quantities for study of the effect of composition on transport properties.

Samples for Seebeck coefficient, electrical resistivity, Hall effect, thermal conductivity, metallographic, and chemical analysis were cut from each hot pressed compact.

The room temperature carrier concentrations and Hall mobilities were measured on thin (0.1 cm) disks using the van der Pauw method [14] with four point contacts equally spaced around the perimeter. The procedure described by Ndlela and Bates [15] was used in this study. A magnetic field of 1 T was applied during which time a minimum of four voltage readings were obtained and subsequently averaged for each of the four current directions. The field was reversed and the voltage samplings repeated. The intermediate Hall coefficients were averaged, and the carrier concentration was determined from the relation $n = (R_H e)^{-1}$. The accuracy of this technique is estimated at better than 1 percent of the true value. The electrical resistivity and Seebeck coefficient measurements were performed by a standard dc four-point probe technique [16] and by determination of the slope of the thermal emf versus temperature plot [17], respectively. Both properties were measured simultaneously on the same sample in a vacuum chamber (~ 10^{-7} Torr) in the temperature range of 25 - 1000°C by a computer-controlled data acquisition system. A fifth-order polynomial regression was used to calculate the integrated power factors in the temperature range of 300 to 1000°C. Thermal diffusivity was measured from 300°C to 1000°C by a standard laser flash diffusivity technique described in a previous publication [18]. Briefly, both faces were coated with a thin (20µm) layer of graphite and the sample was mounted in a low thermal conductivity holder machined from low density ZrO_2. The sample was placed in the center of a BN tube which was wound with Ta wire. This heater assembly was positioned inside a vacuum chamber such that a pressure of less than 10^{-7} Torr was maintained during the characterization. The front surface of the sample was irradiated with a pulse from a ruby rod laser. The zirconia sample holder minimized conductive heat losses from the material, and the thermal transient was measured using an InSb detector. Corrections for finite pulse width and heat loss were applied using an in-house computer program. Thermal diffusivity values were calculated for each 5% rise in temperature between 5% and 95% of the maximum value. An average thermal diffusivity was then determined from these values. Accuracy of the equipment was determined by characterizing a piece of N.I.S.T. graphite, which gave results agreeing to within 2 percent of the published values. The thermal conductivity was determined from the product of the thermal diffusivity, density, and specific heat. Heat capacity data were obtained using a Perkin-Elmer DSC-7.

X-ray diffraction patterns were obtained with an automated powder diffractometer (Scintag Pad V) using Cu Kα radiation. Samples were ground in an agate mortar and mixed with vacuum grease on a glass slide. Step scans were performed with a step size of 0.03° and a dwell time of 3 seconds.

Additional chemical information was obtained by inductively-coupled plasma-atomic emission spectroscopy (ICP-AES) for the major components using an ARL Fisons 3410 Minitorch analyzer, in which the material is solutionized in HNO_3 and HF and fed into a plasma torch. Determination of minor chemical impurities was obtained by laser ionization mass spectroscopy (LIMS).

7.4 Results and Discussion

7.4.1 Microstructure and chemical analysis

Typical microstructure of (Nd-Gd)Se_y samples is shown in Fig. 1a. Grain size of good-quality low oxygen samples generally ranges between 10 and 40 microns, although a few grains as large as 80 microns were observed. A few samples of high Se/R ratios prepared with non-electropolished metal tended to precipitate red crystals out of solution, both intergrannularly and intragrannularly. The presence of these crystals has been observed by other researchers in the Gd-Se system [19,20] and is problematic since their presence can substantially lower the strength of the material by weakening the grain boundaries. One of the most severe cases is illustrated in the optical micrograph shown in Fig 1b. It would seem reasonable that these crystals correspond to the R_2Se_3 composition, since the band gap increases with increasing Se/R ratio and the red color, when viewed in transmission, indicates the presence of a band edge on the order of 2.0 to 2.3 eV. A sample of the material shown in Fig. 1b was examined with a microprobe to determine the compositional relationship between the red precipitation phase and the matrix. These results are shown in Fig. 2.

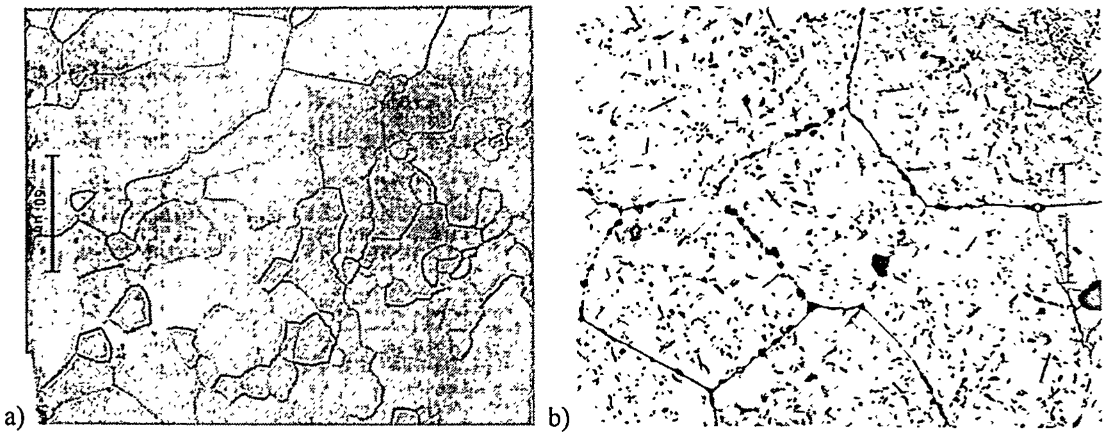

Fig. 1. Optical micrograph of polished and etched surface of (Nd-Ge)Se_y
Left: Typical microstructure of good quality samples
Right: Example of severe precipitation of red crystals

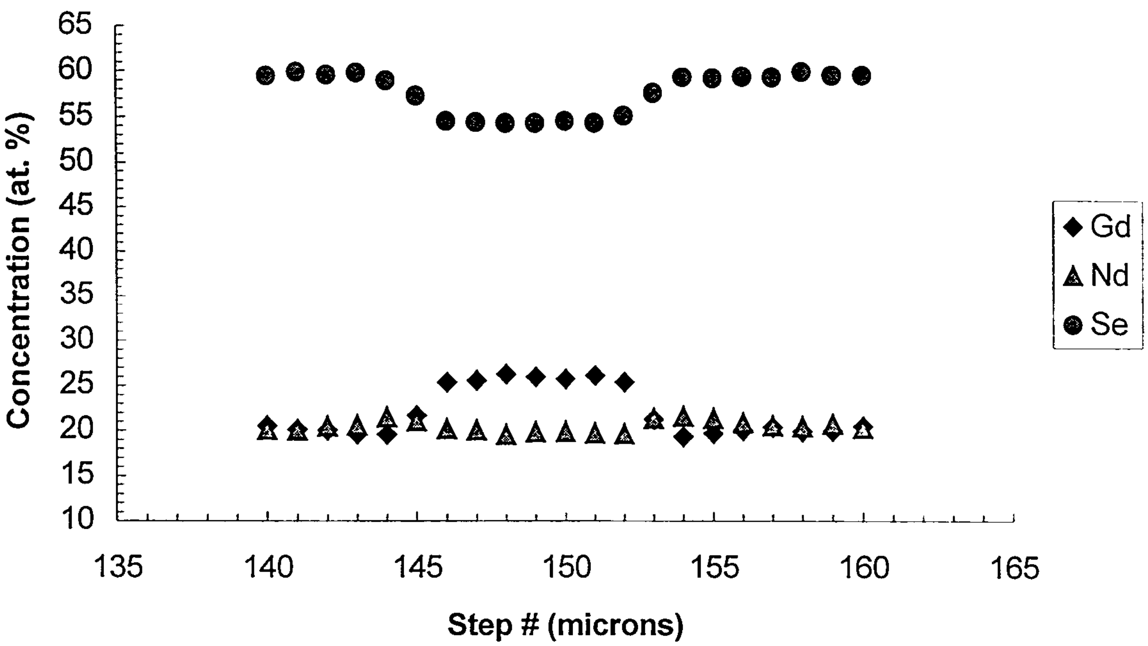

Fig. 2. EPMA scan through red crystalline precipitate phase (located between 145 and 154 microns) in $(Gd_{50}Nd_{50})Se_{1.480}$

The data were acquired in 1 μm increments across one of the grain boundary precipitates. The scan shows a relatively sharp change in composition upon going from matrix to precipitate and then back to matrix. The microprobe result shows that the composition of the matrix is close to that of the nominal value of Nd:Gd:Se = 1:1:3, however, the observed selenium content through the precipitate was less than that of the matrix. The data indicated that the red phase is a separate compound around Nd:Gd:Se 2:3:5 or 2:2.5:5.5 which falls within the RSe to $RSe_{1.22}$ range. This is surprising since it was expected that the composition of the precipitate is $(Nd_{50}Gd_{50})Se_{1.50}$. The difference between x=0 and x=0.02 in $(Gd_{50}Nd_{50})Se_{1.50-x}$ is near the limit of the precision that can be achieved with the microprobe, even with optimum surface preparation. Pure selenium was employed as a standard; however, use of a selenium intermetallic might afford better accuracy. Since the compositional homogeneity range of the Th_3P_4 structure extends only to $RSe_{1.33}$, the red precipitates must be of a different crystal structure than the matrix. Orientation imaging microscopy (OIM) was employed to identify the crystal structure of these precipitates, however, the scans failed to produce Kukuchi patterns of sufficiently high resolution to enable indexing.

Characterization of the hot pressed compacts by x-ray diffraction demonstrated that each sample had the desired γ (bcc Th_3P_4) defect structure, as shown in Fig. 3. The lattice parameter of three compositions was determined from the x-ray data and a Nelson-Riley method. The results are shown in Table I. The density of each compact was determined by Archimedes technique, and each sample was found to have a density in the 7.053 to 7.056 g/cm^3 range, which is within 2 % of theoretical.

Table I. Precision lattice parameters of three compositions of $(Nd_{50}Gd_{50})Se_{1.50-x}$

Sample ID	Composition (1.50-x)	a_o (nm)
35-52A	1.485	0.8791
35-54A	1.490	0.8789
35-56A	1.495	0.8790

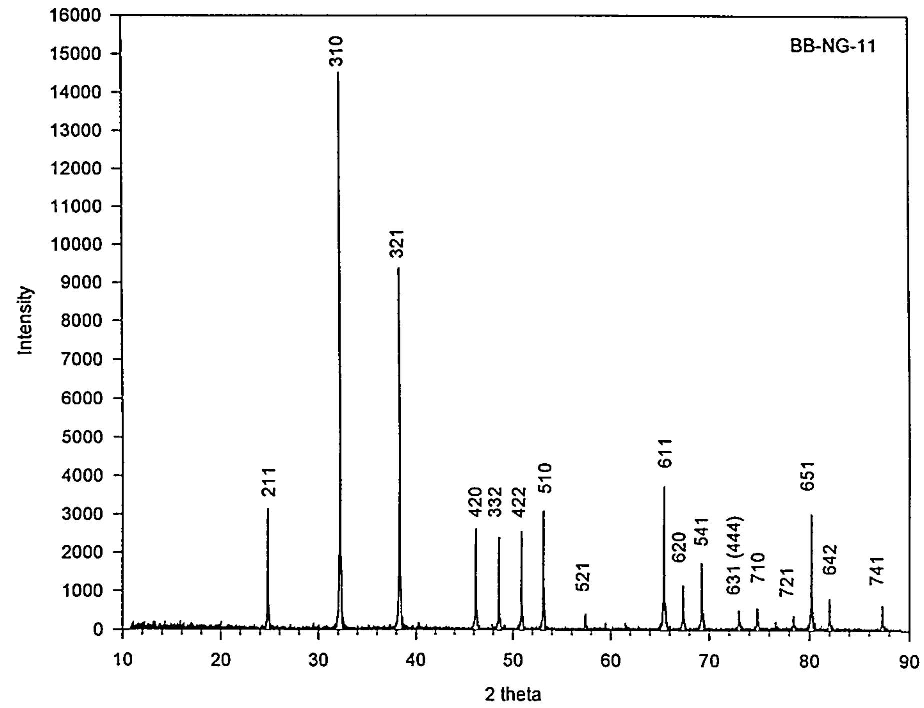

Fig. 3. Typical X-ray diffraction pattern of melted and hot pressed $(Nd_{50}Gd_{50})Se_{1.50-x}$ showing Th_3P_4 crystal structure.

7.4.2 Effects of Hot Pressing Temperature

A 250-gram quantity of $(Nd_{0.5}Gd_{0.5})Se_{1.495}$ was initially prepared by vapor phase reaction for 1 week at 1000°C. The entire powder was then placed in an open W crucible and melted under positive pressure of argon. At 1000°C, significant vaporization and release of selenium occurred, which led to electrical arcing in the induction coil and a subsequent water leak. The material was recovered and subsequently placed in a clean W crucible which was positioned inside a Ta crucible. A Ta lid was arc welded to the top of the crucible and a small pinhole was fabricated in the top. The mixture was heated to 1750°C, again under positive pressure. The ingot was removed from the crucible and samples were chemically analyzed by ICP-AES for R/Se ratio. The results from each of 16 distinct samplings is shown in Fig. 4. It was found that the final composition corresponded to $RSe_{1.495}$, consistent with congruent loss of RSe during the initial melting procedure.

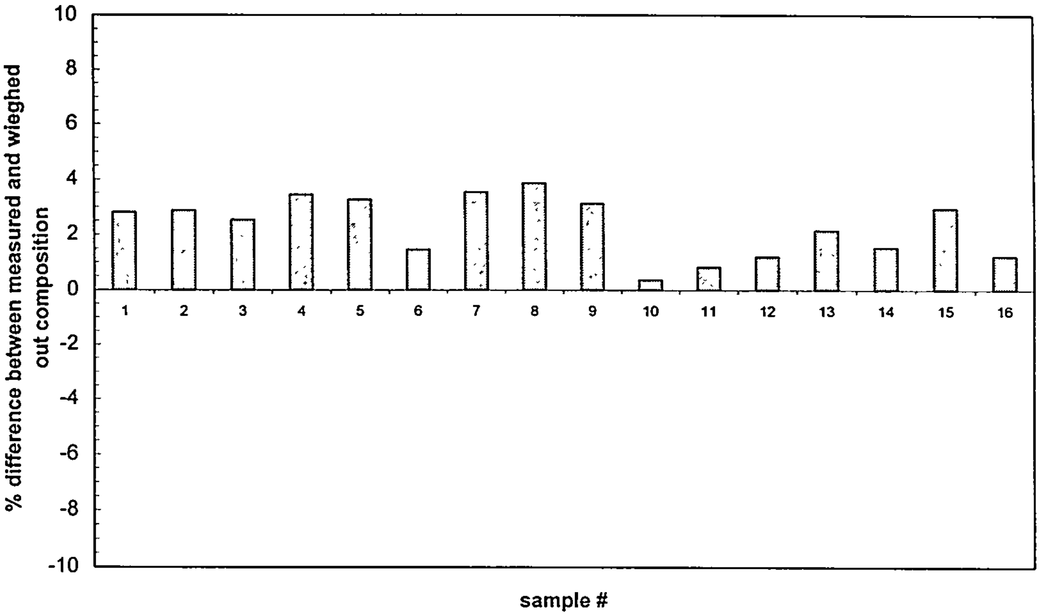

Fig. 4. Measured deviation in composition between nominal and final hot pressed compositions of 16 samples taken from 250-gm. master alloy. Rare earth and chalcogen concentrations were measured by ICP-AES. Nominal composition of master alloy was 1.480. Positive deviation indicates increase in Se/R ratio.

A portion from the top and bottom were mixed together and hot pressed at 1175°C for 60 minutes with an applied pressure of 80 MPa (11,390 psi). After furnace cooling, the sample was removed and exhibited no evidence of fracture. Room temperature electrical measurements of resistivity, mobility, and carrier concentration gave the following results: $\rho = 5.9$ mΩ-cm, $\mu = 5.1$ cm^2/V-s, $n = 2.1 \times 10^{20}$ cm^{-3}.

If the primary vaporization mechanism of $RSe_{1.50-x}$ is selenium, preparation of $RSe_{1.50}$ in sealed ampoules followed by grinding and hot pressing might result in sufficient loss of selenium to yield a $RSe_{1.490}$ to $RSe_{1.495}$ composition. One such sample was prepared with a nominal composition of $RSe_{1.50}$. During initial hot pressing experiments, a friable material with red crystals dispersed throughout was obtained. Evidently, either Se did not vaporize in sufficient quantity through the graphite die to yield $RSe_{1.495}$, or congruent vaporization occurs, i.e., the vaporization product is primarily RSe. A small quantity (i.e., 20 grams) of the 1.48 material was mechanically milled for 60 minutes in a Spex 8000 to homogenize the powder. This powder was then hot pressed at 1500°C for 30 minutes at 80 MPa. The compact was ground and heat treated under vacuum (10^{-6} Torr) at 1530°C for 6 hours in order to facilitate vaporization of the chalcogen. The powder was then hot pressed a second time at 1500°C and the resulting microstructure of the compact exhibited an anomously high density of both inter- and intragrannular red precipitates, shown in Fig. 1b. This observation supports the theory that the vaporization mechanism is congruent loss of RSe. Previous observations by 3M and General Atomic indicated that loss of Se occurs more rapidly at a given temperature in the Nd-Se system than in the Gd-Se system.

Additional samples were taken from the 250 gm. 1.48 "master" ingot and ground for a study of optimum hot pressing temperature of this composition. The evaluation criterion was the magnitude of the electrical power factor. Samples were hot pressed at 1100, 1200, 1300, 1400, and 1500°C for 60 minutes. These materials were quite sensitive to thermal shock; several fractured during cooling, requiring multiple hot pressing attempts. Most of the samples contained intragrannular and intergrannular red-orange precipitate phase. Nucleation of this phase appears favored by high impurity content, especially oxygen. The presence of this phase within the grain boundaries reduces the mechanical strength of the material and makes it more susceptible to fracture.

The electrical resistivity and Seebeck coefficient of these samples is shown in Figs. 4 and 5, respectively. The samples generally exhibit metallic behavior and there is a 30% variation in resistivity values, depending on the specific hot pressing temperature. Determination of the electrical power factor, S^2/ρ, shows that the optimum pressing temperature lies within the 1100 - 1200°C range; however, a lack of systematics in these data may be due to the inability to control temperature precisely during cooling to eliminate formation of microcracks. The room temperature carrier mobility of all samples was found to lie between 5 and 6 cm^2/V-s, regardless of pressing temperature. This is somewhat unusual since higher pressing temperatures tend to yield larger-grained microstructures with accompanying increases in carrier mobility in conventional band-type conductors. While larger grains were observed in the 1400 and 1500°C sample, the relatively high density of the precipitate phase may increase the carrier scattering rate to the point that the relaxation time is essentially independent of grain size. If these materials can be prepared free of the $RSe_{1.50}$ precipitates, some increase in mobility may result, with a corresponding increase in ZT. Metallographic examination of each sample revealed the presence of the insulating phase in most specimens, regardless of the hot pressing temperature. A series of smaller-scale (i.e., 10 to 12 gram) quantities of the following compositions were then prepared by direct reaction and melting: 1.485, 1.490, and 1.495. After hot pressing, each of the three compositions appeared to have varying degrees of the red, insulating phase dispersed throughout. When scratched with a razor blade, the 1.495 was quite soft and the abraded material appeared distinctly orange in color. With decreasing Se/R ratio, the surface appeared progressively more metallic. The room temperature Seebeck coefficient of samples that were hot pressed at 1175°C were measured with the results shown in Table II. Repeated measurements on the 1.495 specimen gave results that alternated between -840 and -775 μV/°C. The initial measurement consistently gave the higher values and only these were used in the averaging. The lower value probably corresponds to a non-equilibrium state in which a ΔT remains in the sample even though the external thermocouple indicated no temperature difference.

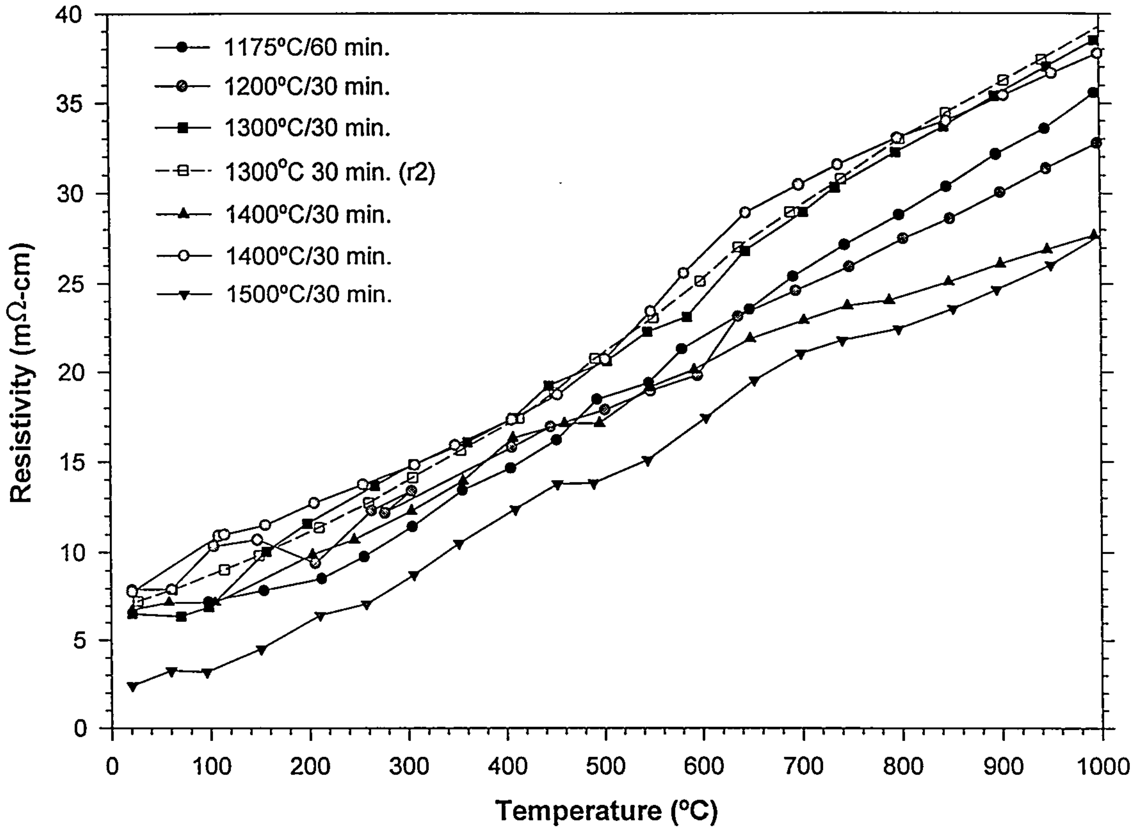

Fig. 4. Electrical Resistivity of $(Nd_{0.50}Gd_{0.50})Se_{1.48}$ Hot Pressed at Different Temperatures
(all samples taken from the same master lot)

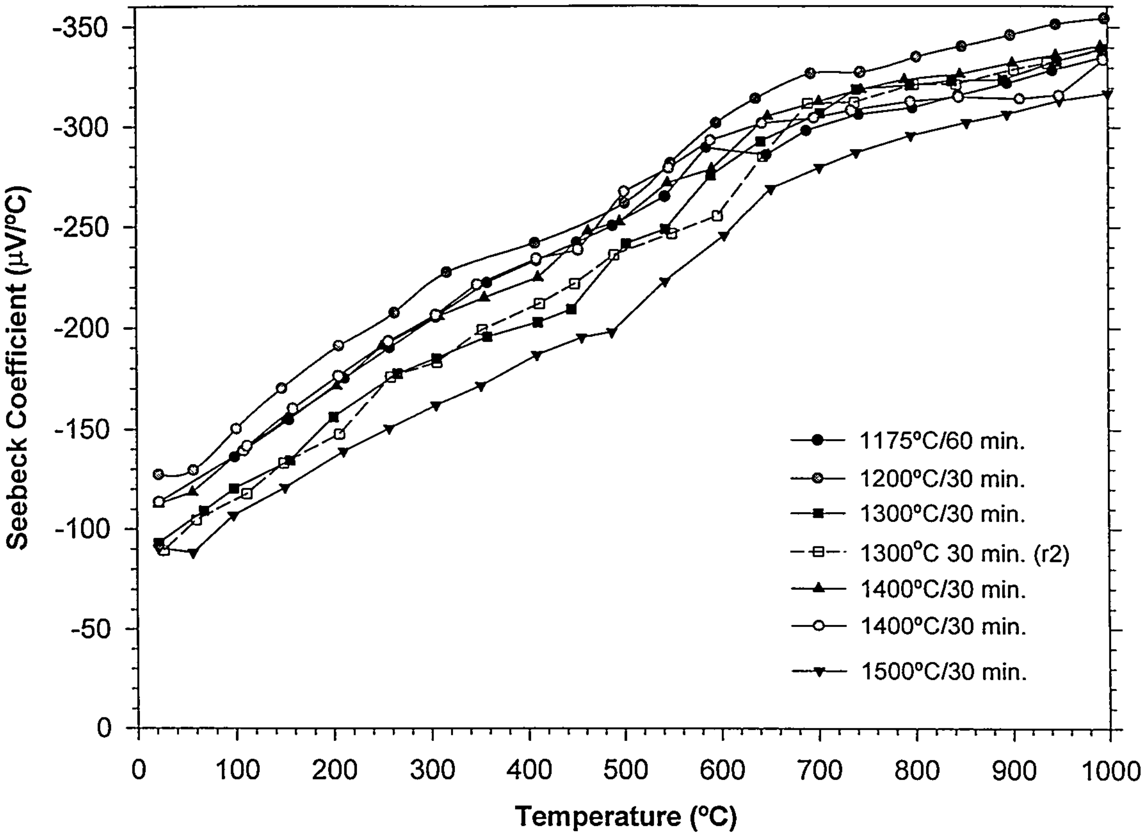

Fig. 5. Seebeck Coefficient of $(Nd_{0.50}Gd_{0.50})Se_{1.48}$ Hot Pressed at Different Temperatures
(all samples taken from the same master lot)

Table II. Room temperature Seebeck coefficient of three small-scale compositions of $(Nd_{50}Gd_{50})Se_x$.

Sample	Nominal Composition, x	$<S_o>$ (μV/°C)
35-52A	1.485	-170.0
35-54A	1.490	-147.5
35-56A	1.495	-842.9

Thus, the lower values probably correspond to a bucking voltage.

7.4.3 Effect of Nd substitution

According to Reid [21], chalcogens containing Nd generally exhibit similar properties to those containing Gd. Two small scale (10 gram) samples of nominal composition $RSe_{1.485}$ were prepared by direct reaction, melting, and hot pressing at 1175°C as described previously. One sample contained no Nd, i.e., $GdSe_{1.485}$ while the other sample contained a 50:50 ratio of Gd to Nd, $(Nd_{50}Gd_{50})Se_{1.485}$. The room temperature Seebeck coefficient of both samples was -170.4 ± 1 μV/°C, indicating that the presence of Nd has no effect on the Seebeck coefficient. Samples of $(Nd\text{-}Gd)Se_{1.480}$ were wrapped in Ta foil, sealed in quartz ampoules, and heat treated at 900°C for varying times up to 1000 hours. According to Wei [22] the transformation in $GdSe_{1.490}$ can be described by

$$\ln\left[\frac{1}{1-x}\right] = kt^{m} \qquad (1)$$

where x represents the volume fraction transformed, t is the time, and m has the value 1.7, as determined empirically. The peak transformation rate was observed to occur near 900°C, where 60 volume percent was observed to have transformed after 100 hours and 95 percent transformed after 300 hours. Since the transformation is diffusional in nature, higher temperatures result in a decrease in nucleation rate and at lower temperatures, the growth rate falls off. X-ray diffraction was performed on the samples after 500 and 1000 hours in order to determine the phases present. The resulting patterns showed no evidence of transformation from the cubic to the orthorhombic phase, indicating that the addition of Nd does, in fact, stabilize the gamma phase as expected.

7.4.4 Analysis of Transport Properties

7.4.4.1 Electrical Resistivity

Based on the preliminary work described above, optimum composition in the RSe_y system appears to fall with the range $1.450 \leq y \leq 1.490$. Samples with higher Se:R ratios have a resistivity too large to be of use for thermoelectric applications, whereas materials with lower Se:R ratios are too metallic. Consequently three samples with nominal compositions of $(Nd_{50}Gd_{50})Se_y$ where y = 1.470, 1.480, and 1.490 were prepared for additional study of transport behavior in this system. The temperature dependence of the electrical resistivity of these samples is shown in Fig. 6. These samples exhibit metallic-like conductivity with a positive temperature coefficient of resistivity. Undoped $RSe_{1.50}$ (i.e., R_2Se_3) is a semiconductor and as such, would exhibit a negative temperature coefficient of resistivity, if not for the self-doping. The data corresponding to the 1.470 composition appear anomalous and the discrepancy is believed due to the presence of oxygen during handling of the powders. The change in carrier concentration going from the 1.50 to the 1.48 or even 1.49 composition is apparently sufficient to cause a transition to metallic-like conductivity. The room temperature resistivity, ρ, carrier concentration, n, and Hall mobility, μ, were measured on a thin slice of the 1.480 material and gave the following results: ρ = 4.5 mΩ-cm, $n = 2.9\times10^{20}$ cm^{-3}, and $\mu = 4.9$ cm^2/V-s. According to Gschneidner [13], the number of conduction electrons per atom is given by

$$N_e = (3-2x)/(1+x) \qquad (2)$$

when the chemical formula is expressed as RSe_x. When the value of x = 1.480 is substituted into this relationship, one obtains a predicted number of electrons per metal atom of 0.016. Since there are 12 metal atom sites per unit cell in this structure, there should exist 0.192

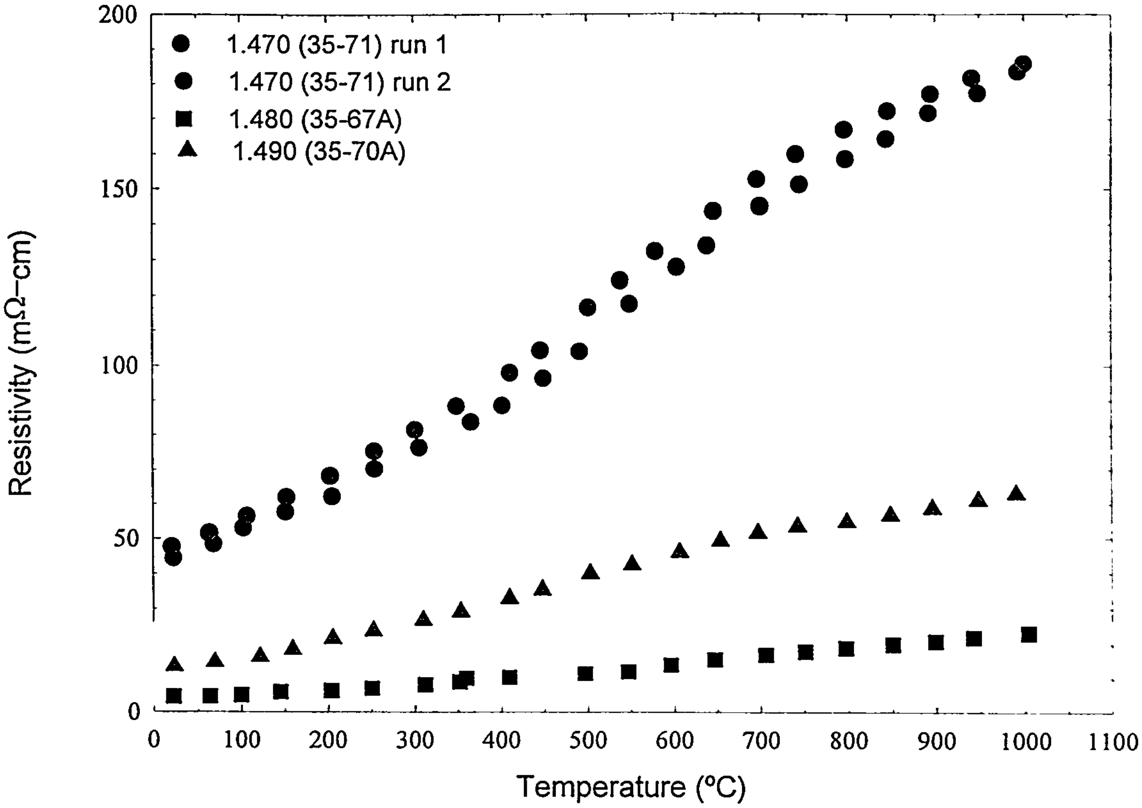

Fig. 6. Temperature dependence of electrical resistivity of $(Nd_{50}Gd_{50})Se_y$

conduction electrons per unit cell. From x-ray data, the unit cell volume is 6.8x10^{-22} cm^3, which means a total of 2.8x10^{20} conduction electrons per cm^3. The experimental result shows excellent agreement with the predicted value and indicates that the composition is quite close to the nominal value, since a composition of 1.490 would have a theoretical carrier concentration of 1.4x10^{20} cm^{-3} and a 1.470 would have a carrier concentration of 4.3x10^{20} cm^{-3}.

In intrinsic semiconductors, the energy gap can be estimated from an Arrhenius relation of the form

$$\sigma = \sigma_o \exp\left\{-\frac{E_g}{2kT}\right\} \qquad (3)$$

where E_g is the band gap energy, k is Boltzman's constant, and T is the absolute temperature. The electrical resistivity in these materials appears metallic over the entire temperature range indicating that they are extrinsic throughout the entire temperature range studied. However, when ln(σ) is plotted against reciprocal temperature, an indication of intrinsic behavior is observed at temperatures above 670°C as shown in Fig. 7.

7.4.4.2 Seebeck coefficient

The temperature dependence of the Seebeck coefficient of these samples is shown in Fig. 8. The Seebeck coefficient of these samples generally follows the temperature dependence of the resistivity, increasing with increasing temperature. A deviation is observed at the highest temperatures in the 1.47 and 1.49 samples. The magnitude of the 1.47 sample is inconsistent with the nominal composition, and indicates that this sample is Se-rich, possibly near a 1.495 composition. The relatively large thermopower is believed to be a consequence of a large effective mass of the carriers in this system. One can estimate the effective mass by combining the results of Seebeck coefficient and Hall effect measurements, assuming a single band conduction model. When the distribution of carriers is described by Fermi-Dirac statistics, as in the case of partial degeneracy, one can write the carrier concentration, n, in terms of the effective mass, m^*, as

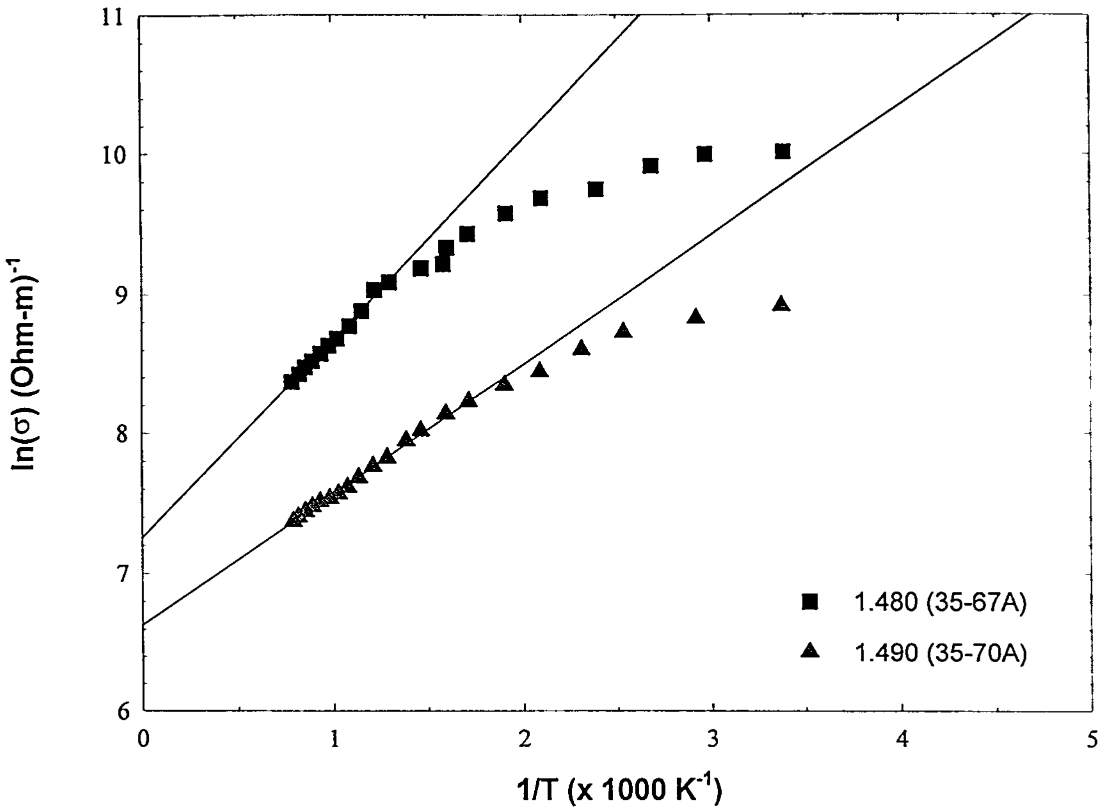

Fig. 7. ln(σ) vs. reciprocal temperature for $(Nd_{50}Gd_{50})Se_{1.480}$ and $(Nd_{50}Gd_{50})Se_{1.490}$

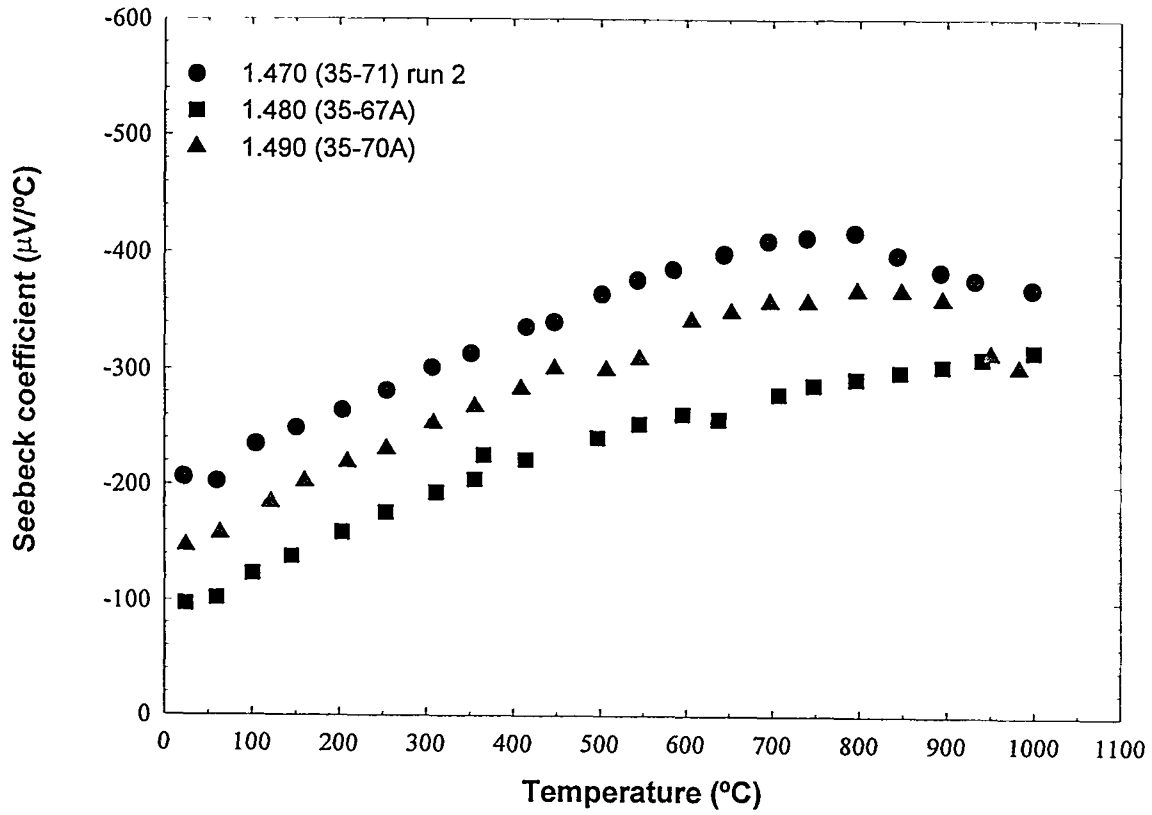

Fig. 8. Temperature dependence of Seebeck coefficient of $(Nd_{50}Gd_{50})Se_y$

$$n = \frac{4}{\sqrt{\pi}} \left(\frac{2\pi m^* kT}{h^2} \right)^{3/2} F_{\frac{1}{2}}(\mu) \qquad (4)$$

where k is Boltzmann's constant, h is Planck's constant, T is the absolute temperature, μ is the reduced Fermi energy (in units of kT), and $F_{1/2}(\mu)$ is the Fermi integral, which has the form

$$F_{\xi}(\mu) = \int \frac{\xi^x}{(1 + \exp(\xi - \mu)} d\xi \qquad (5)$$

The Seebeck coefficient, S, can be written as [16]

$$S = -\frac{k}{e} \left[\frac{(2+s)F_{1+s}(\mu)}{(1+s)F_s(\mu)} - \mu \right] \qquad (6)$$

where s represents the scattering parameter, which is taken as 0 for acoustic mode lattice scattering, 2 for ionized impurity scattering, and 1 for mixed scattering. The simplest approximation is to assume lattice (phonon) scattering. The carrier concentration and Seebeck coefficient at 293K for the 1.48 and 1.49 samples are shown in Table III.

The large effective masses explain the high Seebeck coefficient values in these materials. Other mechanisms, such as complex structure in the density of states near the Fermi energy, may also contribute to the large Seebeck coefficient. For example, Goryachev et al. [23] performed first-principles theoretical calculations which indicated that the conduction band in rare earth chalcogenides is complex, with a mixture of 6s, 5d, and 4f states. The presence of localized d-levels with a high density of states would give rise to sharp features in the d(ln(N))/dE curve near E_f which results in large values for the Seebeck coefficient.

The electrical power factor, defined as S^2/ρ, is plotted against temperature in Fig. 9. The maximum power factor among the compositions investigated occurs between 400°C and 700°C with a peak magnitude of 5.5 μW/cm-°C^2 in the 1.480 system. In order to determine

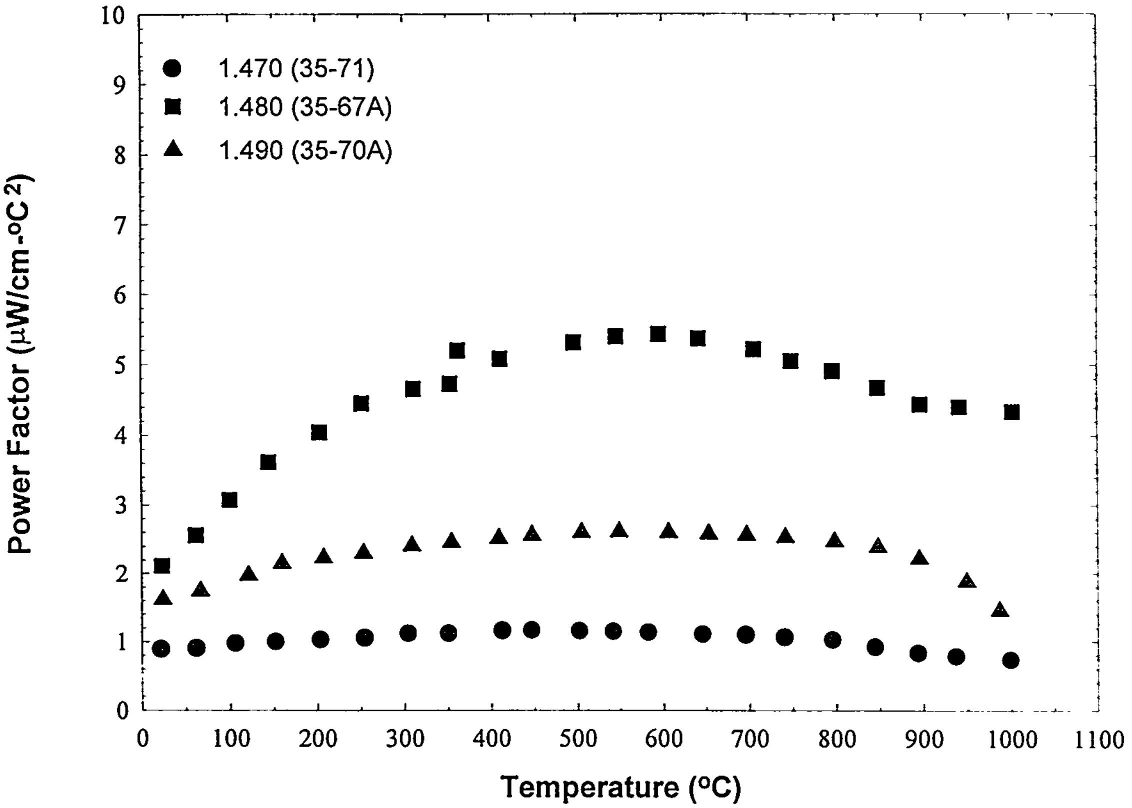

Fig. 9. Temperature dependence of electrical power factor, S^2/ρ, for three samples of $(Nd_{50}Gd_{50})Se_y$

Table III. Transport coefficients samples at 293K

Sample	n x10^{26} m^{-3})	S (μV/K)	μ^* (kT)	m^*
1.48 (35-67A)	2.87	-97	2.5	2.2
1.49 (35-70A)	1.09	-145	1.1	1.9

μ^* represents the reduced Fermi energy, in units of kT

the degree to which the power factor in the $(Nd_{50}Gd_{50})Se_{1.480}$ system is near optimum for this composition, a Jonker analysis was performed using the electrical data obtained from the individual hot pressings of the 1.480 material taken from the 250-gm master lot. Assuming a single band conductivity model, one can write

$$\sigma = ne\mu \qquad (7)$$

where σ is the electrical conductivity, n is the carrier concentration, e the electronic charge, and μ the carrier mobility. Also, if these materials can be described by simple band theory in the Boltzman transport approximation, then

$$S = \left(\frac{k}{e}\right)\left(\ln\left(\frac{N_E}{n}\right) + A\right) \qquad (8)$$

where S is the Seebeck coefficient, k is Boltzman's constant, N_E is the density of states at the Fermi level, and A is the scattering parameter which typically ranges between 0 and 2. By combining equations 7 and 8, one arrives at a simple expression for S in terms of ln(σ):

$$S = \left(\frac{k}{e}\right)\ln(\sigma) - \left(\frac{k}{e}\left(\ln\left(N_E e\mu\right) + A\right)\right) \qquad (9)$$

indicating that a plot of S versus ln(σ) should be linear with a slope equal to (k/e). Such a plot for the various 1.480 samples hot pressed at temperatures ranging from 1100°C to 1500°C was constructed. From this plot, a value of 11.8 was obtained for the logarithm of the intercept (i.e., $\ln(\sigma_o)$) and this result was used to construct a plot of $S^2\sigma$ as a function of σ as shown in Fig. 10. The maximum power factor, obtained differentiating the curve with respect to σ and setting the result equal to zero, gives a $(S^2\sigma)_{max}$ of 5.4 μW/cm-°C^2, corresponding to a resistivity of 5.5 mΩ-cm and a Seebeck coefficient of – 172.3 μV/°C. Thus, it is seen that the small-scale 1.480 composition with a peak power factor of 5.6 μW/cm-°C^2 is representative of nearly optimal electrical behavior.

7.4.4.3 Thermal conductivity

The thermal conductivity, k, of a semiconductor is the sum of a lattice component, k_l, due to phonon propagation, and an electronic component, k_e, due to heat transported by charge carriers. At sufficiently high temperatures, usually above 1500°C, a radiation component can also be appreciable. The lattice component is a function of the degree of phonon scattering, which depends on a number of variables. In elemental semiconductors above the Debye temperature, the lattice component is determined by the phonon scattering rate, which has a positive temperature dependence. As the scattering rate increases, the thermal conductivity decreases according to the relationship

$$k_l \propto T^{-1}. \qquad (10)$$

In alloy semiconductors, there is also a point defect contribution to the phonon scattering rate which reduced the lattice thermal conductivity by an amount proportional to the difference between the atomic mass of the ith atom and the average atomic mass of the alloy. According to Klemens [24] the point defect contribution to the lattice thermal conductivity can be written as

$$k_l \propto T^{-\frac{1}{2}}\varepsilon^{-\frac{1}{2}} \qquad (11)$$

where T is the absolute temperature and ε is a mass-fluctuation parameter, defined as

$$\varepsilon = \sum \frac{C_j(m_j - M)^2}{M^2} \qquad (12)$$

in which C_j is the concentration of the jth element of mass m_j, and M is the weighted average atomic mass, given by

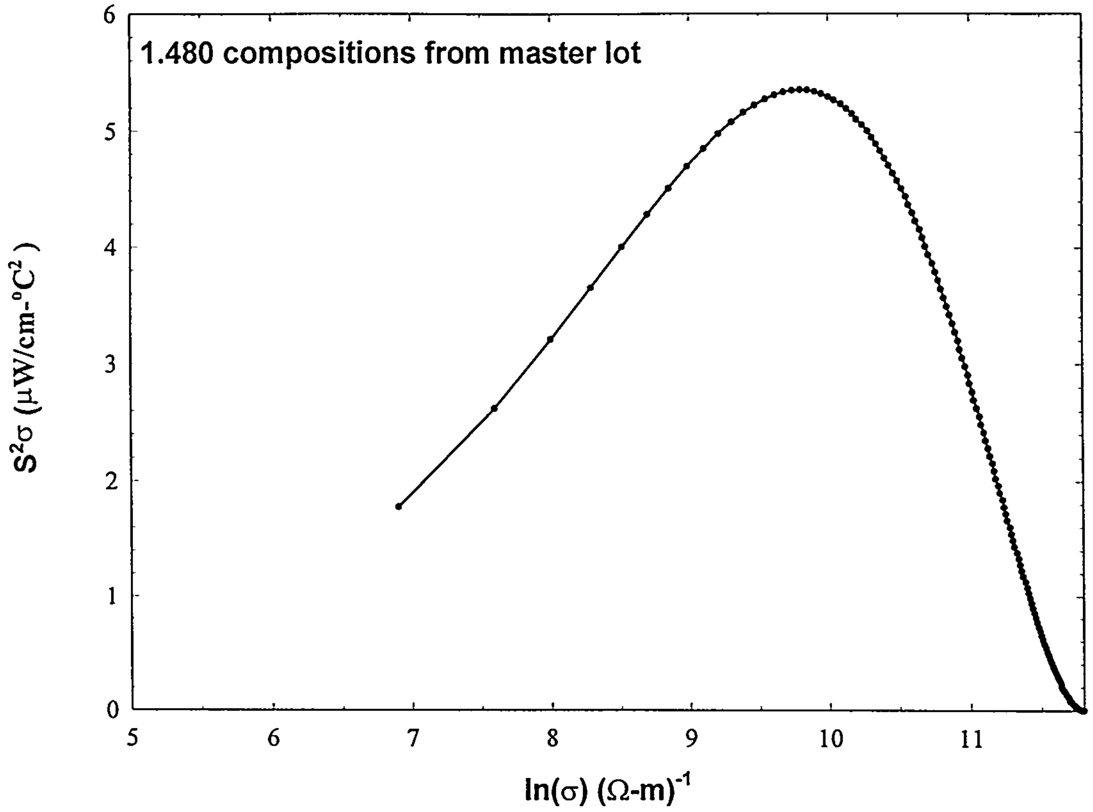

Fig. 10. Jonker plot of electrical resistivity and Seebeck coefficient of $(Nd_{50}Gd_{50})Se_{1.480}$ obtained from samples hot pressed at different temperatures.

$$M = \sum C_j m_j \qquad (13)$$

When the appropriate values for concentration and mass are substituted for $GdSe_{1.50}$ and $(Nd_{50}Gd_{50})Se_{1.50}$, the results indicate that the substitution of Nd ($\varepsilon = 0.11$) should not provide any significant decrease in thermal conductivity relative to $GdSe_{1.50}$ ($\varepsilon = 0.12$), the atomic mass being close to that of Gd and falling between that of Gd and Se. The thermal diffusivity of two of the compositions, a 1.480 and a 1.490, were measured between room temperature and 1000°C and the results are shown in Fig. 10. Also shown in the figure is a partitioning of the lattice and the electronic components, as determined from the Wiedeman-Franz law,

$$k_e = L_o \sigma T \qquad (14)$$

where σ is the electrical conductivity, T the absolute temperature, and L_o is the Lorenz number, which, in the case of a degenerate electron gas, assumes the form

$$L_o = \left(\frac{5}{2} + r\right)\left(\frac{k}{e}\right)^2 \qquad (15)$$

where r is the scattering parameter, which has a value of 0 for acoustic mode lattice scattering, 2 for ionized impurity scattering, and 1 for mixed scattering. The total thermal conductivity decreases with temperature, reaching a minimum near 600°C, and then rises slightly above this temperature. The magnitude of the thermal conductivity of both compositions is quite low, ranging from 9 mW/cm-°C near room temperature, to 4.5 mW/cm-°C near 600°C. Wood [25] claims that the electronic component is the dominant contribution in the $R_{3-x}X_4$ system, however, our results do not agree with this conclusion. The electronic component in this system does not appear to constitute more than about 40 % of the total thermal conductivity. The increase in k with temperature does not appear to be an electronic artifact, as seen from the nearly constant temperature dependence of the electronic component. Since most of the obvious mechanisms cause the phonon scattering rate to increase with temperature, the reason for this anomalous behavior remains unclear.

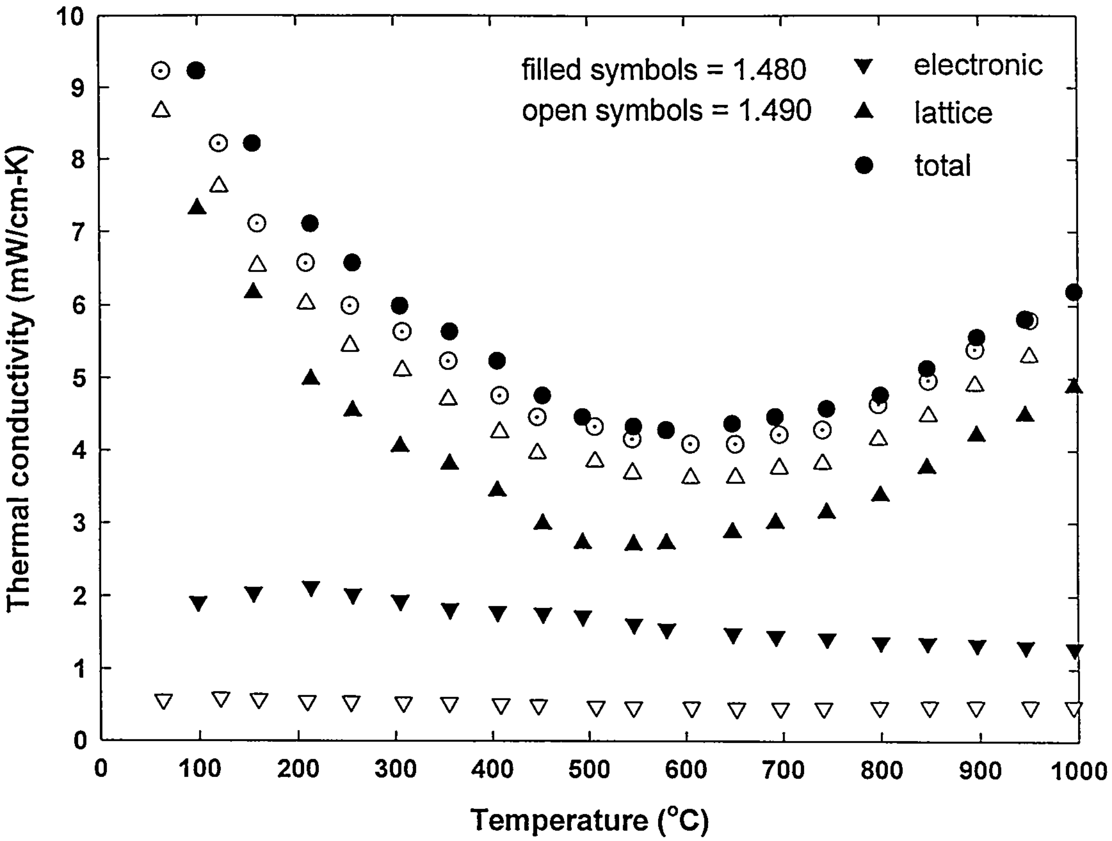

Fig. 10. Lattice, electronic, and total thermal conductivity of $(Nd_{50}Gd_{50})Se_{1.48}$ and $(Nd_{50}Gd_{50})Se_{1.49}$.

The low thermal conductivity in this system can be attributed to three favorable factors; a complex unit cell containing 28 atoms, a low Debye temperature, and the disorder on the metal sites resulting from the random vacancies in the Th_3P_4 defect structure. The lattice thermal conductivity tends to follow the number of atoms per unit cell, N, according to

$$k_l \propto N^{-\frac{2}{3}} \qquad (16)$$

According to Wood [25], the Debye temperature, θ_D, of the rare earth chalcogenides is low, on the order of 200 to 400K, and the lattice thermal conductivity is proportional to θ_D^3. Moreover, as the composition changes from the metallic R_3Se_4 to the semiconducting R_2Se_3, disorder on the cation sites increases, reaching a maximum of 4/3 of the sites per unit cell or 4.76 at. % vacancies. This disorder contributes to anharmonic scattering and further reduces the thermal conductivity. The thermal conductivity of GdS_y was measured by Gadzhiev, et al. [9] who report a lattice contribution nearly twice that observed in this study. However, the microstructure and phase distribution was not mentioned. Taher and Gruber [26] characterized the thermal conductivity of $DyS_{1.496}$ and reported a magnitude of 1 mW/cm-°C above 200°C. It is likely that such an extremely low value is questionable, and the measurement technique was not discussed by the authors.

7.4.4.4 Figure of Merit

The dimensionless figure of merit for the 1.480 and 1.490 compositions is shown in Fig. 11. A strong dependence on the R/Se ratio is evident from the figure which shows that the ZT of the 1.480 composition exceeds unity, reaching a maximum of 1.23 between 750°C and 850°C whereas the ZT of the 1.490 composition within the same temperature range achieves a maximum of only 0.57. The increased Seebeck coefficient of the 1.490 relative to that of the 1.480 is insufficient to compensate for the reduced carrier concentration and mobility observed in the former.

While efforts to stabilize the cubic phase of $GdSe_y$ relative to the low temperature orthorhombic appear successful using a 50:50 ratio of Nd to Gd, the binary phase diagram indicates the possible existence of an ordered δ phase near this composition, which could

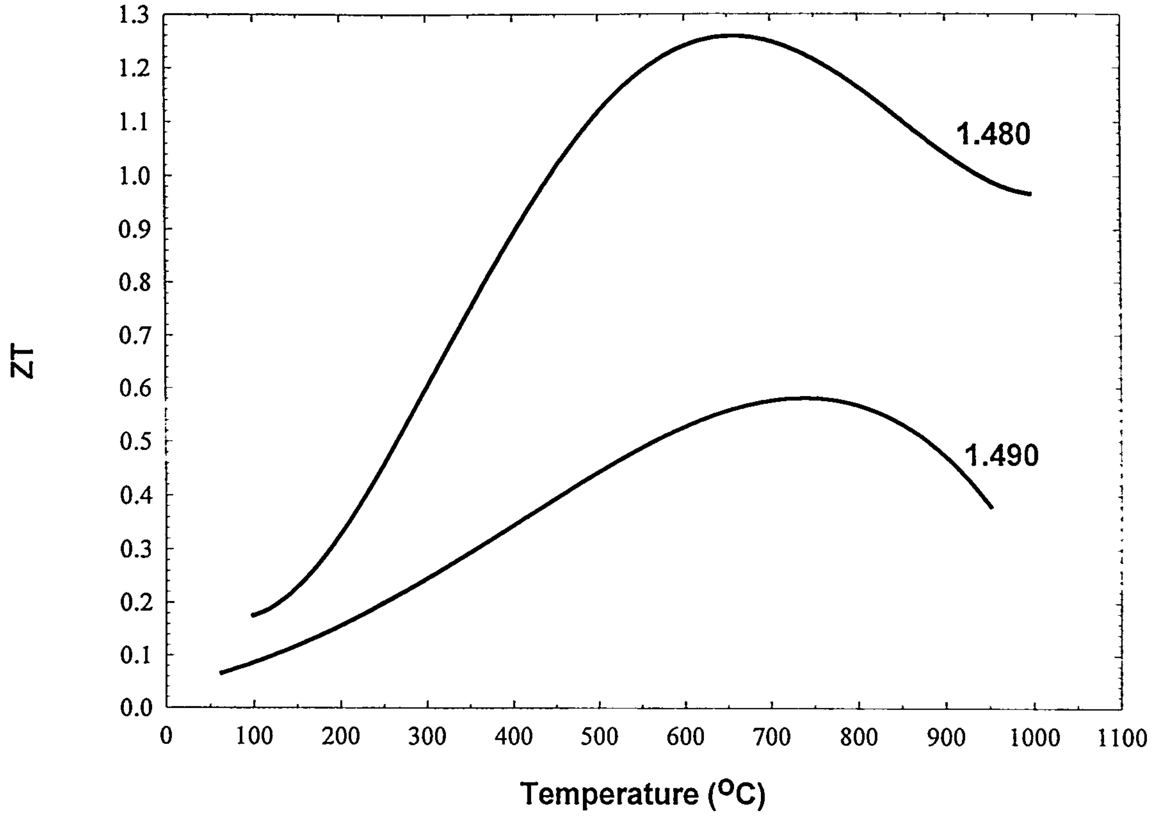

Fig. 11. Dimensionless figure of merit, ZT, of $(Nd_{50}Gd_{50})Se_{1.480}$ and $(Nd_{50}Gd_{50})Se_{1.490}$

affect the transport properties and mechanical behavior. Additional work to determine the minimum amount of Nd required would be useful. Additional work to resolve the anomalous behavior of the 1.470 samples relative to the 1.480 and 1.490 should also be performed.

7.5 Conclusion

Dimensionless figure of merit, ZT, values exceeding unity have been observed in $(Nd_{50}Gd_{50})Se_{1.50-x}$ where $x \approx 0.02$. The transport properties of these materials are quite sensitive to preparation and handling conditions, and minute amounts of oxygen contamination appear to promote nucleation of second phase oxyselenide phases which make sample reproducibility difficult. The materials exhibit electrical behavior characteristic of degenerately-doped semiconductors wherein the electrical resistivity and Seebeck coefficient display positive temperature dependence. The thermal conductivity in this system is quite low, on the order of 4 to 6 mW/cm-°C due to a combination of a complex unit cell, disorder on the cation sites, and a low Debye temperature.

7.6 Acknowledgement

The Ames Laboratory is operated by Iowa State University for the United States Department of Energy under contract W-7405-ENG-82. The microprobe analysis of Dr. Alfred Kracher is gratefully acknowledged. This project was funded by DARPA.

7.7 References

1. C. Zener, Westinghouse Corporation (personal commentary) (1959).

2. M. Fornari and D. J. Singh, Appl. Phys. Lett. 74 (1999) 3666.

3. D. J. Singh, T. L. Reinecke, W. E. Pickett, and P. J. Lin-Chung, Naval Research Reviews, U. S. Government Printing Office, 68 (1996) 4.

4. B. C. Sales, D. Mandrus, R. K. Williams, Science, 272 (1996) 1325.

5. G. C. Wei, "Phase Transformation and Processing of Polycrystalline Gadolinium Selenide, $GdSe_{1.49}$," J. Am. Ceram. Soc., 67 (1984) 664.

6. K. A. Gschneidner, Jr., private communication (1999).

7. W. C. Mitchell, R. B. Ericson, E. F. Hampl, Jr., R. M. Swinehart, K. C. Thompson, S. J. Thompson, and G. R. Wyberg, "Transport Theroy of 3M High-Performance Thermoelectric Materials," Proc. XI Intersociety Electrical Conversion Engineering Conference, p. 1539.

8. L. R. Danielson, S. Matsuda, and V. Raag, "Thermoelectric Properties of Rare-Earth Chalcogenides," Proc. V Inter. Conf. on Thermoelectrics, The University of Texas at Arlington, K. R. Rao, ed. (1984) 41.

9. G. G. Gadzhiev, Sh. M. Ismailov, M. A. Aidamirov, G. N. Dronova, P. P. Khokhlachev, and M.-R. M. Magomedov, "Physical Properties of Gadolinium Sulfides," Inorg. Mater. 33 (1997) 335.

10. M. Cutler, R. L. Fitzpatrick, and J. F. Leavy, J. Phys. Chem. Solids 24 (1963) 319.

11. M. Guittard, A. Bernacerraf, and J. Flahaut, "L_2Se_3 and L_3Se_4 Selenides of the Rare Earth Elements: Update," Ann. Chim., 9 91964) 25.

12. F. M. Ryan, I. N. Greenberg, F. L. Carter, and R. C. Miller, J. Appl. Phys. 33 (1962) 864.

13. K. A. Gschneidner, Jr., "Preparation and Processing of Rare Earth Chalcogenides," JMEPEG, 7 (1998) 656.

14. L. J. Van der Pauw, Phillips Res Rep. **13**, 1 (1958).

15. Z. Ndlela, and C. Bates, J. Rev. Sci. Inst. **60**, 3482 (1989).

16. G. T. Meaden, *Electrical resistance of Metals* (Plenum, New York, 1965), p. 143.

17. E. B. Hensley, Phys. Rev. **23**, 1122 (1952).

18. G. B. Kokos, K. A. Gschneidner, Jr., B. A. Cook, and B. J. Beaudry, J. Appl. Phys.

19. N. E. Elsner, Hi-Z Corporporation, San Diego, CA, private communication (1999).

20. B. J. Beaudry, Ames Laboratory, private communication (1998).

21. F. J. Reid, L. K. Matson, J. F. Miller, and R. C. Himes, "Electrical Properties of Selected Rare Earth Compounds and Alloys," J. Electrochem. Soc. 111 (1964) 943.

22. G. C. Wei, "Phase Transformation and Processing of Polycrystalline Gadolinium Selenide, $GdSe_{1.49}$," J. Am. Ceram. Soc. 67 (1984) 664.

23. Y. M. Goryachev, T. G. Kutsenok, and L. I. Zadvornyi, Izv. Akad. Nauk 4 (1968) 1912.

24. P. Klemens, Phys. Rev., 119 (1960) 507.

25. C. Wood, Rep. Prog. Phys., "Materials for thermoelectric energy conversion," 51 (1988) 459.

26. S. M. Taher and J. B. Gruber, Mater. Res. Bull., 16 (1981) 1407.

CHAPTER 8. GENERAL CONCLUSIONS

The search for thermoelectric materials possessing a figure of merit greater than unity has been an ongoing activity for over 40 years. New processing techniques, including molecular beam epitaxy, rapid solidification, and organometallic chemistry have enabled preparation of new, complex structures and properties unheard of at the dawn of the thermoelectrics renaissance in the 1950's. Advances in band structure calculations have provided improved theoretical guidance in the search for new bulk materials. Still, confirmed reports of materials having a ZT much greater than unity are scarce. Predictions of large ZT values in quantum well heterostructure devices appear to be substantiated by recent experimental evidence. However, the quantum confinement effects and related modification to the local band structure of materials deposited in these configurations fail to address the question of the limiting ZT values in bulk, or macroscopic material (i.e. with a phase or microstructural scale on the order of microns or larger). Many well-intentioned observers with a casual interest in thermoelectric materials regard $ZT = 1$ as an accepted fact, even though thermodynamics places no upper bound on ZT, only on Carnot efficiency. The question has fundamental scientific implications as well as technological and engineering ramifications. If ZT has an upper bound near unity, then the implication is that there exists a limit in the degree to which thermal and electrical currents can be de-coupled, beyond that normally ascribed to the Wiedeman-Franz relationship. The concept of a "phonon glass - electron crystal" implies a material in which the electrical conductivity behaves as in a single crystal, while the thermal conductivity responds as in a glass. Materials with large atomic displacement parameters (formerly called Einstein rattlers) offer the possibility of approaching this condition in bulk materials. Recent work on filled Skutterudites and related compounds has provided encouraging results with claims of $ZT \sim 1.5$. These materials are characterized by glass-like thermal conductivity due to the presence of weakly-bonded atoms within the unit cell that experience large anharmonic vibrations, scattering intermediate wavelength phonons.

The intent of this dissertation was to critically examine the thermoelectric properties of a number of alloy systems, with the objective of identifying and understanding the common characteristics required for the existence of a high figure of merit. The focus was directed mainly at semiconducting materials since these tend to exhibit the best overall combination of resistivity, Seebeck coefficient, and thermal conductivity. A brief summary of what has been learned follows.

Solid solution alloys of silicon germanium constitute one of the most technologically important classes of thermoelectric power generation materials. Since the mid-1970's, the production of on-board electrical power for planetary space probes has relied on the conversion of thermal to electrical energy provided by silicon-germanium alloys in radioisotope thermoelectric generators (RTGs). Given the significant effort that has gone into development and optimization of these alloys, it is appropriate that a discussion of two key aspects of the optimization be included in this dissertation; specifically, (1) an understanding of the role of oxygen contamination during processing and (2) the role and optimization of n-type dopants, P and GaP. In order to improve the performance of these materials, it is important to understand the role of impurities that are an inevitable consequence of handling and processing the raw materials. Central to this is the role of oxygen, since it is ubiquitous and highly reactive. While there is an exhaustive amount of information available on the role of oxygen in silicon up to the solubility limit, little had been published on the effects of oxygen in silicon-germanium alloys especially with regard to the transport properties. The heats of formation of SiO_2 and of Ga_2O_3 are both quite large and negative (-878.6 kJ/mole and -1075.3 kJ/mol, respectively) indicating that the formation of these compounds is thermodynamically favored. The presence of second phase oxides is likely to manifest itself in a slight shift of the lattice parameter as silicon is oxidized and the bulk composition of the alloy is shifted toward a more germanium-rich value. The presence of neutral second phase oxide impurities can lower carrier mobility through impurity scattering and by increasing the density of grain boundary potential barriers in alloys with a sufficiently fine-grained microstructure. Alloys having significantly different oxygen contents would likely exhibit microstructural variations that would in turn provide information about the nature of the sintering process. Normal solid-phase sintering is a diffusion-controlled process and proceeds through the reduction of surface energy. Second phase oxide particles, if segregated at grain boundaries, can act as pinning sites, retarding or preventing grain growth. The magnitude of the pinning effect depends on surface energy, crystal structure, and size of the particulates. Consequently, a heavily oxygenated specimen may show limited grain growth during hot pressing, particularly if the oxide is sufficiently fine and well dispersed. The objective of this component of the study was to determine the maximum tolerable oxygen level in current n-type Si-Ge thermoelectric materials as a compromise between high figures of merit and reasonable preparation and processing conditions. A starting point was to evaluate the variation in fundamental thermoelectric properties with the amount and distribution of oxygen in commonly obtained starting materials. The early work of Dismukes, et al. [21], provided an extensive background of both electrical and thermal properties of heavily doped, silicon-rich alloys and formed the groundwork for subsequent enhancements. Processing methods have since received considerable attention such as the application of hot pressed and sintered alloys [24], the study of grain-boundary scattering and the use of fine-grained alloys designed to lower the lattice thermal conductivity [25,26], application of high-temperature heat treatments to alter the microstructure and redistribute dopants [27,28], and control of second-phase oxygen [29].

Moreover, the claims regarding the effects of gallium phosphide additions, once thought to reduce the thermal conductivity [30] and later reported to increase the solid solubility of phosphorus [31], have had considerable impact on funding and subsequent research directions concerning Si-Ge thermoelectric alloys. Theoretical modeling of the n-type $Si_xGe_{(1-x)}$ system suggested that the optimum dimensionless figure of merit (ZT) at 1300K is in the range of 1.1 ($Si_{0.8}Ge_{0.2}$) [32] to 1.2 ($Si_{0.7}Ge_{0.3}$) [33], without the introduction of artifacts such as inert, nanophase phonon scattering inclusions. Standard zone-leveled Si-Ge n-type alloys, doped only with phosphorus, have a ZT value 17-20% lower than the theoretical maximum. The role and interaction of GaP and elemental P as dopants to the Si-Ge system were central to optimization of the material and control of the resulting microstructure.

Oxides have traditionally been disregarded as viable thermoelectric materials due to their large band gap and resulting low electrical conductivity. What is generally not appreciated about oxides is the wide range of electrical conductivity exhibited. For example, in TiO the Ti^{2+} d-orbitals are diffuse and give rise to bands rather than discrete energy states. These bands can accommodate up to 6 electrons. Ti^{2+} is a d^2 ion so the 2 d-electrons partially occupy the band. Consequently, TiO is a metallic conductor with a $\sigma \approx 10^3$ (Ohm-cm)$^{-1}$. Similar behavior is observed for other early transition metal oxides such as VO, ZrO, NbO, and HfO. In contrast, NiO exhibits more "conventional" oxide behavior due to decreased screening of the nuclear charge and contraction of the d-orbitals, making them less diffuse. Consequently, the t_{2g} levels form discrete states rather than a band. In addition, Ni^{2+} has 8 d-electrons which completely fill the t_{2g} level (which can accommodate six), leaving 2 additional electrons to populate the e_g orbital which has partial occupancy. The e_g orbitals cannot overlap with those on neighboring Ni ions to form bands, therefore, NiO is an electrical insulator. The trioxides of W and Re constitute a particularly interesting class of oxides. WO_3 is a pale yellow insulator due to an empty band resulting from the W^{6+} d^0 oxidation state whereas ReO_3 has a partially filled band due to the Re^{6+} d^1 oxidation state and is metallic with a room temperature conductivity within two orders of magnitude of copper! The electrical properties of WO_3 can be controlled by insertion of various alkali metals such as Na. For example, $Na_x(WO_3)$ contains an electron donated by the sodium which partially fills the π band making this material a gold-colored, good conductor. A study by Ohtaki et al.[34] examined $(Zn_{1-x}Al_x)O$ alloys where $x = 0 - 0.1$ for high temperature thermoelectric applications and reported a dimensionless figure of merit of 0.31 in $(Zn_{0.98}Al_{0.02})O$ at 1000°C. Tanaka et. al.[35] have examined various ZnO alloys doped with other oxides for thermoelectric applications and reported a power factor (S^2/ρ) between 1.0 and 3.0 μW/cm-K^2 near 1000°C. However, Wang et al. [36] examined the electrical properties of transparent thin films based on ZnO doped with Al_2O_3, Ga_2O_3, In_2O_3, and Ge_2O_3 and found that elemental Ga can act as a dopant, thereby increasing the electrical conductivity. The identification of potential dopants, combined with the possibility of isostructural alloying with ZnS, providing a mechanism to decrease the lattice thermal conductivity, motivated a systematic investigation into the optimization of ZnO-based thermoelectric materials as a way to improve thermoelectric conversion efficiency by increasing the hot side temperature. While a

ZT of only 0.3 was found in this system, that a value as large as this was obtained in a oxide was itself noteworthy and suggested that related systems may be worthy of examination.

Certain classes of intermetallic compounds, based on MNiSn where M=Ti,Zr, or Hf have been shown to exhibit semiconducting behavior and relatively large Seebeck coefficients [37,38,39]. Results of band structure calculations [40]have shown that the semiconducting properties are due to the formation of a gap in the density of states at the Fermi level when one of the nickel sublattices in the MNi_2Sn Heusler structure is removed, leaving a sublattice of ordered vacancies. The resulting "half-Heusler" MgAgAs structure becomes particularly attractive for thermoelectric applications because of the potential to reduce thermal conductivity through isoelectronic alloying on the M sites, and to optimize the carrier concentration through substitution on the stannide or nickel sites. Previous studies of the synthesis and properties of TiNiSn [41] demonstrated attractive electrical properties in the 300 to 600°C temperature range. Other researchers have examined substitutions for the Group IVA transition metal [42] and for the Group VIIIA transition metal [43]. Recent work on the Zr and Hf systems established the significance of structural disorder of the respective sites on the low temperature thermal properties [44]. Moreover, this study also demonstrated that a large fraction of heat is carried by phonons, opening up the possibility for reduction in thermal conductivity by alloying and other techniques. In addition, it was found that these alloys exhibited metal-like conductivity at low temperatures, changing over to semiconductor-like conductivity near ambient temperature. Such behavior is curiously reminiscent of paramagnetic to ferromagnetic transitions near the Curie point, where spin scattering of the carriers decreases upon entering the metal-like ferromagnetic state [45]. The objective of this study was to examine the elevated temperature electrical and microstructural characteristics of arc melted and annealed MNiSn, where M=Ti, Zr, or Hf, in terms of the effects of isostructural alloying on the M sites, as well as the effects of Sb doping on the Sn sites. This objective was accomplished by characterizing the electrical resistivity and Seebeck coefficient as a function of temperature between 300 and 1050K on polycrystalline samples of ZrNiSn, HfNiSn, $(Zr_{0.5}Hf_{0.5})NiSn$, $(Zr_{0.5}Hf_{0.5})NiSn_{0.995}Sb_{0.005}$, and $(Zr_{0.5}Hf_{0.5})NiSn_{0.990}Sb_{0.010}$.

Development and optimization of the high temperature n-leg component for a proposed 71 W/kg segmented thermoelectric generator was the goal of a research activity to synthesize and optimize alloys based on (Nd-Gd)$Se_{1.5-x}$. Since semiconductors exhibit an optimum thermoelectric conversion efficiency over a relatively narrow temperature range, segmenting different materials enables each one to operate within its optimum temperature range, thereby increasing the overall electrical output of the generator. Conventional materials such as Si-Ge have a thermal conductivity at least four times higher than the Pb-Te segments to which they would be bonded. This discrepancy results in thermal expansion mismatches and unequal heat flow down the segments. Rare earth selenides, with a much lower thermal conductivity than Si-Ge, are attractive candidates for the high temperature n-leg components of a segmented generator. While Gd_2Se_3 has been shown to have a ZT close to unity and is mechanically robust, it undergoes a phase transformation from cubic to orthorhombic at high temperatures, degrading the thermoelectric properties and resulting in crack formation. Neodymium does not exhibit such a transformation, however, Nd_2Se_3 is brittle and prone to mechanical failure. Substitution of Nd for Gd is expected to produce a stable cubic phase compound with good mechanical strength. The cubic (γ) phase of (Nd-Gd)Se_x exists in the Th_3P_4 "defect structure" wherein the metal atoms are randomly distributed among 12 lattice sites. At the 2:3 composition, each unit cell contains 10-2/3 metal atoms in a disordered structure. The disorder results in considerable phonon scattering and a low lattice thermal conductivity. Addition of metal atoms to the 1-1/3 unoccupied sites per unit cell increases the carrier concentration, resulting in metallic conductivity for the 3:4 composition. Samples of (Nd-Gd)Se_y where $1.450 < y < 1.490$ were synthesized and characterized for composition by microprobe, ICP, and XRD. Microprobe examination of transparent red precipitates indicated a different crystal structure than the Th_3P_4 matrix. Transport properties (electrical resistivity, Seebeck coefficient, thermal diffusivity, and electron mobility) were measured giving a maximum ZT = 1.1 at 800°C for the 1.480 composition. Analysis of transport data indicate that a large fraction (80%) of the heat is carried by phonons, suggesting that further increases in ZT are possible with incorporation of additional scattering mechanisms.

During the initial development of semiconductor thermoelectric materials in the late 1950's, there was general optimism regarding the ultimate efficiency of such devices. In fact, Zener, when asked why he estimated the ultimate efficiency of thermoelectric devices at (only) 35% replied that he wished to offer a prediction that was achievable. Today, the best thermoelectric devices have a conversion efficiency of about 10 percent, well below Zener's prediction of nearly 40 years ago and certainly much less than Carnot efficiency. Given the significance of the discovery of a material with a ZT >> 1 (at any temperature), both scientifically and technologically, a search for such a material is warranted. There are strong indications that ZT values greater than 2 may be found in heterostructures, in which mobility enhancement due to the physical separation between carriers and ionized impurities occurs. However, no such indications (yet) exist for bulk materials.

GENERAL REFERENCES

1 Strictly speaking, thermopower refers to the magnitude of the (open circuit) voltage for a given temperature difference, ΔT. Seebeck coefficient refers to the slope of the ΔV vs. ΔT curve.

2 Littman, H. and Davidson, B. J. Appl. Phys. 32 (1961) 217.

3 Ho, C. Ackerman, W. and Wu, K., "Thermal Conductivity of copper-nickel and silver-palladium alloy systems" Thermal Conductivity **14**, edited by P. Klemens and T. Chu, (Plenum Press, New York, 1976) 233-244.

4 Laubitz, M. J. and Matsumura, T., Canadian J. of Phys. 50 (1972) 196.

5 Aselage, T. L., "High temperature thermoelectric properties of boron carbide" in Modern Perspectives on Thermoelectrics and Related Materials, MRS Symp. Proc. 234, Allred, D., Vining, C., and Slack, G., Eds., Materials Research Society, Pittsburgh, 1991, 145.

6 Bouchacourt, M. and Thevenot, F., "The correlation between the thermoelectric properties and stoichiometry in the boron carbide phase B4C – B10.5C", J. Mater. Sci. 20 (1985) 1237.

7 Aselage, T. and Emin, D., CRC Handbook of Thermoelectrics, D. M. Rowe, ed. CRC Press, Inc. (1995) 373.

8 Sidorenko, N. A., and Mosolov, A. B., in Proc. X Inter. Conf. On Thermoelectric Energy Conversion, Rowe, D. M.,Ed., University of Wales, Cardiff, 1991, 80.

9 Seebeck, T., Magnetic Polarization of metals and minerals, *Abhandlungen der Deutschen Akademie der Wissenschaften zu Berlin*, 265, 1822-23.

10 Peltier, J., Nouvelles experiences sur la caloricite des courans electrique, Ann. Chim., LVI 371, 1834.

11 Ioffe, A.F., *Semiconductor Thermoelements and Thermoelectric Cooling*, Infosearch, London, 1957.

12 Ho, C. Ackerman, W. and Wu, K., "Thermal Conductivity of copper-nickel and silver-palladium alloy systems" Thermal Conductivity **14**, edited by P. Klemens and T. Chu, (Plenum Press, New York, 1976) 233-244.

13 Vining, C.B., private communication

14 Barnard, R.D., *Thermoelectricity in Metals and Alloys*, Taylor & Frances, London, 1972.

15 Ioffe, A. F., Proc. Inter. Conf. On Electron Transport in Metals and Solids, Ottawa, (1956) p. 1342

16 Chasmar, R. P., and Stratton, R. J., J. Electron. Control 7 (1959) 52.

17 Walker, H. Z. Naturf. a 7 (1952) 744.

18 Goodman, C. H. L. Proc. Phys. Soc. B 67 (1954) 258.

19 Klemens, P. G., Proc. Phys. Soc. A 68 (1955) 1113.

20 Goldsmid, A. J. Thermoelectric Refrigeration (New York, Plenum) 1964.

21 Dismukes, J. P., Ekstrom, L. , Steigmeier, E. F., Kudman, I., and Beers, D. S., J. Appl. Phys. 35 (1964) 2899.

22 Ioffe, A. F., "Semiconductor Thermoelements and Thermoelectric Cooling Information", Infosearch, London (1957).

23 Wood, C. Rep. Prog. Phys. 51 (1988) 459-540.

24 McVay, G.L., Lefever, R.A., and Baughman, R.J., Mater. Res. Bull. **9**, 735 (1974).

25 Goldsmid, H.J. and Penn, A.W., Phys. Lett. **27A**, 523 (1968).

26 Parrot, J.E., J. Phys. C. : Solid St. Phys. **2**, 147 (1969).

27 Vandersande, J.W., Wood, C., and Draper, S., Mater. Res. Soc. Symp. Proc. **97**, 347 (1987).

28 Fleurial, J-P., Borshchevsky, A., Vandersande, J.W., Scoville, N., and Bajgar, C., Proc. IX Symp. on Space Nuc. Power Systems **1**, 326 (1992).

29 Cook, B.A., Harringa, J.L., Han, S.H., and Beaudry, B.J., J. Appl. Phys. **72**(4), 1423 (1992).

30 Pisharody, R.K. and Garvey, L.P., Proc. XIII IECEC **3**, 1963 (1978).

31 Fleurial, J-P., Borshchevsky, A., Proc. IX Int. Conf. on Thermoelectrics , Jet Propulsion Laboratory, C. B. Vining, ed. (1990) 206.

32 Vining, C.B., J. Appl. Phys. **69** 331 (1991).

33 Slack, G. and Hussain, M.A., J. Appl. Phys. **70** 2694 (1992).

34 Michitaka Ohtaki, Toshiki Tsubota, Koichi Eguchi, and Hiromichi Arai, J. Appl. Phys. **79** (1996) 1816.

35 Y. Tanaka, T. Ifuku, K. Tsuchida, and A. Kato, J. Mat. Sci. Letters **16** (1997) 155.

36 R. Wang, L. H. King, and A. W. Sleight, J. Mater. Res., **11** (1996) 1659.

37 Z.M. Dashevsky, L.L. Dudkin, V.B. Eliseev, and R.V. Skolozdra, "New Materials for Thermoelectric Generation", X Int. Conf. on Thermoelectrics, D.M. Rowe, ed. (Babrow Press, Cardiff, UK, 1991) 186-190.

38 F.G. Aliev, *Physica B* **171** (1991) 199-205.

39 F.G. Aliev, N.B. Brandt, V.V. Moshchalkov, V.V. Kozyrkov, R.V. Skolozdra, and A.I. Belogorokhov, *Z. Phys. B - Condensed Matter* **75** (1989) 167-171.

40 S. Ögut and K.M. Rabe, *Phys. Rev. B* **51**, 16 (1995) 10443-10453.

41 B. A. Cook, J. L. Harringa, Z. S. Tan, and W. A. Jesser, Proc. XV Intl. Conf. On Thermoelectrics, Pasadena, CA, March 1996, IEEE Catalog Number 96TH8169, p. 122.

42 F.G. Aliev, V.V. Kozyrkov, V.V. Moshchalkov, R.V. Scolozdra, and K. Durczewski, *Z. Phys. B - Condensed Matter* **80** (1990) 353-357.

43 A.H. El-Sayed, G.J. Nieuwenhuys, J.A. Mydosh, and K.H.J. Buschow, *J. Phys. F: Met. Phys.* **18** (1988) 2265-2281.

44 C. Uher, J. Yang, S. Hu, D. T. Morelli, and G. P. Meisner, Phys. Rev. B 59 (1999) 8615.

45 G. Ji, X. J. Fan, J. H. Zhang, C. S. Xiong, and X-G Li, J. Phys. D: Applied Phys. 31 (1998) 3036.

ACKNOWLEDGMENTS

This work was performed at Ames Laboratory under Contract No. W-7405-Eng-82 with the U. S. Department of Energy. The United States government has assigned the DOE Report number IST 1874 to this dissertation.

There are many who deserve recognition for their contributions, either directly or indirectly, to the completion of this project. K. A. Gschneidner, Jr. has maintained an interest and involvement in thermoelectric materials research over the years, despite the demands of directing a highly successful research activity in magnetic refrigeration. His continued support is greatly appreciated. The assistance and professionalism of numerous staff members of the Ames Laboratory has been, and continues to be appreciated by the author. Among these individuals, the efforts of Fran Laabs (electron microscopy) and Hal Sailsbury (optical microscopy and specimen preparation) deserve particular attention for the high quality of their work and their willingness to respond to time-critical needs.

The author would also like to acknowledge Dr. William J. Barnett, program manager of the U.S. Department of Energy's Office of Special Applications (NE-53), for his continued support, encouragement, and stimulating conversations over the years.

The author would like to offer special recognition and thanks to two individuals who have played pivotal roles throughout these various project. As the author's immediate supervisor, Bernard Beaudry, provided an environment in which continuing education was encouraged and supported. His advice and friendship will always be appreciated. In addition, this work would not have been possible without the assistance of Joel Harringa, who continued to faithfully maintain and upgrade equipment, prepare and instrument samples, and perform countless errands, despite the inevitable uncertainties of research funding and the demands on his own time.